4-2016

Incorporation of GNSS multipath to improve autonomous rendezvous, docking and proximity operations in space

Benjamin W. Ashman
Purdue University

Graduate School Form
30 Updated 12/26/2015

PURDUE UNIVERSITY
GRADUATE SCHOOL
Thesis/Dissertation Acceptance

This is to certify that the thesis/dissertation prepared

By Benjamin W. Ashman

Entitled
Incorporation of GNSS Multipath to Improve Autonomous Rendezvous, Docking and Proximity Operations in Space

For the degree of Doctor of Philosophy

Is approved by the final examining committee:

James L. Garrison
Co-chair

Mark R. Bell
Co-chair

James V. Krogmeier

Luke M. Winternitz

To the best of my knowledge and as understood by the student in the Thesis/Dissertation Agreement, Publication Delay, and Certification Disclaimer (Graduate School Form 32), this thesis/dissertation adheres to the provisions of Purdue University's "Policy of Integrity in Research" and the use of copyright material.

Approved by Major Professor(s): James L. Garrison

Approved by: V. Ragu Balakrishnan 4/28/2016

Head of the Departmental Graduate Program Date

INCORPORATION OF GNSS MULTIPATH TO IMPROVE AUTONOMOUS RENDEZVOUS, DOCKING AND PROXIMITY OPERATIONS IN SPACE

A Dissertation

Submitted to the Faculty

of

Purdue University

by

Benjamin W. Ashman

In Partial Fulfillment of the

Requirements for the Degree

of

Doctor of Philosophy

May 2016

Purdue University

West Lafayette, Indiana

To the West Lafayette Ashmans.

ACKNOWLEDGMENTS

This research has only been possible through the support and contributions of a great many people. I thank Dr. James Garrison for guiding this work for the last five years. Four of those years were funded by a NASA Space Technology Research Fellowship (grant NNX11AN52H), and I also thank my fellowship mentor and committee member Dr. Luke Winternitz for his guidance and input throughout. I thank Dr. Mark Bell and Dr. James Krogmeier for serving on my committee and helping me through my graduate school.

Many engineers at NASA Goddard Space Flight Center took an interest in this work and provided critical feedback and insight, especially Sam Price and Jenny Valdez. Also at Goddard, Victor Fontanez assisted with antenna measurements in the GEMAC and Todd Bentley helped construct the antenna mounting plate. I am deeply appreciative of Dr. Penina Axelrad and Jeanette Veldman at the University of Colorado for their contributions and suggestions throughout our collaboration.

I thank Dr. Nuri Emanatoglu at the University of Maine, my first research advisor. His guidance during my summer National Science Foundation fellowship inspired my interest in graduate school. I also thank Shyler Switzer and Micah McCreery, at what was then the Ohio Coal Research Center in Athens, for teaching me practical research skills, like how to work through being stuck on a problem.

On a personal note, I thank my friends at Purdue in the W&C Society for teaching me about philosophy, epistemology, metaphysics, and arguing, especially Mark, Davis, Lauren, Joel and Natalie. I enjoyed living in Lafayette for the last six years, not least of all because of the time it gave me with my family here. Getting together for pizza most weeks kept everything in context. I especially thank Leah Bevis for her support, every day since the beginning, without which I'm not sure I could have kept at it. Finally I thank my immediate family, Lewis, Diane and Sam, for their encouragement,

phone calls and visits. They inspire me with their insatiable curiosity about the world and love of learning.

TABLE OF CONTENTS

Page

Page

LIST OF TABLES

LIST OF FIGURES

ABBREVIATIONS

AR&D	Autonomous Rendezvous and Docking
C/N_0	carrier to noise spectral density
DLL	Delay Lock Loop
EKF	Extended Kalman Filter
FFT	Fast Fourier Transform
GO	Geometrical Optics
GPS	Global Positioning System
GNSS	Global Navigation Satellite System
GSFC	Goddard Space Flight Center
HEO	high Earth orbit
HSM4	Hubble Servicing Mission 4
IF	intermediate frequency
IFFT	Inverse Fast Fourier Transform
IGS	International GNSS Service
IMU	Inertial Measurement Unit
LCP	Left-hand Circularly Polarized
LOS	line of sight
MATLAB	matrix laboratory
MSM	Mass Storage Module
PATH	Postflight Attitude and Trajectory History
PLL	Phase Lock Loop
RCP	Right-hand Circularly Polarized
RELBET	Relative Best Estimate Trajectory
RF	radio frequency

RMSE	root mean square error
PRN	Pseudo-random Noise (code)
RNS SDR	Relative Navigation Sensor Software-Defined Radio
SDR	software-defined radio
SNR	Signal to Noise Ratio
STK	Systems Tool Kit
UGDT	Uniform Geometrical Theory of Diffraction
UTC	Universal Consolidated Time

ABSTRACT

Ashman, Benjamin W. Ph.D., Purdue University, May 2016. Incorporation of GNSS Multipath to Improve Autonomous Rendezvous, Docking and Proximity Operations in Space. Major Professors: James L. Garrison and Mark R. Bell.

Automated rendezvous and docking (AR&D) operations are important for many future space missions, such as the resupply of space stations, repair and refueling of large satellites, and active removal of orbital debris. These operations depend critically on accurate, real-time knowledge of the relative position and velocity between two space vehicles. Unfortunately, Global Navigation Satellite System (GNSS) capabilities remain severely limited in close proximity to large space structures due to significant multipath effects and signal blockage. Although GNSS is used for the initial stages of approach, other instruments such as laser, radar and vision-based systems, are required to augment GNSS during AR&D over the last few hundred meters.

This dissertation models the GNSS signal received during such proximity operations, and uses this information to improve relative navigation accuracy and integrity. Methods for separating and interpreting reflected signals are demonstrated using GNSS data collected during Hubble Servicing Mission 4 (HSM4), a model of the mission geometry, electromagnetic (EM) ray tracing, and a custom GNSS software receiver. EM ray tracing is used to show that a number of signals sufficient for ranging are reflected by the Hubble Space Telescope (HST) during HSM4, and the properties of these reflections are used to generate simulated GNSS data. The impact of reflected signals on code correlation shape, code tracking error, and pseudorange measurement is demonstrated using the simulated and experimental data.

Relative navigation is demonstrated using simulated reflected signal measurements and the dependence of relative navigation on the reflecting object's scattering properties is illustrated. From the tracking of data from two oppositely polarized antennas, both simulated and experimental, it is determined that multipath measurements are limited by system properties such as antenna polarization quality and front end bandwidth. Design considerations involved in optimizing a receiver to measure reflected signals are discussed.

1. INTRODUCTION

NASA has done extensive work over the past two decades to incorporate GNSS into a variety of missions as a source of position, velocity, time, and attitude [1] [2], including the U.S. portion of the International Space Station, where GNSS has been the primary source of this information since April 2002 [3]. Historically, spacecraft navigation has been dependent on communication with ground stations, where orbit determination is performed offline, i.e., not real-time. Regular communication links must be performed and ground assets maintained, introducing additional expenses and logistical challenges that limit mission design. However, with the advent of advanced, space-capable receivers, such as the Navigator receiver designed at Goddard Space Flight Center (GSFC) [4], on-board, autonomous navigation has become increasingly feasible for any operations in cis-lunar space [5].

In the rendezvous and docking of spacecraft, GNSS signals can reflect off the target vehicle and cause prohibitively large error in the chaser vehicle receiver at ranges below 200 meters [6]. These errors vary in time due to the relative motion and geometry of the vehicles involved [7] or produce systematic errors if the direct signal is completely blocked. In order to calculate a receivers position, the time of travel for line of sight signals must be determined from at least four satellites. When a large object is located in close proximity to the receiver, reflections of the transmitted signals may also be received. These delayed replicas of the direct signals contribute erroneous time of travel information to the receivers position calculation, an error called multipath. Although GNSS is used for the initial stages of approach, relative range information during docking must currently be obtained from other sensors over the last few hundred meters. Availability of a single, reliable relative range source over all approach stages would be especially useful for autonomous rendezvous and docking (AR&D) missions, such as satellite servicing.

The significance of multipath error in docking scenarios has been studied, but most methods address it by modeling the multipath signals and developing methods to mitigate the resulting receiver errors [8] [1] [2]. Rather than eliminating multipath, it has been proposed that these additional ray paths be used as a source of information about the distance of the target vehicle from the receiver [9]. The technique of estimating receiver-to-target range using a reflected signal from a separate transmitter is known as bistatic radar. This has been demonstrated using reflected GNSS signals in the case of aircraft altimetry [10] and a fixed target [11].

Unlike the estimation of error due to multipath, determining a reflected signal's additional path length requires measuring and comparing the raw signal correlation properties of the direct and reflected signals. If the difference in arrival time for these two signals corresponds to a path difference of less than one C/A code chip (approximately 293 m), it is difficult to separate them using conventional tracking methods. The shape of the code correlation will be the result of summing both signals. Consequently, an experiment was performed during Hubble Servicing Mission 4 (HSM4), in which sampled intermediate-frequency (IF) data were collected from two oppositely polarized antennas, one tuned to receive direct signals, the other reflected signals. This dissertation explores the challenges involved in processing reflected GNSS signals for relative navigation during spacecraft rendezvous and docking, using HSM4 as a case study.

2. OVERVIEW OF GLOBAL NAVIGATION SATELLITE SYSTEMS

2.1 Background

Radio navigation relies on the principle that electromagnetic signals travel through space at a known rate. If a signal's time of travel can be measured, the distance between the points of reception and transmission can be calculated. With measurements from multiple transmitters, the receiver's position can be estimated using the technique of trilateration. Several radio navigation systems preceded satellite navigation (e.g., LORAN and Omega in the 1940s and 1960s respectively), but these employed ground-based beacons that were limited in range and provided only two-dimensional estimates of a receiver's position. This was sufficient for terrestrial and maritime applications, but the advent of aviation made altitude increasingly important.

In 1957 it was observed that *Sputnik I*'s orbit could be determined by measuring the Doppler shift of its signals received at a ground station with a known location. Using this principle, the U.S. Navy developed the first satellite navigation system, Transit, in which the transmitting satellite positions were known and a receiver's position was estimated from the Doppler shifts. Parallel navigation projects were being pursued in the U.S. Army and U.S. Air Force (MOSAIC and SECOR, respectively) throughout the 1960s. In 1973, these programs were combined, along with the Navy's Timation satellite system, into NAVSTAR, now referred to as the Global Positioning System (GPS). The first satellite was launched in 1978 and the system was declared to have Full Operational Capacity in 1995 [12].

The Soviet Union simultaneously developed its own satellite navigation system, GLONASS, from two systems similar to Transit (Parus and Tskikada). Other systems in various stages of planning or testing include China's BeiDou and the European

Union's Galileo. Systems with regional coverage include India's IRNSS and Japan's QZSS. These systems are referred to collectively as Global Navigation Satellite Systems (GNSS). Although the following discussion will use the specific architecture of GPS as an example, the concepts explored in this dissertation are broadly applicable to all GNSS.

2.2 Global Positioning System Signal Structure

GNSS signals are designed to satisfy a number of constraints. The primary objective is to estimate the receiver's position using trilateration. To this end, signals must be designed so that the propagation delay between the transmitter and receiver can be measured. GNSS signals must also allow multiple access and provide robustness to interference and multipath.

The GPS constellation consists of 32 satellites in six orbital planes. The satellites are in nearly circular orbits, each with a radius of approximately $26,600$ km. This arrangement ensures that more than eight satellites are always visible at any point on the earth. A complete description of GPS signals is given in the interface specifications document maintained by the U.S. government [13]. Each satellite transmits several signals at different carrier frequencies, but only the civilian signal transmitted on the L1 carrier will be considered here. This signal received from the i-th GPS satellite can be written

$$y^i(t) = a^i(t)d^i(t-\tau^i(t))p^i(t-\tau^i(t))\cos(2\pi(f_{L1}+f_D^i)t+\theta^i(t_0))+v^i(t). \tag{2.1}$$

Dropping the satellite superscripts when there is no risk of ambiguity, the signal essentially consists of two codes, $d(t)$ and $p(t)$, modulated by a radio frequency (RF) carrier with an amplitude $a(t)$. Random noise affecting the signal at reception is modeled by adding a circular symmetric Gaussian random variable $v(t)$ with zero mean and variance σ^2. The carrier frequency of the GPS L1 signal, f_{L1}, is 1.57542 GHz. This is chosen to penetrate the atmosphere and satisfy spectrum restrictions for satellite navigation. This particular value is mathematically related to the code

frequencies, as well as the L2 and L5 frequencies, allowing all to be generated from the same on-board clocks. The carrier is shifted in frequency by an unknown Doppler shift f_D due to the rate of change of the distance between the transmitting satellite and the receiving antenna. For distance rate of change $\dot{r}(t)$ and rate of signal propagation c, $f_D = \dot{r}(t) f_{L1}/c$. Doppler effects on $d(t)$ and $p(t)$ are ignored for now, as their lower frequencies result in comparatively minor effects.

Amplitude is a function of the signal power, $a(t) = \sqrt{2P_R(t)}$. The received signal power is the result of the satellite's 27 Watt transmission, 14.7 dB antenna gain (at boresight), spreading loss over the distance of propagation, and receive antenna gain properties. The signal $d(t)$ is a 12.5 minute navigation data message, transmitted at 50 bits per second. The navigation message contains information on the transmitting satellite's health, ephemeris, and clock bias, as well as reduced-precision ephemerides for all of the satellites in the constellation. This message also contains time of transmission information, essential for resolving cycle ambiguities in the spreading code.

The spreading code $p(t)$ is referred to as the Coarse Acquisition code (C/A code). This is chosen to have autocorrelation and cross correlation properties that enable propagation delay measurement and multiple access. To meet these requirements, signals must have a small autocorrelation function except at zero offset, and a small cross correlation function at all shifts [14]. This means that for two different satellites the cross correlation of their corresponding codes is nearly zero, allowing multiple access, and for a single satellite the autocorrelation of its code is nearly zero at all shifts other than zero, enabling delay measurement. Several different coding schemes meet this criteria, but 1023-length Gold sequences are used for the GPS civilian code [15].

The C/A code is a sequence of 1.023 MHz square pulses that is periodic with period 1 ms. Each code is the sum of two maximal length sequences (of length $2^{10}-1 = 1023$) generated by tapped linear feedback shift registers. Although deterministic, the codes exhibit noise-like properties and are also referred to as pseudo-random noise (PRN) codes. A unique code is generated for each satellite by different shift register taps.

The code's pulses are called "chips" to distinguish them from the 50Hz information-bearing "bits" of the navigation message.

The signal arrives at the receive antenna delayed by $\tau(t)$ seconds due to the time of propagation. This delay can be seen in each of the components of Equation (2.1); in the carrier term it is contained in the unknown initial phase $\theta(t_0)$. The ability to determine this delay and reference it to the time of transmission contained in the navigation data message is essential to the satellite navigation concept. This is accomplished by processing the ambiguity function.

2.2.1 Ambiguity Function

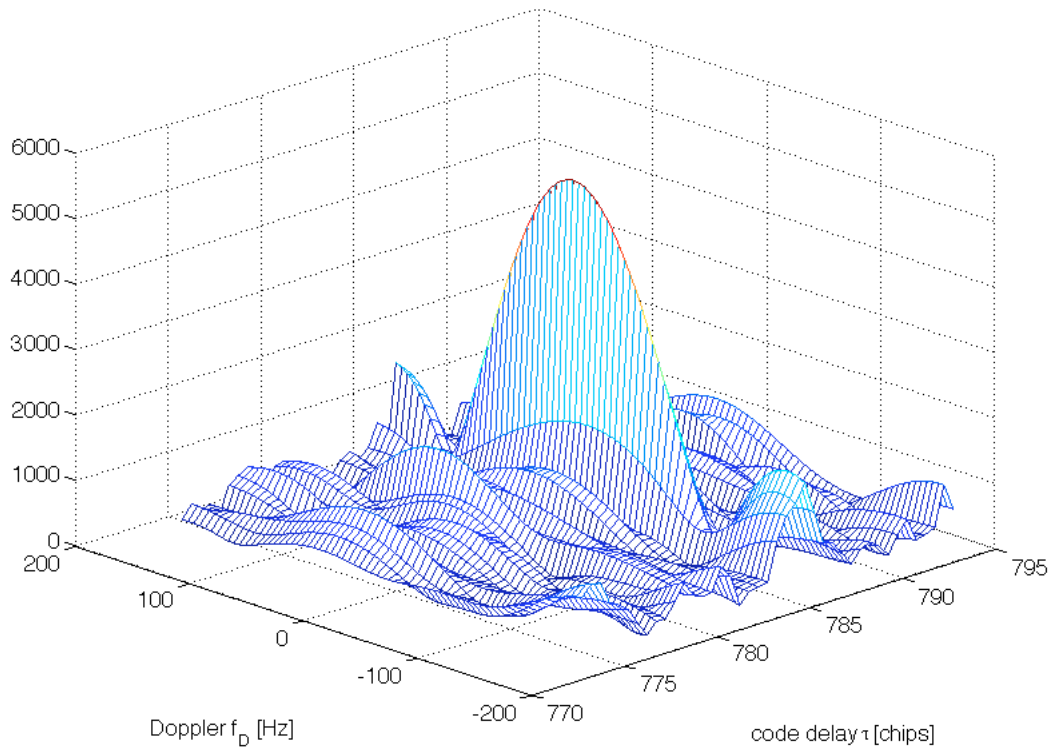

Fig. 2.1. Example of correlation peak in Doppler and delay from HSM4 data processing

In order to determine the delay and frequency of the incoming signal, or the presence of a signal at all, it is necessary to form a decision statistic. A GPS receiver is a correlation receiver, that is, it correlates the incoming signal with a local copy of that signal. This is equivalent to convolving the input signal with a matched filter, and is optimal in the sense that it maximizes the signal to noise ratio (SNR). Recall that the incoming signal arrives with an unknown delay and Doppler. The filter matched to the C/A code is mismatched with respect to the received signal in delay and Doppler by τ and f_D respectively. The two-dimensional function at the matched filter output is an asymmetric ambiguity function,

$$\chi(\tau, f_D) = \int_{t-T_I}^{t} p(\alpha)p^*(\alpha - \tau)e^{i2\pi f_D \alpha}\, d\alpha, \tag{2.2}$$

where the asterisk indicates a complex conjugate.

An example ambiguity function is shown in Figure 2.1. For illustrative purposes, only a segment of the code delay axis is shown. This is an optimal decision statistic for estimating the delay and Doppler of the received signal defined in Equation (2.1) after removal of the carrier [16]. A GPS receiver applies a test delay $\tilde{\tau}$ and test Doppler $\tilde{f}_D$ to the local code replica, and the values that maximize the decision statistic (i.e., the ambiguity function peak in delay and Doppler space) are taken as the estimated delay and Doppler of the incoming signal. The convolution sample time, T_I, corresponds to the signal length and is an important factor in noise performance known as the pre-detection integration time.

The ranging properties of the GPS signal depend on the shape of the ambiguity function. Along the zero delay axis, $p^2(t) = 1$ for a normalized C/A code. Considering signals with finite length T_I and $t_0 = 0$,

$$\begin{aligned}\chi(0, f_D) = \int_0^{T_I} e^{i2\pi f_D t}\, dt &= \frac{1}{i2\pi f_D}\left(e^{i2\pi f_D T_I} - 1\right) \\ &= \frac{T_I e^{i2\pi f_D T_I/2}}{i2\pi f_D T_I}\left(e^{i\pi f_D T_I} - e^{-i\pi f_D T_I}\right).\end{aligned}$$

Using Euler's formula for expressing sine in terms of exponentials, this simplifies to

$$\frac{e^{i2\pi f_D T_I/2}}{i2\pi f_D T_I} 2i \sin(\pi f_D T_I) = T_I e^{i\pi f_D T_I} \mathrm{sinc}(f_D T_I).$$

This amounts to the Fourier transform of a square pulse with length T_I. Therefore, $\chi(0, f_D)$ is a scaled sinc function with nulls occurring at integer multiples of $\pm 1/T_I$. In order to detect the main lobe of $\chi(\tau, f_D)$ in the Doppler dimension, the frequency search must have a step size less than or equal to $1/(2T_I)$. A finer resolution search will maximize the detected peak but require more computation. The range of Doppler frequencies that must be searched can be determined from estimated receiver dynamics.

Along the delay dimension (i.e., $\chi(\tau, 0)$), the ambiguity function has the shape of a C/A code autocorrelation function. For local C/A code replica $p(t)$, the normalized correlation of the incoming code shifted by τ is given by

$$R(\tau) = \frac{1}{T_I} \int_{t-T_I}^{t} p(\alpha) p(\alpha - \tau) d\alpha. \tag{2.3}$$

Here the complex conjugate has been ignored - the locally generated replica code sequence is strictly real. Although the exact shape of the correlation function over all τ varies by PRN, in every case the autocorrelation has a peak at $\tau = 0$, decreasing linearly to approximately zero at $\tau = \pm T_c$, where T_c is the chip period.

Note that in the preceding formulas the reference local code replica is not shifted, so the propagation delay τ of the incoming signal is identical to the shift offset between the two codes. In general a test shift of $\tilde{\tau}$ is applied to the local code, so that the relative shift is $\epsilon = \tilde{\tau} - \tau$ and the ideal code correlation function is

$$R(\epsilon) = \begin{cases} 1 - \frac{|\epsilon|}{T_C} & \text{for } |\epsilon| \leq T_C \\ 0 & \text{elsewhere} \end{cases}. \tag{2.4}$$

The shift in the local code necessary to maximize the code correlation function is the incoming signal delay modulo one code period, also referred to as the code phase.

2.2.2 Complex Accumulations

The ambiguity function formed by a GPS receiver is complex, however. A detailed model of complex accumulations is given by Psiaki et al. in their 2015 article on

multipath estimation using antenna motion [17]; a simplification of their model is used in this dissertation. The received signal in Equation (2.1) is mixed to an intermediate frequency, filtered, and sampled. The raw RF front end output sample at receiver sample time t_i can be written

$$y_i = y(t)2e^{j\omega_{LO}t} * h(t)|_{\text{at } t=iT_s}. \tag{2.5}$$

Here ω_{LO} is the local oscillator frequency such that the intermediate frequency $\omega_{IF} = \omega_{LO} - \omega_{L1}$, $h(t)$ is the front end filter's complex envelope response function and $*$ indicates convolution. The signal is sampled at sampling rate $f_s = 1/T_s$. This is shown in Figure 2.2. Omega is used to indicate a frequency in radians (e.g., $\omega_{L1} = 2\pi f_{L1}$, where f_{L1} is in hertz).

If $h(t)$ is a bandpass filter centered at ω_{IF} with two-sided bandwidth B in Hz such that $B < f_s$ (i.e., there is no aliasing), then

$$\begin{aligned} y_i = a(t_i)\{&\tilde{p}_I(t_i - \tau(t_i))\cos(\omega_{IF}t_i + \phi_{NBC}(t_i)) \\ &+ j\tilde{p}_Q(t_i - \tau(t_i))\sin(\omega_{IF}t_i + \phi_{NBC}(t_i))\} + v(t_i). \end{aligned} \tag{2.6}$$

Assuming the code correlation is aligned with the start edge of a navigation bit and the accumulation length T_I is no longer than one bit (20 ms), the navigation message $d(t)$ can be ignored here. Doppler effects on the code are again ignored for now. The negative beat carrier frequency arising from the local oscillator phase mismatch during downconversion to IF is defined $\phi_{NBC}(t_i) = -\omega_D t_i - \theta(t_0)$ (i.e., the time integral of the Doppler).

Here $\tilde{p}_I$ and $\tilde{p}_Q$ are, respectively, the in-phase and quadrature components of the signal's PRN code after front end filtering:

$$\tilde{p}_I(t) = \text{real}\left\{ \int_{-\infty}^{\infty} p(\beta)h(t-\beta)\,d\beta \right\} \tag{2.7}$$

$$\tilde{p}_Q(t) = \text{imag}\left\{ \int_{-\infty}^{\infty} p(\beta)h(t-\beta)\,d\beta \right\}. \tag{2.8}$$

Although the PRN code is nominally transmitted on the in-phase channel only, some code will appear on the quadrature channel due to imperfect phase alignment of the

local oscillator with the incoming signal. The two codes are further distinguished by the real and imaginary responses of the front-end filter, which in general are not the same [18].

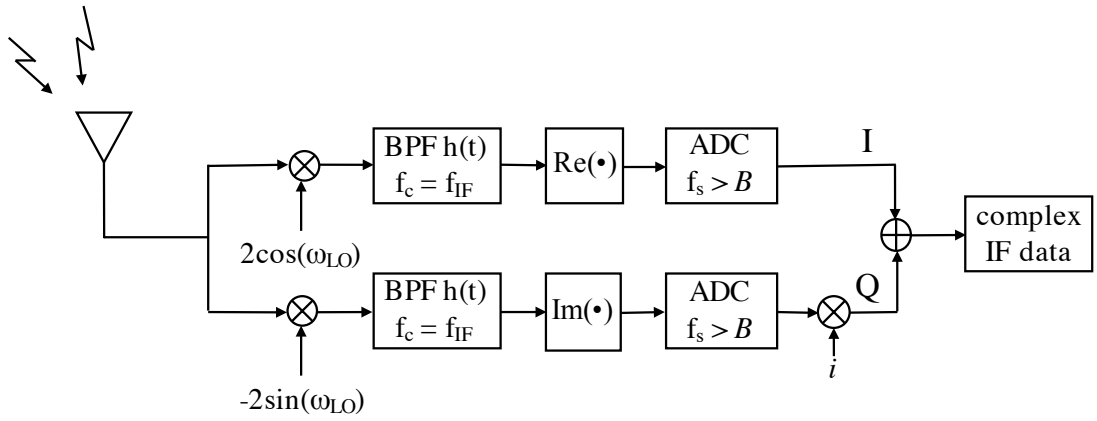

Fig. 2.2. RF front end

The ideal code correlation in Equation (2.4) is a function of the offset ϵ between the incoming code and the local code replica. For an estimated delay $\hat{\tau}$, consider an arbitrary number of correlators offset by η from $\hat{\tau}$. The correlation value at each η is the sum of the incoming code and local code product over the correlation length, or predetection integration time, T_I. This sum is known as an accumulation, and the k-th in-phase and quadrature accumulations are computed

$$I_k(\eta) = \text{real}\left\{ \sum_{i=i_k}^{i_k+N_k-1} y_i p(t_i - \hat{\tau}_k - \eta) \exp(-j(\omega_{IF} t_i + \hat{\phi}_k + \hat{\omega}_k(t_i - \hat{\tau}_k))) \right\}, \quad (2.9)$$

$$Q_k(\eta) = \text{imag}\left\{ \sum_{i=i_k}^{i_k+N_k-1} y_i p(t_i - \hat{\tau}_k - \eta) \exp(-j(\omega_{IF} t_i + \hat{\phi}_k + \hat{\omega}_k(t_i - \hat{\tau}_k))) \right\}. \quad (2.10)$$

where N_k is the number of samples in T_I. The delay estimate $\hat{\tau}_k$ is formed in the receiver by the Delay Lock Loop, while estimates of the negative beat carrier phase $\hat{\phi}_k$ and Doppler shift $\hat{\omega}_k$ are formed by the Phase Lock Loop, both described in more detail in Sections 2.3.3.

Consider the in-phase accumulation. Assuming double frequency terms average out in the accumulation,

$$I_k(\eta) = \frac{1}{2}\sum_{i=i_k}^{i_k+N_k-1} a(t_i)\Big\{\tilde{p}_I(t_i-\tau(t_i))p(t_i-\hat{\tau}_k-\eta)\cos(\hat{\phi}_k+\hat{\omega}_k(t_i-\tau_k)-\phi_{NBC}(t_i)) - \tilde{p}_Q(t_i-\tau(t_i))p(t_i-\hat{\tau}_k-\eta)\sin(\hat{\phi}_k+\hat{\omega}_k(t_i-\tau_k)-\phi_{NBC}(t_i))\Big\}. \quad (2.11)$$

The frequency term

$$f(t_i) = \hat{\phi}_k + \hat{\omega}_k(t_i-\tau_k) - \phi_{NBC}(t_i), \quad (2.12)$$

is the error in the PLL carrier estimate. For small errors this can be approximated as constant over the accumulation

$$f(t_i) \approx f(\bar{t}_k) = \Delta\phi_k + \Delta\omega_k\bar{t}_k, \quad (2.13)$$

where $\Delta\phi_k$ is the phase difference between the local oscillator and the carrier, and $\Delta\omega_k$ the carrier Doppler shift error at the accumulation midpoint $\bar{t}_k$. If the code correlations are written as a function of the DLL error $\Delta\tau_k = \tau_k - \hat{\tau}_k$,

$$\tilde{R}_I(\Delta\tau_k+\eta) = \sum_{i=i_k}^{i_k+N_k-1}\tilde{p}_I(t_i-\tau_k)p(t_i-\hat{\tau}_k-\eta), \quad (2.14)$$

and

$$\tilde{R}_Q(\Delta\tau_k+\eta) = \sum_{i=i_k}^{i_k+N_k-1}\tilde{p}_Q(t_i-\tau_k)p(t_i-\hat{\tau}_k-\eta), \quad (2.15)$$

then the complete description of the in-phase accumulation is

$$I_k(\eta) = \frac{1}{2}A_k\Big\{\cos(\Delta\phi_k+\Delta\omega_k\bar{t}_k)\tilde{R}_I(\Delta\tau_k+\eta) - \sin(\Delta\phi_k+\Delta\omega_k\bar{t}_k)\tilde{R}_Q(\Delta\tau_k+\eta)\Big\}, \quad (2.16)$$

where A_k is the signal amplitude at the start of the k-th accumulation interval. The quadrature channel can be computed in a similar manner and the complex accumulation formed $I_k(\eta) + jQ_k(\eta)$. When tracking is locked, power is concentrated in the in-phase accumulations, and the presence of the quadrature code term on the in-phase channel is negligible. In the presence of multipath, however, the shape of the ambiguity function is distorted in complex space, so the representation of the accumulation as complex becomes important [17]. This is discussed further in Section 3.3.

2.3 RNS SDR Receiver Architecture

A GPS receiver has three main tasks: determine which satellites are visible, and estimate the delay and Doppler associated with each; refine the delay and Doppler estimates and track these features as they change over time; and use measurements from all visible signals to produce an estimate of the receiver's position and velocity. These processes are referred to as acquisition, tracking and navigation respectively, and are covered in detail in the corresponding chapters of the American Institute of Aeronautics and Astronautics' *Global Positioning System: Theory and Applications* (references [19], [20] and [21] respectively). Acquisition and tracking will be discussed here by describing the particular features of the software receiver developed and used in this research. Navigation is addressed later in Chapter 7.

A software-defined radio (SDR) is a system for processing RF signals that is constructed entirely in software. Input data is in the form of real or complex samples taken immediately after the received signal is downconverted to an intermediate frequency. An SDR allows complete flexibility in the design and modification of receiver components. An SDR also provides access to the signal at every stage of processing. A custom software-defined GPS receiver was constructed specifically to analyze the HSM4 data because the novel processing of multipath for relative range information involves examination and exploitation of signal features on a fundamental level. This receiver, the Relative Navigation Sensor Software-Defined Radio (RNS SDR), was written in MATLAB and consists of several interconnected modules.

2.3.1 Program Operation

Running the RNS SDR script calls a separate settings file, then performs acquisition, plots carrier to noise spectral density (C/N_0) estimates from acquisition, performs signal tracking, plots tracking results and finally saves the acquisition and tracking results. The settings script allows the receiver to be configured for processing simulated data or data from HSM4. The receiver has also been used for processing

a number of other data sets of various data types, though always complex in the form of interleaved in-phase and quadrature samples. When processing HSM4 data, predictions of Doppler for each satellite from Systems Tool Kit (STK) are used to aid satellite search.

The start time of tracking is set in terms of Universal Consolidated Time (UTC), which is then referenced to a specified file start time. Tracking duration is set in seconds. The pre-detection integration time, Doppler search resolution and other acquisition and tracking parameters can be adjusted. An acquisition threshold can be chosen to determine satellite visibility at the time of acquisition, but a non-visible satellite must be set as a noise floor reference for computing acquisition C/N_0 estimates. After the receiver loses lock it does not automatically attempt to re-acquire. The receiver can be run for the whole GPS constellation, but because channels are processed serially this is computationally time consuming. Typical operation is to run the receiver for a particular PRN and time frame of interest. Acquisition and tracking results are saved in directories by date for access by post-processing scripts (e.g., prompt power oscillation plots, excess pseudorange calculations).

2.3.2 Acquisition

After establishing signal parameters and file identifiers, program flow proceeds to signal acquisition. Acquisition seeks to determine which satellites are visible and then form an estimate of the delay and Doppler of each in order to initialize tracking. The basic premise has been described above: correlate the incoming signal with local replica signals across a span of frequencies, and seed tracking with the Doppler and delay estimates that maximize the correlation.

A pre-detection integration time longer than 1 ms is needed for the acquisition of weak signals. Consider that the nominal received GPS signal power is -130 dBm. Due to the 1.023 MHz C/A code, the received GPS signal has a bandwidth of approximately 2 MHz. For this bandwidth, the noise power is greater than the signal

strength: $P_{N,dB} = 10\log_{10}(kTB) = -110$ dBm, where k is Boltzmann's constant, T is the equivalent noise temperature (usually 273 K) and B is the bandwidth considered. Using an integration time of 1 ms to correlate with the C/A code corresponds to a filter bandwidth of 1 kHz and a noise power of -144 dBm, bringing the noise floor below the received signal power. Increasing the pre-detection integration time to raise the SNR is critical for weaker signals [22].

When $T_I > 1$ ms, data bits cannot be regarded as constant. Even when $T_I = 1$ ms is used for tracking, RNS SDR performs fine acquisition using 10 ms coherent integration. Following the Alternate Half-Bits Method in [23], four 10 ms correlations of N samples are formed,

$$z(\tilde{\tau}, \tilde{\omega}_D) = \sum_{i=N\ell}^{N(\ell+1)-1} y_i p_{i-\tilde{\tau}} \exp(-j(\omega_{IF} - \tilde{\omega}_D)t_i), \tag{2.17}$$

for correlation start time $\ell = \{1, 2, 3, 4\}$, test delay $\tilde{\tau}$ and test Doppler $\tilde{\omega}_D$. The N sums within each correlation preserve phase and therefore add coherently. The duration of each coherent correlation is adjusted for code Doppler according to the test Doppler value, so the sum is performed across an integer number of code periods. The first and third sums are then added together non-coherently (i.e., the magnitudes are summed, no longer preserving phase between them) and compared to the non-coherent addition of the second and fourth coherent sums. Each coherent sum is half the duration of a navigation bit, so one of the non-coherent sums is guaranteed to be free of navigation bit transitions, providing increased SNR for estimating τ and ω_D.

Doppler and delay search results from the maximum coherent sum pair are used to form estimates. As discussed above, due to the shape of the ambiguity function's Doppler dimension, Doppler must be searched with a minimum resolution of $1/(2T_I)$. RNS SDR uses a 5 Hz frequency step over a span of ± 175 Hz, centered around the STK Doppler prediction for HSM4 data. When other data is used and the frequency span is larger, a step size of 250 Hz is used an approximation of finer search grid is achieved through

$$z_{\text{fine}}(\tilde{\tau}, \tilde{\omega}_D) = \exp(j\Delta\hat{\omega}_D \bar{t}_\ell) z(\tilde{\tau}, \tilde{\omega}_D) \tag{2.18}$$

where $\bar{t}_\ell$ is the midpoint of the ℓ-th accumulation as detailed in [23].

The process of correlating a local copy with the input signal itself effectively searches all possible delays with a resolution corresponding to the input signal sample rate, f_s. C/A codes are pre-generated and read from a file for speed. The circular correlation of two finite and equal length sequences $x[n]$ and $y[n]$ is equivalent to

$$Z(k) = X^*(k)Y(k), \tag{2.19}$$

where $X^*(k)$ is the complex conjugate of the frequency domain representation of $x[n]$, and $Y(k)$ is the frequency domain represenation of $y[n]$. Using this relationship, the C/A code can be efficiently correlated by taking the Fast Fourier Transform (FFT) of the received signal after carrier removal and multiplying it by the complex conjugate of the FFT of the locally generated code. The peak corresponding to the delay offset of the local and received codes can be found through the Inverse Fast Fourier Transform (IFFT).

The method of determining C/N_0 during acquisition is only an approximation. Correlation is performed over a range of frequencies to form the statistic $z^j(\tilde{\tau}, \tilde{\omega}_D)$ using the C/A code for a non-visible satellite j. Due to the cross correlation properties of the codes, this produces only noise. The average over delay and Doppler of the magnitude squared (or power) of $z^j(\tilde{\tau}, \tilde{\omega}_D)$ is taken to be the noise floor, N_0. The carrier to noise spectral density of satellite j, $(C/N_0)^i$, is approximated as the ratio of the magnitude squared of $z^i(\tilde{\tau}, \tilde{\omega}_D)$ to N_0 divided by T_I,

$$\left(\frac{C}{N_0}\right)^i = \frac{|z^i(\tilde{\tau}, \tilde{\omega}_D)|^2}{T_I \text{mean}(|z^j(\tilde{\tau}, \tilde{\omega}_D)|^2)}. \tag{2.20}$$

This result is compared with the user-specified threshold in order to evaluate visibility. A more accurate and precise measurement is determined during the subsequent tracking procedure.

2.3.3 Tracking

After all visible satellites are acquired, the desired signals can be tracked. Satellites to be tracked are specified in the RNS SDR settings. If determined visible by acquisition, these are processed serially. Tracking starts at the sample in the data file corresponding to the start of the next C/A code period, as determined from the acquisition delay estimate. The tracking loop continues for the specified time duration. After all satellites are processed, the results are plotted. Loop lock occurs in 1 second or less, depending on signal strength, but the C/N_0 estimate takes approximately six seconds to settle.

The goal of tracking is to refine the delay and Doppler estimates produced by acquisition. In short, this involves correlating the input signal with a local replica and filtering the results to produce error terms that quantify the difference between the local replica and the actual input signal. A feedback process makes adjustments to the local signal replica according to the code delay and frequency error terms. In addition to converging on the input signal parameters τ and ω_D, the tracking of the dynamic signal allows for measurements of changing signal features and more accurate measurements of C/N_0 than possible with acquisition. Tracking is achieved using a phase lock loop (PLL) for the carrier and a carrier-aided delay lock loop (DLL) for the code.

Phase Lock Loop

The PLL is characterized by its loop discriminator and loop filters. At the start of tracking, a local carrier is generated at a frequency equal to $\omega_{IF} + \tilde{\omega}_{D,k}$. This finite-length signal is multiplied by an input signal of the same length and a sampled version of the C/A code, delayed (via a circular shift) according to $\hat{\tau}_k$, to form the k-th prompt correlation

$$e_{P,k} = \sum_{i=i_k}^{i_k+N_k-1} y_i p(t_i - \hat{\tau}_k) \exp(-j(\omega_{IF} t_i + \hat{\phi}_k + \hat{\omega}_k(t_i - \hat{\tau}_k))). \tag{2.21}$$

The number of samples in the correlation, N_k, is determined by T_I and the compression or expansion of the C/A code periods by the Doppler shift. The prompt correlator output is a complex signal consisting of in-phase and quadrature components $e_{PI,k}$ and $e_{PQ,k}$. As such, $e_{P,k}$ contains information about the frequency difference between the locally generated carrier and the received signal. This is translated into an error term by the loop discriminator,

$$\epsilon_{carr,k} = \arctan\left(\frac{e_{PQ,k}}{e_{PI,k}}\right). \tag{2.22}$$

The loop filter is designed to make phase adjustments to the local oscillator (i.e., the frequency of the locally generated carrier) on the basis of the discriminator output such that $\epsilon_{carr,k}$ is driven to zero. In the RNS SDR, this discriminator output is filtered by the third-order loop filter shown in Figure 2.3 and fed back to the carrier generator as a correction $\omega_{IF} + \hat{\omega}_k$ [24]. A third order filter is used to handle the high dynamics present in HSM4.

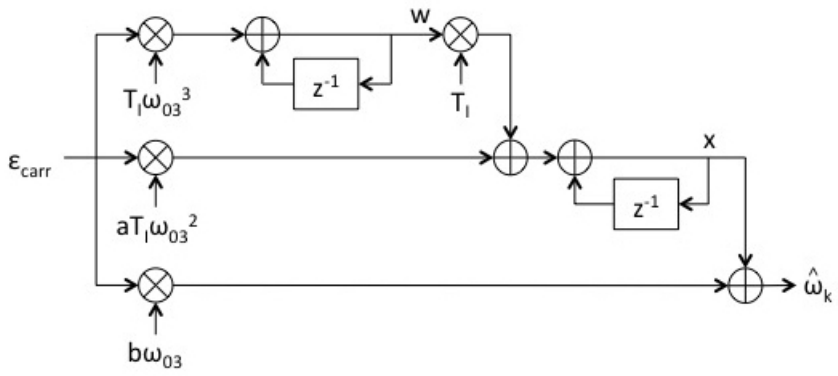

Fig. 2.3. PLL loop filter

The transfer function of the loop filter in the z domain is

$$H(z) = T_I^2\omega_{03}^3(1+z^{-1})^2 + aT_I\omega_{03}^2(1+z^{-1}) + b\omega_{03}, \tag{2.23}$$

where ω_{03}^3 is the natural frequency of the filter and a and b are adjustable parameters. Loop bandwidth is an important factor in PLL noise performance; a wider bandwidth is less susceptible to high dynamics but a narrower bandwidth is more robust if the

signal is weak. The filter parameters are adjusted to achieve a loop bandwidth B_n that accommodates these factors based on the integration time used (in general, $T_I = 1$ ms for strong signals and $T_I = 20$ ms for weak signals). Bandwidth is calculated

$$B_n = \frac{1}{2\pi} \int_0^\infty |H(\omega)|^2 \, d\omega. \tag{2.24}$$

Recall that $H(\omega) = H(z)|_{z=e^{j\omega}}$. The integral in Equation (2.24) can be solved using contour integration and Cauchy's integral formula [25].

A key performance metric of the PLL is its carrier loop thermal noise error. A 1-sigma rule-of-thumb bounds the standard deviation of the PLL to less than or equal to 15° in order to maintain lock. Breaking the PLL standard deviation into its components, this means

$$\sigma_{PLL} = \sqrt{\sigma_{t,PLL}^2 + \sigma_v^2 + \theta_A^2} + \theta_e/3 \leq 15^\circ \tag{2.25}$$

must hold to maintain carrier lock [24]. Here, $\sigma_{t,PLL}^2$ is the thermal noise jitter, σ_v^2 is the vibration induced oscillator jitter, θ_A^2 is the Allan variance induced oscillator jitter and θ_e is the dynamic stress error.

Thermal noise is the only factor of significance in the case of HSM4, as the latter quantities are either relatively small (in the case of oscillator jitters), or depend on higher-order dynamics, such as jerk, that are not a concern (in the case of the dynamic stress error). Thermal noise jitter depends on the carrier loop noise bandwidth, carrier to noise spectral density, and pre-detection integration time according to

$$\sigma_{t,PLL} = \frac{360}{2\pi} \sqrt{\frac{B_n}{C/N_0} \left(1 + \frac{1}{2T_I C/N_0}\right)}, \tag{2.26}$$

where the coefficient of $360/(2\pi)$ degrees per radian is used to produce a noise jitter in units of degrees. The condition for PLL lock, then, is that the following hold:

$$\sigma_{PLL} = \frac{360}{2\pi} \sqrt{\frac{B_n}{C/N_0} \left(1 + \frac{1}{2T_I C/N_0}\right)} \leq 15^\circ. \tag{2.27}$$

Delay Lock Loop

As with the PLL, the DLL is characterized by its loop discriminator and loop filters. The basic process is similar to that used in carrier tracking: the correlation between an input signal and a locally generated signal is translated into an error term by the loop discriminator and this is used to correct the local signal generation via loop filters to reduce the error.

Code tracking is performed on the baseband signal,

$$y_{b,i} = y_i \exp(-j(\omega_{IF} t_i + \hat{\phi}_k + \hat{\omega}_k(t_i - \hat{\tau}_k))), \tag{2.28}$$

by forming the correlations between two locally generated codes - an early and a late code. The k-th early and late correlations are, respectively,

$$e_{E,k} = \sum_{i=i_k}^{i_k+N_k-1} y_{b,i} p(t_i - \hat{\tau}_k + \frac{d}{2} T_c), \tag{2.29}$$

$$e_{L,k} = \sum_{i=i_k}^{i_k+N_k-1} y_{b,i} p(t_i - \hat{\tau}_k - \frac{d}{2} T_c), \tag{2.30}$$

where d is the offset of the two correlations in chips, i.e., the early-late correlator spacing.

The result of these correlations can be understood intuitively through Figure 2.4, where the magnitudes of the complex quantities e_E and e_L are plotted against delay error $\Delta\tau = \tau - \tilde{\tau}$ for $d = 1$ chip. In Case A the estimated code delay is a chip less than the true delay and the received code arrives later than estimated, maximizing the late correlator. The early code, however, is offset by a full chip, yielding a magnitude of zero due to the C/A code cross correlation properties. Case B shows when both the early and late codes are a half chip offset from the input data, resulting in equal magnitudes at half the maximum. When the early code is perfectly aligned with the input data Case C occurs: $|e_L| = 0$ and $|e_E|$ is maximized.

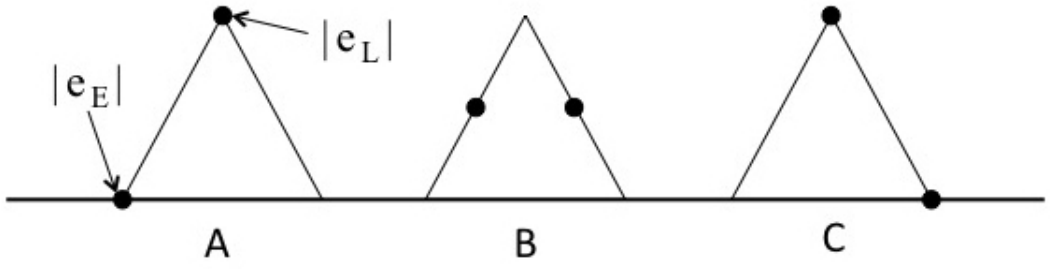

Fig. 2.4. Case A: $\hat{\tau} = \tau - dT_c$ Case B: $\hat{\tau} = \tau$ Case C: $\hat{\tau} = \tau + dT_c$

The local code is perfectly aligned with the input data when the correlations are equal, as in Case B, so the error must be zero when $|e_E| - |e_L| = 0$. The loop discriminator is normalized so as to range over $[-1, 1]$. For a noncoherent discriminator,

$$\epsilon_{code} = \frac{|e_E| - |e_L|}{|e_E| + |e_L|} = \frac{\sqrt{e_{E,I}^2 + e_{E,Q}^2} - \sqrt{e_{L,I}^2 + e_{L,Q}^2}}{\sqrt{e_{E,I}^2 + e_{E,Q}^2} + \sqrt{e_{L,I}^2 + e_{L,Q}^2}}. \tag{2.31}$$

A noncoherent discriminator is used in the RNS SDR with $d = 1$. The noise performance of the discriminator is determined by the early-late correlator spacing - notice that changing d changes the slope of the discriminator and, in turn, the discriminator's tolerance to large errors in $\hat{\tau}$. Increasing d enables the loop to handle higher dynamics and noise, but is less precise. If the carrier were perfectly aligned, it would be sufficient to compare the early and late correlations of only the in-phase branch. Using (2.31) makes the DLL operation theoretically independent of PLL lock. The normalized power difference enables the DLL to track signals with different strengths and C/N_0 levels better than simply using $\epsilon_{code} = |e_E| - |e_L|$ would [26].

The loop filter seeks to track the null of the discriminator, adjusting $\hat{\tau}$ to achieve Case B. A first order DLL is used, so the transfer function is simply $H(z) = -\omega_0$. This term, the loop's natural frequency, is chosen to obtain a desired noise bandwidth B_n where $B_n = \omega_0/4$, computed using (2.24). The output of the loop filter is used to adjust the local code chip frequency via

$$f_{chip} = u + (1 + \frac{x}{2\pi f_{L1}}) f_{chip,nominal}. \tag{2.32}$$

The nominal chip frequency is 1.023 MHz and x is the L1 Doppler frequency calculated by the PLL loop filter (see Figure 2.3). In Equation (2.32), x is converted to the chip frequency Doppler shift. This is added to the nominal chip frequency. Thus, u is an adjustment above or below the frequency estimate from carrier tracking [24].

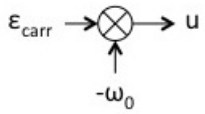

Fig. 2.5. DLL loop filter

2.3.4 C/N_0 Estimation

The RNS SDR method of estimating carrier to noise spectral density is an iterative procedure, based on a method employed in GSFC's Siggen tracking utility. For accumulation k of the tracking loop, the C/N_0 is estimated as

$$\left(\frac{\hat{C}}{N_0}\right)_k = 10\log_{10}\left(\frac{1}{2T_I}\left(\frac{z_{I,var}[k]}{z_{Q,var}[k]} - 1\right)\right) \tag{2.33}$$

where $z_{I,var}[k]$ and $z_{Q,var}[k]$ are the estimated variance of the in-phase and quadrature components of e_p respectively. Following [19], these are computed according to

$$z_{I,var}[k] = \alpha\beta\left(\sum_{i=i_k}^{i_k+N_k-1} I_{i_k}\right)^2 + (1-\alpha)z_{I,var}[k-1], \tag{2.34}$$

$$z_{Q,var}[k] = \alpha\beta\left(\sum_{i=i_k}^{i_k+N_k-1} Q_{i_k}\right)^2 + (1-\alpha)z_{Q,var}[k-1], \tag{2.35}$$

for accumulation k and samples N_k. The filter parameters α and β depend on the value of T_I. For $T_I = 1$ ms, $\alpha = 1/128$ and $\beta = 1$. For $T_I = 20$ ms, $\alpha = 1/32$ and $\beta = 1/256$.

2.4 Other Receivers Used

Two other SDRs were used in this dissertation, both developed by engineers in Code 596 at GSFC. These receivers provided independent testing and validation during the development of RNS SDR, as well as certain additional capabilities. The custom RNS SDR is used for results presented throughout this dissertation, however, unless stated otherwise.

2.4.1 NavSDR

The Navigator GPS Receiver is a receiver designed by engineers at GSFC for space-based platforms [4]. It incorporates numerous techniques to overcome challenges that arise in space applications, such as weak signals, ionospheric scintillation, and high receiver velocity. A software version of Navigator, the GSFC NavSDR, was used to perform conventional tracking of all the rendezvous data, taking advantage of the receiver's sophisticated space-specific features and history of testing and validation.

2.4.2 Siggen

In addition to the signal simulation features described in Section 5.2, GSFC's Siggen includes a tracking script. This was primarily used to validate RNS SDR measurements during development and more than once uncovered important errors, particularly in code phase and pseudorange measurements.

2.5 Pseudorange

The fundamental measurements of a GPS receiver described above are used to calculate pseudorange. Pseudorange is distinguished from range because it is a measure of the distance between the transmitting satellite and receiver that is biased by the transmitter and receiver clocks. Distance to the i-th satellite can be calculated

as the difference between the times of transmission and reception, multiplied by the nominal signal propagation rate c to get units of distance,

$$\rho^i = c(t_r - (t_s^i - \tau^i)) + \epsilon^i. \tag{2.36}$$

Error in the pseudorange is represented by ϵ^i, t_r is the time of reception according to the receiver clock, and t_s^i is the time of reception according to the clock on the transmitting satellite. If the time of propagation was τ^i, then $(t_s^i - \tau^i)$ was the time of transmission according to the satellite clock. Both the satellite and receiver clocks are biased relative to the reference GPS time, $t_r = t_{GPS} + t_{b,R}$ and $t_s^i = t_{GPS} + t_{b,s}^i$, where t_{GPS} is the GPS time standard and $t_{b,R}$ and $t_{b,s}^i$ are the receiver and satellite clock biases. The time of propagation is the result of the geometric range between the satellite and receiver and delays due to the atmosphere,

$$\tau^i = (r^i + I_{L1}^i + T^i)/c, \tag{2.37}$$

where r^i is the geometric range between the satellite and receiver, I_{L1}^i the delay due to the ionosphere, and T^i the delay due to the troposphere. The ionosphere is a region of ionized gas in the upper atmosphere where the time varying density of free electrons and ions introduces a dispersive (i.e., frequency dependent) delay. This does not delay the different components of the GPS signal equally, but for simplicity the delay on the L1 frequency is used here. The troposphere, consisting of dry gases and water vapor, is not a dispersive medium.

Substituting t_r, t_s^i and τ^i into Equation (2.36), pseudorange can be written,

$$\rho^i = r^i + ct_{b,R} - ct_{b,s}^i + I_{L1}^i + T^i + v^i, \tag{2.38}$$

where the time dependence of all terms is suppressed for notational simplicity. In order to form a pseudorange measurement, the navigation message must be decoded. The message is organized into six second subframes, each beginning with an eight bit Telemetry word (TLM) and Hand-over word (HOW), the latter of which contains the satellite time the subframe was transmitted. The position of the code tracked

by the receiver relative to the subframe start is used to determine the transmission time (according to the satellite clock) of a given sample and, through a comparison to the time of reception of that sample (according to the receiver clock), to calculate the time of propagation. This is covered in more detail in [12], but it is ultimately the combination of pseudorange measurements from four or more satellites that is used to solve for a receiver's position [21]. This concept is revisited in Chapter 7 incorporating reflected signals.

3. MULTIPATH AND RELATIVE NAVIGATION

3.1 Electromagnetic Propagation

The propagation of electromagnetic energy is described by Maxwell's Equations. In free space (i.e., in the absence of free charges or currents), these equations can be written

$$\nabla \times \vec{E} = -\mu \frac{\partial \vec{H}}{\partial t} \tag{3.1}$$

$$\nabla \times \vec{H} = \epsilon \frac{\partial \vec{E}}{\partial t} \tag{3.2}$$

$$\nabla \cdot \epsilon \vec{E} = 0 \tag{3.3}$$

$$\nabla \cdot \mu \vec{H} = 0 \tag{3.4}$$

where $\vec{E}$ is the electric field and $\vec{H}$ is the magnetic field. These fields can be written in terms of rectilinear components, $\vec{E} = E_x\hat{i} + E_y\hat{j} + E_z\hat{k}$ and $\vec{H} = H_x\hat{i} + H_y\hat{j} + H_z\hat{k}$, where $\hat{i}$, $\hat{j}$, and $\hat{k}$ are the unit vectors in the x, y, and z directions respectively. The electrical permittivity and magnetic permeability of the propagation medium are given by ϵ and μ respectively. The $\times$ symbol indicates the vector cross product, and $\cdot$ the vector dot product. The del "operator" is the vector differential operator $\nabla = \frac{\partial}{\partial x}\hat{i} + \frac{\partial}{\partial y}\hat{j} + \frac{\partial}{\partial z}\hat{k}$, so that $\nabla\times$ as used above represents the vector curl operation and $\nabla\cdot$ the vector divergence.

For a linear, isotropic, homogenous and nondispersive medium, Maxwell's Equations can be shown to reduce to a scalar wave equation [27] [28]. A rearrangement of the equations produces the vector wave equation describing propagation of an electric field in a homogenous (constant ϵ) medium,

$$\nabla^2 \vec{E} - \frac{n^2}{c^2}\frac{\partial^2 \vec{E}}{\partial t^2} = 0. \tag{3.5}$$

Here n is the refractive index of the medium, $n = (\epsilon/\epsilon_0)^2$, and c is the velocity of propagation in a vacuum, $c = 1/\sqrt{\mu_0\epsilon_0}$. Both ϵ_0 and μ_0 are reference values, the permittivity and permeability of a vacuum. Significantly, Maxwell's Equations can also be rearranged to produce an identical wave equation for the magnetic field,

$$\nabla^2\vec{H} - \frac{n^2}{c^2}\frac{\partial^2\vec{H}}{\partial t^2} = 0.$$

Because both the electric and magnetic field follow the vector wave equation, the field components propagate according to a scalar wave equation of the same form. By substituting $u(\vec{r},t)$ for any scalar field component, a single scalar wave equation can be used to describe the electric and magnetic vector fields,

$$\nabla^2 u(\vec{r},t) - \frac{n^2}{c^2}\frac{\partial^2 u(\vec{r},t)}{\partial t^2} = 0. \tag{3.6}$$

The scalar field is dependent on position $\vec{r}$ and time t. Without loss of generality, we can establish the coordinate system such that the electric field is propagating along the z axis. The x and y components of an electric field propagating along the z axis must each satisfy the scalar wave equation.

One solution to the wave equation of interest in the present work is the linear combination of two wave functions in the $\hat{i}$ and $\hat{j}$ directions (relying on the assumption of a linear medium). If these wave functions are chosen to be identical cosine functions, the electric field can be written [29]

$$E(z,t) = E_x\cos(\omega t \pm kz)\hat{i} + E_y\cos(\omega t \pm kz - \omega t_0)\hat{j}.$$

The reference time t_0 is arbitrary, so if it is selected so the spatial displacement, z, relative to the coordinate system origin is zero, then

$$E(t) = E_x\cos(\omega t)\hat{i} + E_y\cos(\omega t - \psi)\hat{j}. \tag{3.7}$$

Here ω is the wave frequency in radians per second, E_x and E_y are the magnitudes of the x and y electric field components, respectively, and $\psi = \omega t_0$ is the phase offset of the wave function in the y direction relative to that in the x direction. This phase

offset determines the polarization of the electric field. The signal transmitted by a GPS satellite is circularly polarized, and specifically right hand circularly polarized (RCP), so $\psi = \pi/4$:

$$E_{RCP}(t) = E_x \cos(\omega t)\hat{i} + E_y \sin(\omega t)\hat{j}. \tag{3.8}$$

In this case the resulting electric field traces out a circle on the x-y plane, moving clockwise when looking along the z axis in the direction of propagation.

The received "signal" in Equation 2.1 is then no more than a polychromatic wave representation of this scalar electric field. This is the electromagnetic disturbance at the receiving antenna arriving along the direction of the line of sight between the antenna and the transmitting GNSS satellite (including the effect of antenna polarization). In this way, the propagating electric field is approximated as a ray - a vector in space along the direction of propagation. However, the scalar wave equation is just an approximation that relies on the assumptions made above about the propagation medium. The approximation breaks down, for instance, when boundary conditions are applied to the field, as in the interaction of the field with obstructing surfaces and objects. The errors introduced extend only a few wavelengths from the boundary condition, however, and so remain tolerable as long as the object dimensions are large relative to the signal wavelength.

This representation of the propagating field as a ray is known as geometrical optics (GO). As long as the wavelength condition is met, the interaction of this ray with surfaces and different mediums is described by the GO laws of reflection and refraction. The Geometrical Theory of Diffraction expands the GO laws to handle complex bodies by introducing diffraction to describe the scattering of rays at edges [30] [31]. The Uniform Geometrical Theory of Diffraction (UGTD) further refines this description by introducing a more precise diffraction coefficient in transition regions adjacent to shadow and reflection boundaries.

A ray is more rigorously defined in GO as the trajectory satisfying the Fermat principle [31], that the path taken by a ray is the path that can be traveled in the least amount of time. When the electrical properties of an environment are fully

defined, EM ray tracing can be used to determine the path taken by an EM ray. EM ray tracing is used in this dissertation to model the GNSS rays scattered by a target spacecraft during docking.

3.2 Bistatic Radar

The concept of ranging from a reflected RF signal is known as radar. When introduced in 1940, radar was an acronym for RAdio Detection And Ranging, but has since become a common noun. The particular case of interest for ranging during spacecraft proximity operations is known as bistatic radar. As illustrated in Figure 3.1 for the case of HSM4, this involves a receiver and transmitter that are in separate locations. The signal transmitted by the GNSS satellite travels along the R_T direction, reflects off HST, and travels along the R_R direction to the receiver in the space shuttle cargo bay.

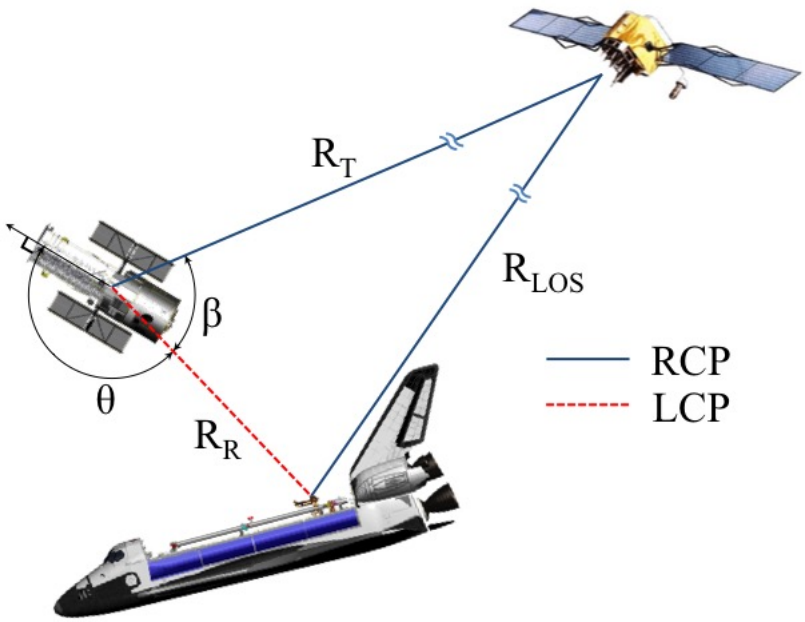

Fig. 3.1. Bistatic radar using direct and reflected GNSS signals during HSM4

The ranging properties of GNSS signals described in Chapter 2 allow the distances traveled by each signal to be measured. By computing the propagation path length of signals reflected off the same target from several GNSS satellites, the target location can be estimated. This is described below in Section 3.4. Detection of a reflected signal relies on sufficient received power.

3.2.1 Direct Signal

The received direct signal power, inclusive of the receiver antenna gain and receiver losses, is calculated as

$$P_{R,direct} = \mathcal{P}_{T,rcvr} A_R \quad [W], \tag{3.9}$$

where $\mathcal{P}_{T,rcvr}$ is the power spatial density produced by the transmitter at the receiver in Watts per square meter, and A_R is the effective area, or aperture, of the receive antenna in square meters. The effective area of the receive antenna is a measure of the antenna's ability to capture power in an electric field incident on the antenna from a certain direction, defined as

$$A_{eff} = \frac{G\lambda^2}{4\pi} \quad [m^2], \tag{3.10}$$

where G is the antenna's gain over an isotropic radiator and λ the signal wavelength (19 cm for GPS).

An isotropic antenna radiates power equally in all directions. At a given distance from the transmitter, R, this power is spread uniformly over a sphere of the same radius. Thus, the power density at R, in power per square meter, is simply the transmitted power divided by the surface area of the sphere: $P_T/(4\pi R^2)$. This accounts for the spreading loss. Spreading loss can be offset by focusing the transmitted power in a particular direction, a property described by the transmit antenna gain, G. The GPS satellites under consideration have antennas biased toward the earth, with a beamwidth of $\pm 21.3^\circ$ from the antenna boresight. Although the resulting gain is a function of azimuth and elevation, a constant 14.7 dB can be used; the signal transmission is designed to be stronger at larger angles to compensate for the increased

range [12]. By the reciprocity theorem of antennas, an antenna's transmit gain also describes its ability to focus received power, so $G = 4\pi A_{eff}/\lambda^2$, regardless of whether the antenna in question is transmitting or receiving.

Regarding atmospheric losses as negligible, the power density at the receiver can be written as

$$\mathcal{P}_{T,rcvr} = \frac{P_T G_T}{4\pi R_{LOS}^2} \quad [W/m^2]. \tag{3.11}$$

for the particular case of GPS transmitter gain G_T, transmitted power P_T, and line of sight (LOS) range R_{LOS}. For receiver gain G_R,

$$P_{R,direct} = \frac{P_T G_T G_R \lambda_{L1}^2}{(4\pi R_{LOS})^2} \quad [W], \tag{3.12}$$

This is a form of the well-known Friis transmission equation, and is valid when $R_{LOS} \geq 2a^2/\lambda$, where a is the largest linear dimension of either antenna [32]. The Friis equation follows from scalar diffraction theory, and so depends on conditions discussed above for which scalar diffraction is a valid approximation (i.e., large diffracting structures compared with the signal wavelength, and a linear, isotropic, homogeneous, nondispersive medium) [28].

3.2.2 Reflected Signal

In the case of monostatic radar, where the receiver and transmitter are collocated, the received power can be calculated via the radar equation,

$$P_{R,refl} = \mathcal{P}_{T,targ} \cdot \sigma_m \cdot \frac{1}{4\pi R_T^2} \cdot A = \frac{P_T A^2 \sigma_m}{4\pi \lambda^2 R_T^4} \quad [W]. \tag{3.13}$$

The first term, $\mathcal{P}_{T,targ}$, is the power spatial density produced by the transmitter at the target (e.g., HST). This is identical to (3.11) but for the range R_T rather than R_{LOS}. The monostatic radar cross section (RCS) of the target, σ_m, quantifies the amount of incident power that is scattered back in the direction of the receiver in units of square meters. An additional spreading loss term is added to account for losses from the reflecting target back to the transmitter/receiver location, and the effective area of the transmitting and receiving antenna is represented by A.

The calculation of received signal power in the bistatic radar case takes the same form,

$$P_{R,refl} = \mathcal{P}_{T,targ} \cdot \sigma_B \cdot \frac{1}{4\pi R_R^2} \cdot A_R \quad [W],$$

where the bistatic radar cross section is denoted σ_B in square meters. The spreading loss term accounts for losses from the target to the receiver, and A_R is the effective area of the receiving antenna. Substituting $\mathcal{P}_{T,targ}$ gives the bistatic radar equation [33]:

$$P_{R,refl} = \frac{P_T G_T G_R \lambda_{L1}^2 \sigma_b}{(4\pi)^3 R_T^2 R_R^2} \quad [W]. \tag{3.14}$$

The bistatic RCS describes the scattering properties of the target and is a function of the target's material, shape, and orientation relative to the transmitter and receiver. In the bistatic case, this is a function of the incident angle and the angle to the receiver line-of-sight relative to the target body frame, as indicated by the angles θ and β in Figure 3.1. The scattering properties can be broadly broken into three regions according to the magnitude of the bistatic angle β. In order of increasing β, these are the pseudo-monostatic, bistatic, and forward-scattering regions [34]. This simplified treatment has limited use, however. An analytic model of a structure like HST is complicated, involving the decomposition of the target into simple shapes for which closed form scattering formulas exist. A further discussion of this analytic approach is provided in Appendix B, but given the high dynamics and multi-faceted structures involved in HSM4, such calculations are prohibitively complex and slow. In this dissertation, numerical EM ray tracing is primarily used to determine the signals scattered by HST.

3.2.3 Carrier to Noise Spectral Density

Received signal power P_R can be related to C/N_0 by dividing by the noise power per frequency unit,

$$N_0 = kT_{Eff}. \tag{3.15}$$

Here k is Boltzmann's constant and T_{Eff} the total effective noise temperature of the receiver (in Kelvins) [16]. Effective noise temperature includes the receiver noise fig-

ure, ambient temperature, and receiver implementation losses (e.g., A/D conversion). This is related to SNR by

$$\frac{C}{N_0} = SNR + B = (P_R - B - N_0) + B \quad \text{[dB-Hz]}, \tag{3.16}$$

where B is the two-sided receiver filter bandwidth. Unlike SNR, C/N_0 is independent of the receiver bandwidth - it is a power to noise density per unit frequency.

3.3 GNSS Multipath

Reflected signals can be a significant source of error in GNSS measurements. In order to calculate a receiver's position, the time of travel for LOS signals must be determined from at least four satellites. When a large object is located near the receiver, reflections of the GNSS signals may also be received. These delayed, attenuated replicas of the LOS signals contribute erroneous time of travel information to the receiver's position calculation, an error called multipath.

Multipath modeling efforts fall into two broad categories: those that seek to model the receiver errors produced by multipath (e.g., [35], [8], and [7]), and those that seek to model properties of the multipath signals themselves (e.g., [36], [1] and [37]). This latter category is most relevant to the work presented here; in order to estimate environment features from multipath (such as the distance of a reflecting target spacecraft from a receiver), it is necessary to characterize the relationship between the environment features of interest and the observable multipath signal properties.

The Multipath Estimation Delay Lock Loop (MEDLL) is an important method of this class. The algorithm directly estimates the components of each recieved multipath ray using maximum likelihood criteria, essentially performing a nonlinear curve fit of the measured correlation function to find the number of rays and amplitude, phase, and delay of each [36]. Psiaki et al. expanded the MEDLL model of multipath to estimate multipath features from antenna motion [17]. An expression for LOS complex accumulations was introduced in Section 2.2.2 based on this previous work, and is here extended to include multipath.

Ignoring the navigation message and satellite superscripts, the received signal in Equation (2.1) with multipath can be written

$$y(t) = \sum_{m=0}^{M} a_m(t) p(t - \tau_m(t)) \cos(2\pi(f_{L1} + f_{D,m})t + \theta_m(t_0)) + v_m(t). \tag{3.17}$$

for M multipath rays. The LOS signal is assigned the index $m = 0$, while the reflected signals are indexed from $m = 1$ to M. Therefore, assuming an RCP antenna, the signal amplitude for $m = 0$ is a function of the antenna's co-polarization gain,

$$a_0(t) = \sqrt{\mathcal{P}_{T,0} G_R \lambda_{L1}^2 / 4\pi} \tag{3.18}$$

where $\mathcal{P}_{T,0}$ is the power spatial density produced by the GNSS satellite at the receiver along the LOS, and G_R depends on the elevation and azimuth of the incoming signal. Notation indicating the time dependence of $\mathcal{P}_{T,0}$ and G_R is left off for simplicity. The signal amplitude for $m \neq 0$ is a function of the antenna's cross polarization gain,

$$a_m(t) = \sqrt{\mathcal{P}_{T,m} G_{R\times} \lambda_{L1}^2 / 4\pi}. \tag{3.19}$$

After the signal is downcoverted to IF, filtered, and sampled, the i-th sample can be written

$$y_i = \sum_{m=0}^{M} a_m(t_i) \Big\{ \tilde{p}_I(t_i - \tau_m(t_i)) \cos(\omega_{IF} t_i + \phi_{NBC,m}(t_i)) + j\tilde{p}_Q(t_i - \tau_m(t_i)) \sin(\omega_{IF} t_i + \phi_{NBC,m}(t_i)) \Big\} + v_m(t_i). \tag{3.20}$$

The k-th in-phase and quadrature accumulations are computed according to Equations (2.9) and (2.10) respectively. If the error in the PLL carrier estimate is indexed by m,

$$f_m(t_i) = \hat{\phi}_{m,k} + \hat{\omega}_{m,k}(t_i - \tau_{m,k}) - \phi_{NBC,m}(t_i) \approx \Delta\phi_{m,k} + \Delta\omega_{m,k}\bar{t}_k, \tag{3.21}$$

and the code correlations are written as a function of the DLL error $\Delta\tau_{m,k} = \tau_{m,k} - \hat{\tau}_k$,

$$\tilde{R}_{m,I}(\Delta\tau_{m,k} + \eta) = \sum_{i=i_k}^{i_k+N_k-1} \tilde{p}_I(t_i - \tau_{m,k}) p(t_i - \hat{\tau}_k - \eta), \tag{3.22}$$

and

$$\tilde{R}_{m,Q}(\Delta\tau_{m,k}+\eta)=\sum_{i=i_k}^{i_k+N_k-1}\tilde{p}_Q(t_i-\tau_{m,k})p(t_i-\hat{\tau}_k-\eta), \tag{3.23}$$

then the complete description of the in-phase accumulation under the influence of multipath is

$$I_k(\eta)=\frac{1}{2}\sum_{m=0}^{M}A_m\Big\{\cos(\Delta\phi_{m,k}+\Delta\omega_{m,k}\bar{t}_k)\tilde{R}_{m,I}(\Delta\tau_{m,k}+\eta) - \sin(\Delta\phi_{m,k}+\Delta\omega_{m,k}\bar{t}_k)\tilde{R}_{m,Q}(\Delta\tau_{m,k}+\eta)\Big\}. \tag{3.24}$$

The quadrature accumulations can be computed in a similar manner, and complex accumulation formed $I_k(\eta)+jQ_k(\eta)$. As discussed previously, the accumulation power is concentrated on the in-phase channel when tracking is locked, but the presence of multipath will cause distortion of the ambiguity function in complex space. An example of this is shown in Figure 3.2, where the solid blue line shows the tracking result for a simulated PRN without multipath. The dashed orange line shows the distorted ambiguity function of a PRN with multipath. Both are complex, due to random noise, but the additional distortion of the multipath-corrupted PRN can be seen in the projections onto the Q-delay plane.

Each multipath ray can be characterized by its amplitude, code phase and carrier phase relative to the LOS signal, denoted α_m, δ_m and ψ_m respectively. The EM ray tracing used in this dissertation characterizes each multipath ray by its relative electric field strength $E_m=\mathcal{P}_{T,m}/\mathcal{P}_{T,0}$. The relationship between the simulated value and the α_m component described above is

$$\alpha_m=\sqrt{E_m\frac{G_{R\times}}{G_R}}=\sqrt{\frac{a_m}{a_0}}, \tag{3.25}$$

where again the antenna gains are azimuth and elevation dependent. Relative code phase is $\delta_m=\tau_m-\tau_0$ and relative carrier phase $\psi_m=\theta_0-\theta_m$.

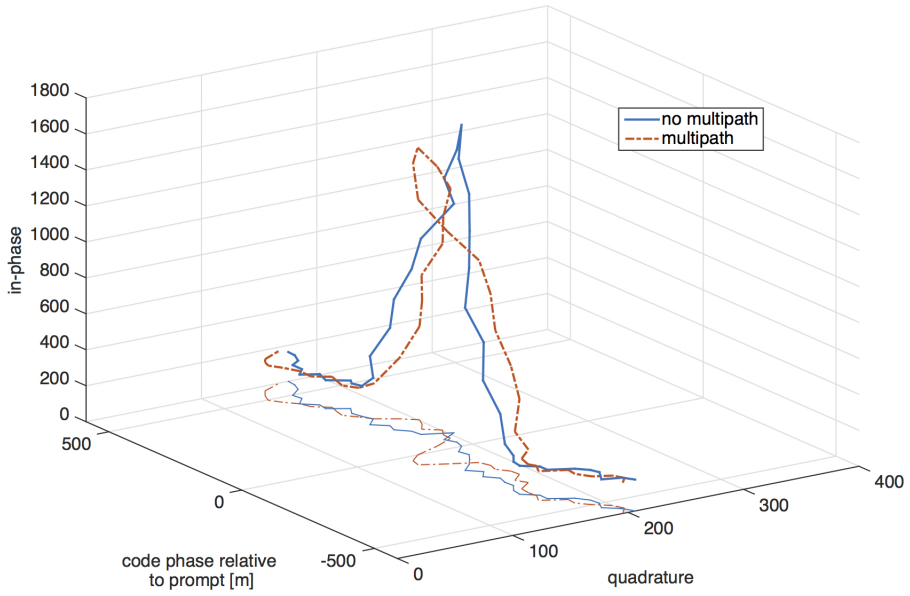

Fig. 3.2. Complex ambiguity function under the influence of multipath (inspired by Figure 2 in [17])

3.4 Use of Multipath in Relative Navigation

Rather than eliminating multipath, this dissertation proposes that these additional ray paths be used as a source of information about the location of the target vehicle relative to the receiver during spacecraft proximity operations. Point positioning using GNSS is achieved by solving, usually in the least-squares sense, the system of pseudorange measurements for the receiver location [21]. The problem can be visualized in two dimensions as shown in Figure 3.3. The transmitting satellites are represented by plus signs. Their positions are known, and pseudorange measurements from each satellite place the receiver on the dashed circles of corresponding radii. The point solution is the intersection of these circles, indicated by an $\mathbf{x}$. The actual problem is complicated by three dimensions (i.e., the point solution is the intersection of spheres), measurement noise, satellite geometry, and overdetermination.

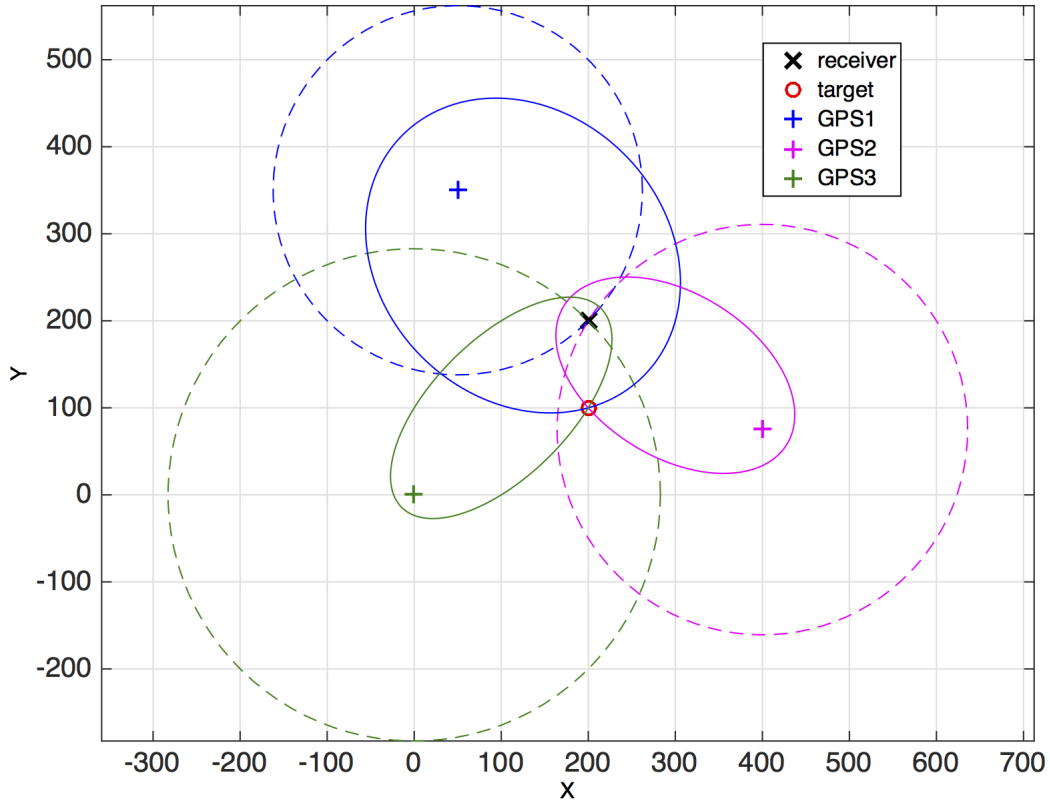

Fig. 3.3. Estimation of target and receiver in two dimensions

A range measurement from a reflected signal from one GNSS satellite constrains the target position to the locus of points for which the sum of the distances from the GNSS satellite to the target and from the target to the receiver is equal to the reflected pseudorange. This corresponds to an ellipse with the target and receiver at its foci. The target position is the intersection of the ellipses corresponding to all of the reflected signal range measurements, shown in Figure 3.3 as a small circle. Again the actual problem involves three dimensions (i.e., the intersection of ellipsoids), variable satellite geometry, and measurement noise.

3.4.1 Previous Work

Calculating range from reflected GNSS signals has been successfully demonstrated in the simpler case of radar altimetry. As with the bistatic radar problem described above, reflected GNSS signals are measured by a receiver and used to measure the distance of the receiver from the reflecting point. The problem is simplified by the reflecting target properties - essentially an infinite plane, albeit with topographical and material variations. In 1994, researchers for Dassault Electronique observed that a GPS-based aircraft tracking system gave an incorrect position estimate when the aircraft was flying over water. Furthermore, they found that the aircraft position errors were related to the aircraft's height above the water surface [38]. Katzberg et al. followed these results in 1999 with a theoretical and experimental study of an altimeter using GNSS reflections over water [39]. Subsequent experiments by other researchers further validated the ocean-reflected GNSS altimeter concept [40] [41]

Masters et al. expanded upon upon the concept in 2001 to consider land reflection, achieving 0.68 m root mean square error (RMSE) for aircraft-based measurements made over the ocean at low altitudes, and an RMSE below 20 m over land [42]. In 2005, Vinande et. al at the University of Colorado used a MATLAB-based software receiver to collect and process data from a similar experimental flight [10]. This experiment successfully measured the aircraft altitude, and observed variations in received signal strength corresponding to ground material reflectivity, highlighting bodies of water below the aircraft. The methods employed were similar to some of those used in this dissertation: a bank of closely spaced correlators in which the correlators of the LCP channel were "slaved in time" to those of the RCP channel. In the aircraft altimeter experiments, it is is important to note that direct and reflected signals were well isolated, not just by differently polarized antennas, but also by antenna placement: LCP antennas were mounted on the bottom of the aircraft, RCP antennas on the top.

The difficulty of reflected-GNSS ranging increases with target complexity, as is evident even in the comparison between ocean and land altimetry [42]. In 1998, Stockmaster et al. used GNSS signals reflected off a cylindrical metal buildling to determine the its range from the receiver [11]. A least squares approach was used to produce a single range measurement from multiple satellite reflections. Reflected signal tracking was initialized with direct signal acquisition results and a target range estimate (accurate to within 150 m). With 1.3 seconds of data, the target range at 36.6 m and 65.5 m was measured to within 1-2 m. Three years later, Treuhaft and others at Jet Propulsion Laboratory (JPL) demonstrated the use of carrier phase techniques to measure the surface of Crater Lake in Oregon with 2 cm precision [43]. A single antenna was used to collect a signal containing both the direct satellite transmission and a component reflected off the lake 480 meters below. Nonlinear parameter estimation was used to estimate the reflected signal properties through 20 ms correlations with a local signal replica.

A patent granted to researchers at The Charles Stark Draper Laboratory in 2004 describes the use of reflected signals for terrestrial vehicle navigation, primarily to overcome signal blockage by terrain or buildings [44]. Tracking of a signal reflected off a mountain or building is performed when the LOS signal is still visible, and a relationship between the two is established. This is then used to estimate LOS measurements if the direct signal becomes blocked. In his 2007 dissertation on spacecraft formation flying, Chris Lane explored the idea of using reflected signals for relative navigation between members of a formation [45]. In a master's thesis that same year, Ian Cohen proposed that GNSS multipath be used as a bistatic radar in spacecraft rendezvous and docking [9] [46] [47]. This concept was the motivation for including RCP and LCP GPS antennas in the RNS experiment described in Chapter 4. The resulting data provided the first opportunity to experimentally study this theory and formed the basis of this dissertation.

4. HUBBLE SERVICING MISSION 4

4.1 Relative Navigation Sensor Experiment

HSM4, or STS-125, was performed in 2009 by the crew of the space shuttle *Atlantis* over the course of thirteen days, from May 11th to May 24th. During HSM4, the Relative Navigation Sensor (RNS) experiment collected several hours of imagery and other data for estimating the space telescope's position and attitude relative to the shuttle cargo bay. The primary objective of the RNS experiment was to compare the performance of several vision processing algorithms: Goddard Natural Feature Image Recognition (GNFIR), both real-time and post-processed, and Ultra Lethal Targeting by Optical Recognition (ULTOR) Passive Pose and Position Engine (P3E) [48]. Three cameras of varying optical ranges were mounted in the shuttle cargo bay to collect images throughout rendezvous and docking [49]. Additionally, two GPS antennas were included as part of this experiment, one right-hand circularly polarized (RCP), optimally polarized for receiving direct signals, the other left-hand circularly polarized (LCP), optimally polarized for receiving reflected signals. Data were collected during the shuttle's rendezvous and docking with HST on May 13th (16:12 - 18:30 UTC), and its deploy of HST on May 18th (10:21- 21:06 UTC). The RNS hardware was mounted in the shuttle cargo bay on the Multi-use Logistic Equipment carrier (MULE), shown in Figure 4.1.

4.2 GPS Data

The received signals were mixed to an intermediate frequency of 604 kHz, sampled at 2.048 MHz, then stored on the Mass Storage Module (MSM) using commercial hard drives at eight bits per sample (four bits real, four bits imaginary). Data were

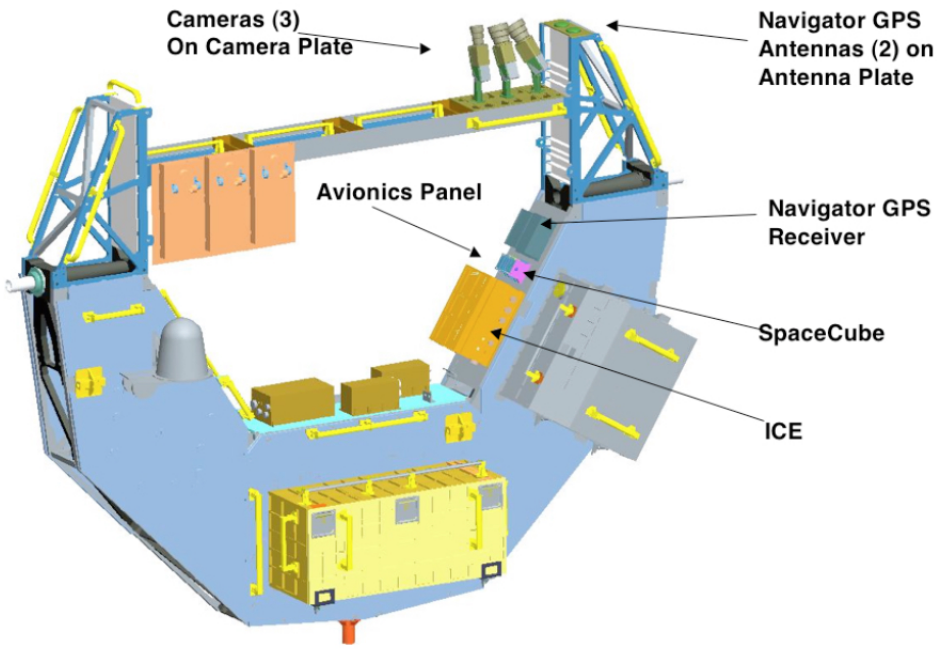

Fig. 4.1. RNS hardware mounting locations on MULE carrier (image from [49])

digitized from the antennas by the Navigator Signal Processor and transferred to the MSM via a high speed serial interface in packets, shown in Figure 4.2(a) [50]. Packets were combined into files, shown in Figure 4.2(b). This file structure is not included in the documentation and was determined experimentally. A bash script was used to call C++ parsing code written by previous researchers, Greg Heckler and Mike Walker. Separate output files were created for RCP and LCP data, each containing three MSM files (152.55 seconds of 16-bit complex data). Data have been parsed for the duration of rendezvous and docking, but deploy data have not yet been processed.

4.3 Antennas

Sensor Systems RCP (Model S67-1575-39) and LCP (Model S67-1575-139) antennas were flown on HSM4 [51]. The antennas were mounted in the shuttle cargo bay on top of the MULE beside the RNS cameras, as indicated by the arrow in Figure

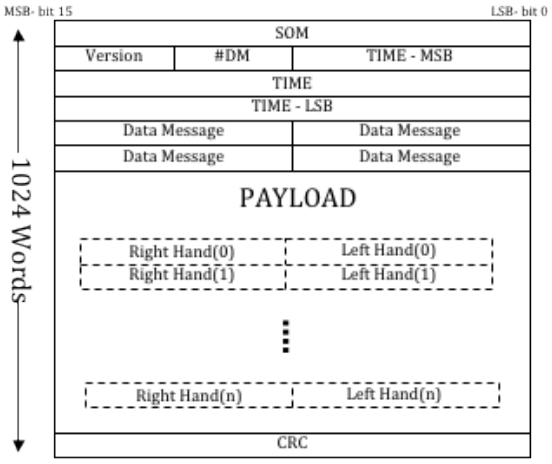

(a) Data packet contents (from [50])

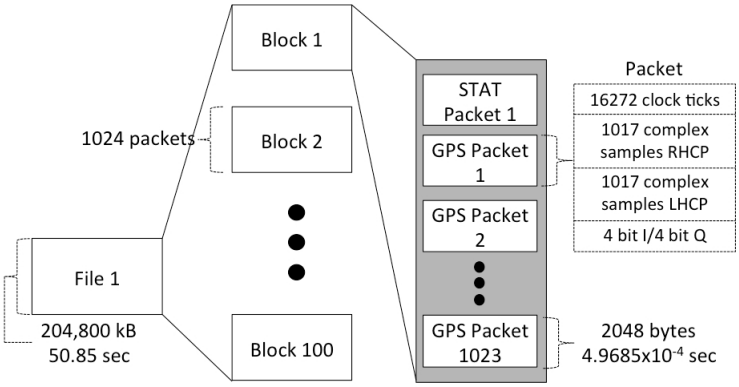

(b) Data file structure

Fig. 4.2. HSM4 file structure

4.3(a). After initial tracking results suggested poor isolation of direct and reflected signals, it was important to determine the cross-pole discrimination of the antennas. The antennas were not measured prior to the mission, but information provided by Sensor Systems suggested only a 3 dB cross-pole attenuation. More accurate measurements were needed. The antenna mounting plate was reconstructed according to HSM4 photographs, and then the flight antenna gain patterns were measured in the Goddard ElectroMagnetic Anechoic Chamber (GEMAC), shown in Figure 4.3(b).

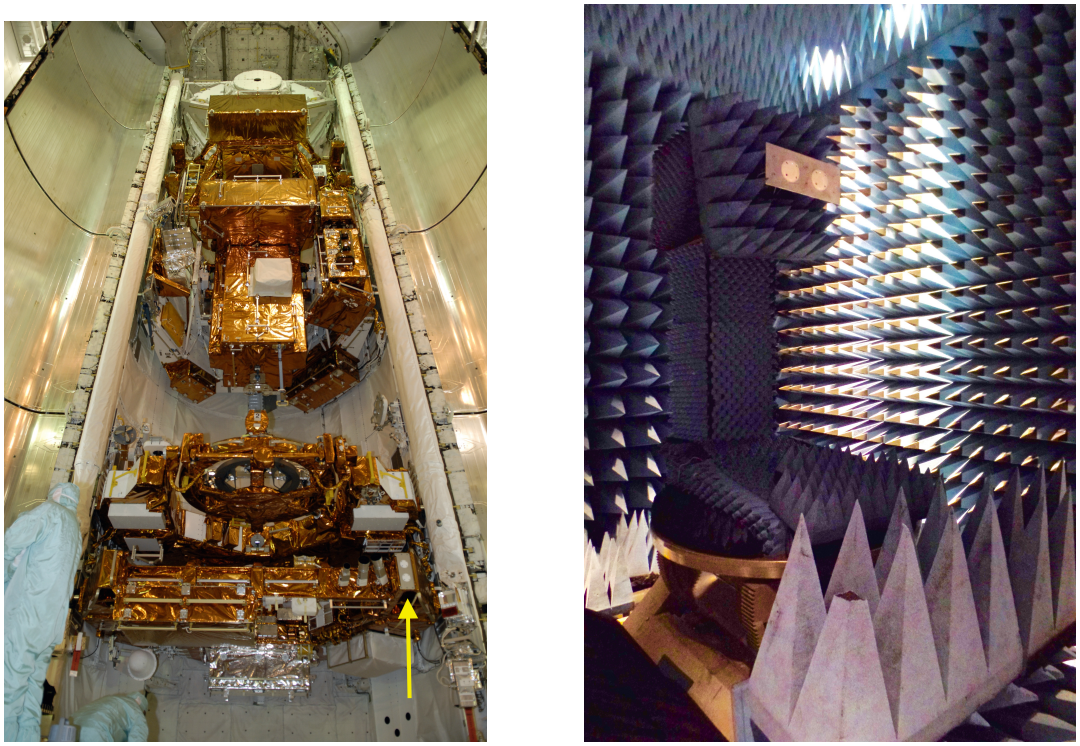

(a) Antenna placement on space shuttle (image from RNS researchers)

(b) Antenna testing in GEMAC

Fig. 4.3. HSM4 flight antennas

Azimuth cuts of the measured gain patterns are shown in Figure 4.4. Measurements were taken across antenna elevation from −179 to 179 degrees in increments of one degree at each antenna azimuth cut. Antenna azimuth was tested from 0 to 180 degrees in increments of 15 degrees. Both antennas are active antennas, but the 26 dB gain of the low noise amplifier has been subtracted. In each case, the co-pole gain is plotted with solid lines and the cross-pole gain with dotted lines. Average gain across the different azimuth cuts is plotted in black; the attenuation of an LCP signal at the RCP antenna boresight is 12 dB, while the attenuation of an RCP signal at the LCP antenna boresight is 7 dB. This is better than the cross-pole attenuation specified by the manufacturer, but the poorer polarization of the LCP antenna causes difficulty in the isolation of LCP signals.

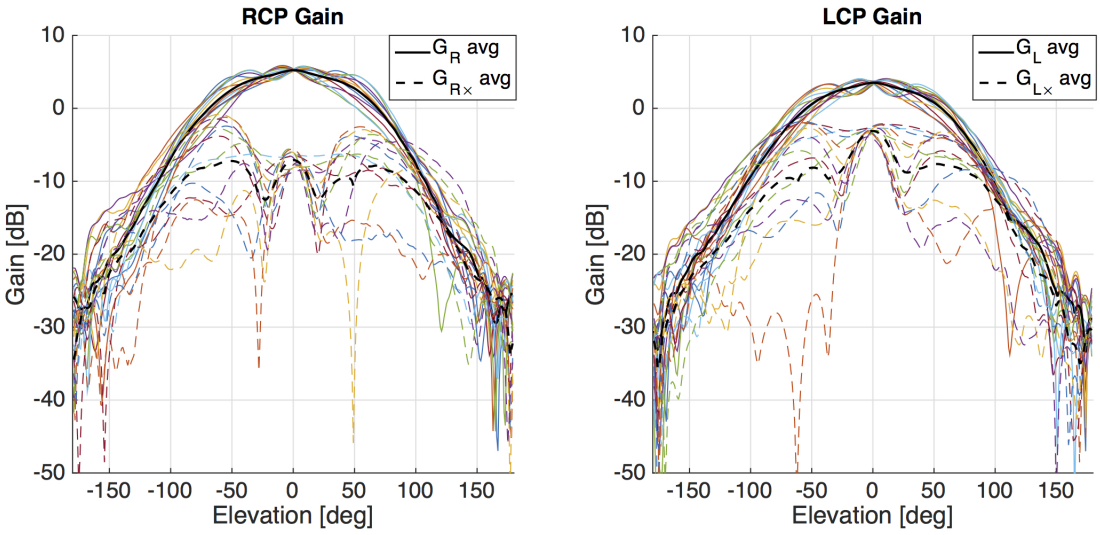

Fig. 4.4. Elevation (solid) and azimuth (dashed) gain cuts of HSM4 antennas measured in GEMAC

Another issue is the large azimuthal variation of the gain patterns. This is especially apparent in the polar gain plots, Figures 4.5 and 4.6, and is likely a ripple due to the size of the ground plane. The ground plane has been constructed to approximately match the antenna mount plate flown on the servicing mission, but the exact dimensions are not known. Furthermore, the antenna order was not recorded (i.e., which antenna was closer to the front of the shuttle), making it difficult to accurately reconstruct the effects of the ground plane. The boresight cross-pole discrimination is used in simulation as an approximation, but modeling the RCP/LCP mix received through each antenna is hindered by this azimuth variation and ambiguity.

4.4 Model of Mission Truth Geometry

United Space Alliance calculated the absolute position and attitude of the space shuttle as part of their Postflight Attitude And Trajectory History (PATH) product, a standard product for shuttle missions. This incorporated tracking data (both ground-

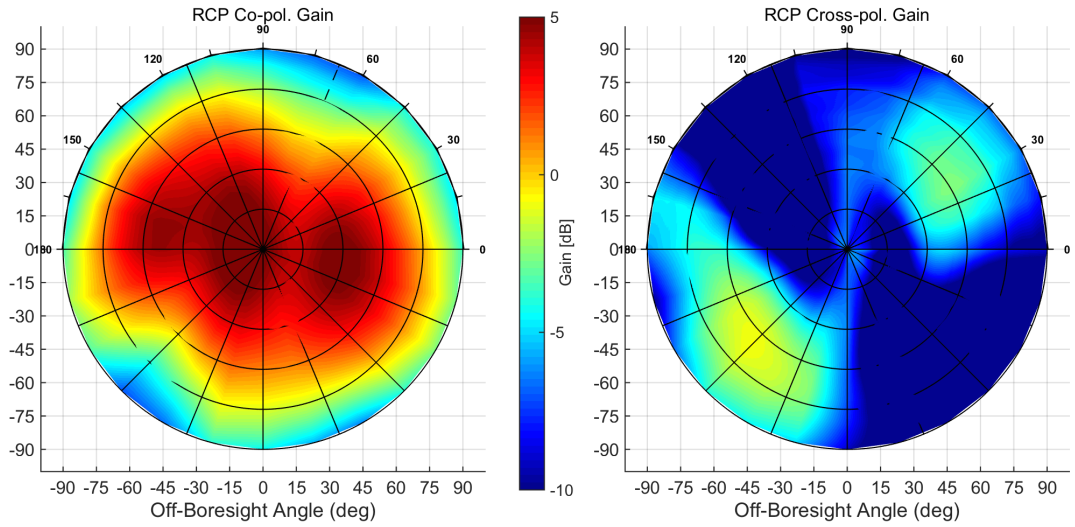

Fig. 4.5. Co-pole and cross-pole gain of RCP flight antenna

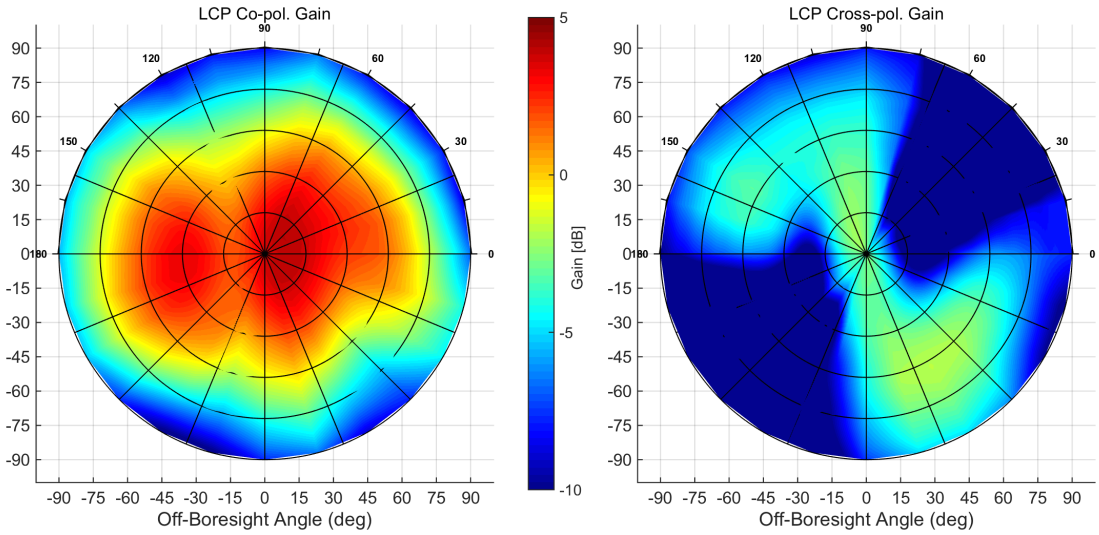

Fig. 4.6. Co-pole and cross-pole gain of LCP flight antenna

based C-band radar tracking and TDRS tracking), telemetry data, and data generated during real-time support in the Mission Control Center [52].

As an optional service, United Space Alliance also calculated the relative position and attitude of HST as part of the Relative Best Estimate Trajectory (RELBET) product. This primarily relied on the shuttle's on-board rendezvous radar for rela-

tive range information [53]. The rendezvous radar is part of a dual-purpose shuttle subsystem, the Ku-band radar/communication system, that can either communicate with the ground or act as a radar [54]. The functions are not available simultaneously, however, and during docking at 16:37:30 UTC, the radar was switched over to wideband communications [48]. Error increased in the RELBET estimate of HST position after the rendezvous radar was switched to communications, rendering the solution invalid.

Using images from the three RNS cameras, vision processing algorithms sought to track physical features of HST and estimate the space telescope's state relative to the shuttle. Noting discrepancies between their estimate and the RELBET estimate, researchers used RNS flight imagery to justify the HST position from RNS algorithms as the correct solution [48]. Therefore, the RELBET HST position is used for this work until the rendezvous radar is turned off at 16:37:30 UTC, then the position estimate from RNS image processing is used. The attitude truth is taken from RELBET throughout rendezvous. Spline interpolation was used to produce a composite HST trajectory from the RELBET and RNS data. This HST relative state was combined with the PATH ephemeris and attitude for the shuttle and GPS satellite positions from the International GNSS Service (IGS) to create a simulation of the mission geometry in STK. This is used as the reference truth geometry.

The range between the shuttle and composite HST trajectory is shown in Figure 4.7 for the RNS experiment time frame, overlaid on the range from each of the three data sources. A vertical dashed line indicates when the rendezvous radar was turned off. Note that scalar range alone does not fully describe the relative HST states of the three different data sources, or the transitions between them. See Appendix A for further details.

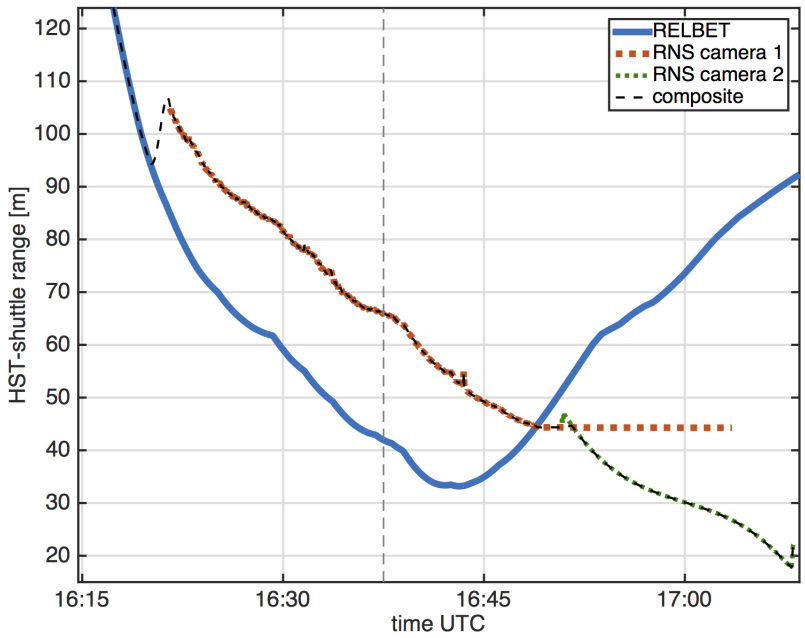

Fig. 4.7. HST-Shuttle range during rendezvous (May 13, 2009)

4.4.1 Accuracy

Qualitatively, the HST trajectory formed through the combination of these data sources produces a spacecraft geometry that closely agrees with the nominal mission profile [55]. The shuttle flies horizontally, parallel to the surface of the earth, as it approaches within 300 meters of HST (approximately 16:10 UTC). The shuttle's cargo bay is facing the space telescope, referred to as "target track attitude" [48]. As in the nominal approach [55], the shuttle flies below HST in preparation for the R-bar approach. Because HST is inertially fixed, it slowly rotates from its rendezvous attitude to the grapple attitude, where the HST aft bulkhead faces the shuttle cargo bay.

Due to a shuttle-HST S-band link failure, none of the planned HST maneuvers were performed. Instead, a 45° shuttle yaw maneuver was performed at 16:53 UTC when the inter-vehicle range was approximately 45 meters. At this point the space-

craft passed into orbital night and the shuttle began its R-bar approach. As the range to HST dropped below 40 meters, the shuttle was placed in an inertial hold, matching the space telescope rotation rate. All of these features of the shuttle and Hubble trajectories are accurately reproduced. Hubble was grappled with the Shuttle Remote Manipulator System at 17:13:56 UTC.

Quantifying the simulation accuracy is more difficult. The rendezvous radar used to determine RELBET position has a published 3σ bound of 25 meters downrange, 2 meters cross-track and 2 meters radial when the target spacecraft is less than 300 meters away [54] [52]. These bounds correspond to x, y and z in the shuttle body frame respectively. Attitude from RELBET has an accuracy of 0.2° when data from the Inertial Measurement Unit (IMU) is available and an accuracy of 0.75° when IMU data is not available and interpolation is used instead.

Due to errors in the RELBET solution after the rendezvous radar was powered off, no true HST trajectory was available for calculating the accuracy of the RNS algorithm's position estimates. Camera images were used to justify using the post-processed GNFIR solution as truth, and errors in RELBET, real-time GNFIR and ULTOR are stated relative to this trajectory. RNS researchers ultimately concluded, however, that their position estimation met the project's accuracy goals, reproduced here in Table 4.1. Although "lateral" and "range" refer to the x and z axes of the relevant RNS camera, these roughly correspond to the y and z axes of the shuttle structure frame respectively. These error bounds are consistent with a 1/10-th scale simulation conducted in the Flight Robotics Lab at Marshall Space Flight Center prior to the actual servicing mission [49].

Accuracy is even more uncertain for the absolute position of the shuttle (upon which the space telescope position is based). The PATH Interface Control Document states that "the 3σ ephemeris position accuracies may range from 0.5 to 5 km, while the 3σ ephemeris velocity accuracies may range from 0.5 to 5 m/sec" [52]. Typical flight values are shown in Table 4.2, but the PATH document notes that this is "excluding rendezvous periods." The lack of a reliable truth trajectory is a significant

challenge in analyzing and interpreting the HSM4 GPS data and hinders validation of an EM ray tracing model.

Table 4.1.
HST 3σ relative position accuracy (from [52] and [48])

	Target Range [m]	**Lateral Accuracy [m]**	**Range Accuracy [m]**
Rndz. Radar	< 300	2	2
RNS Cameras	150	1	3.3
	30	0.3	0.5
	5	0.1	0.1

Table 4.2.
Shuttle 3σ position and velocity accuracy (from [52])

	Radial	**Downtrack**	**Crosstrack**
position [m]	200	450	200
velocity [m/s]	0.45	0.20	0.25

5. MULTIPATH MODELING AND SIGNAL SIMULATION

5.1 EM Ray Tracing

In order to estimate environment features from multipath (such as the distance of a reflecting target spacecraft from a receiver), it is necessary to characterize the relationship between the environment features of interest and the observable multipath properties. In an effort to quantify this relationship, a simulation of signal reflections in HSM4 has been constructed using EM ray tracing software. Reflected signals are characterized by their amplitude attenuation, carrier phase shift and code phase shift relative to LOS signals, as described in Section 3.3. These properties can be related to the additional path length traveled by the reflected signal. This can, in turn, be related to the location of the reflecting surface.

The Advanced GNSS Multipath Model (AGMM) developed at the Colorado Center for Astrodynamics [56] is used to simulate the expected multipath during HSM4. AGMM integrates the commercially-available wave propagation software WinProp® (developed by AWE Communications [57]) into the following suite of modules [58]. The scenario was set up in collaboration with researchers at the University of Colorado, Jeanette Veldman and Penina Axelrad. They then performed the ray tracing runs [59]. The modules employed to produce the ray tracing results used in this dissertation are described below. Other modules of the AGMM, such as the antenna and tracking loop modules, were not used.

1. The receiver environment module is initialized with a CAD model describing the structures surrounding the receiving antenna. For the HSM4 simulation, a CAD model of HST provided by GSFC was imported into the software. The model was simplified to decrease ray tracing computation time. This simulation

neglects multipath generated in the shuttle bay. Structures were translated and rotated within WinProp to reproduce the time-variant relative geometry of HST and the shuttle while docking.

2. The transmitter motion module describes the relative trajectory of the GPS satellites with respect to the receiver on the shuttle. The satellite motion in WinProp is defined by azimuth, elevation, and range relative to the receiving antenna. For the HSM4 simulation, trajectories of visible GPS satellites during docking were defined using final solutions from the IGS. Combined with the trajectory of the shuttle discussed in Section 4.4, GPS satellite positions were converted into azimuth and elevation in the receive antenna frame.

3. The ray tracing module incorporates environment information from the first two modules and generates all possible signal paths between the transmitter and receiver. This module calculates all possible signal paths between the transmitter and receiver based on concepts from GO and UGTD [57]. WinProp logs the characteristics of each incoming ray path, including time of arrival, field strength, and number of interactions. Several interaction parameters are also logged, including coordinates, material properties, and object ID number.

A ten-minute ray tracing simulation was developed to replicate HSM4 geometries from 16:22 to 16:23 UTC on May 13, 2009. Continuous interactions were observed lasting up to three minutes. The ray tracing results for all PRNs are summarized in Figure 5.1, where each interaction is plotted in the antenna frame coordinates and colored according to the received field strength relative to the corresponding LOS signal. The combination of reflections reveals the outline of HST. The translation of HST due to the docking approach trajectory is evident (progressing from top to bottom of the figure), and the relative field strengths increase as the shuttle approaches. Some of the strongest reflections arise from the spacecraft's solar panels.

Additional summarizing features of the ray tracing results are shown in Figure 5.2. In 5.2(a), the number of PRNs with visible reflections is shown over the duration

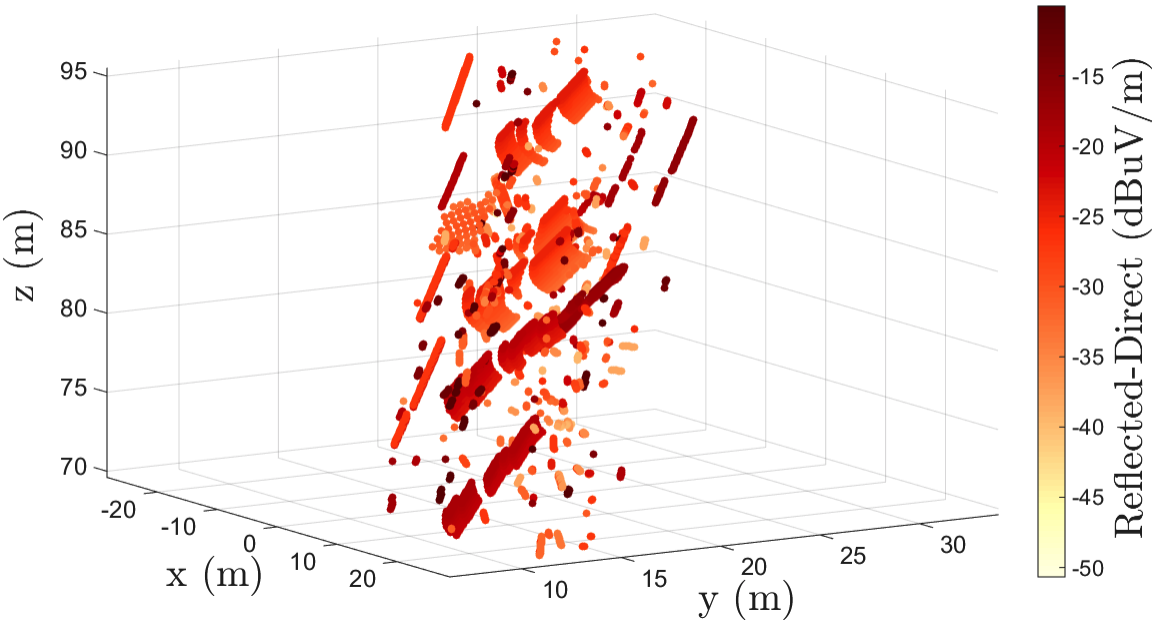

Fig. 5.1. Relative field strength of interactions generated by all PRNs between 16:22 and 16:32 UTC, plotted in receive antenna coordinates (figure produced by J. Veldman [59])

of the EM simulation. The variety of PRNs causing reflections is important, as the quality of a reflection for navigation depends on HST's scattering properties for a given incident angle. The navigation solution quality also depends on the geometric distribution of transmitters. Reflection duration is important if the reflections are to be measured. The relative delays of four PRNs with continuous reflections greater than a minute are shown in 5.2(b). Note that these are the relative delays of each PRN's strongest reflection; in actuality there are numerous simultaneous reflections for each.

5.2 Signal Simulation

The reflected ray properties produced by the EM ray tracing are used to generate simulated GPS data, where the geometric features causing multipath are precisely

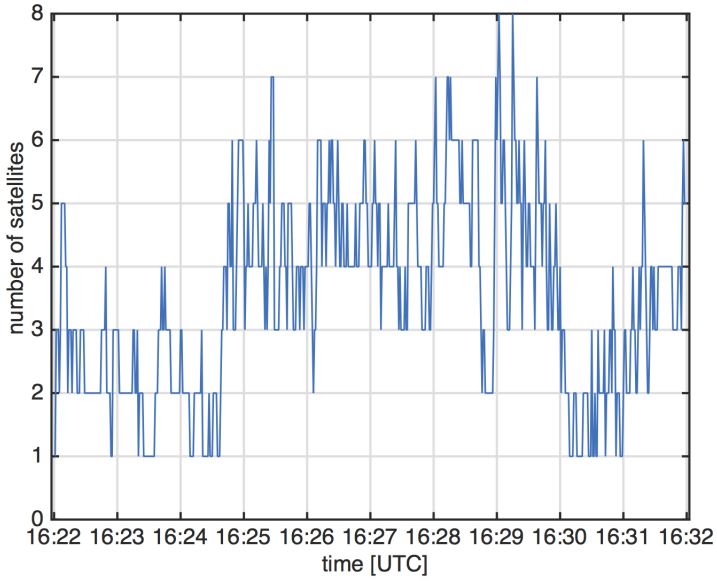

(a) Number of PRNs with visible reflections

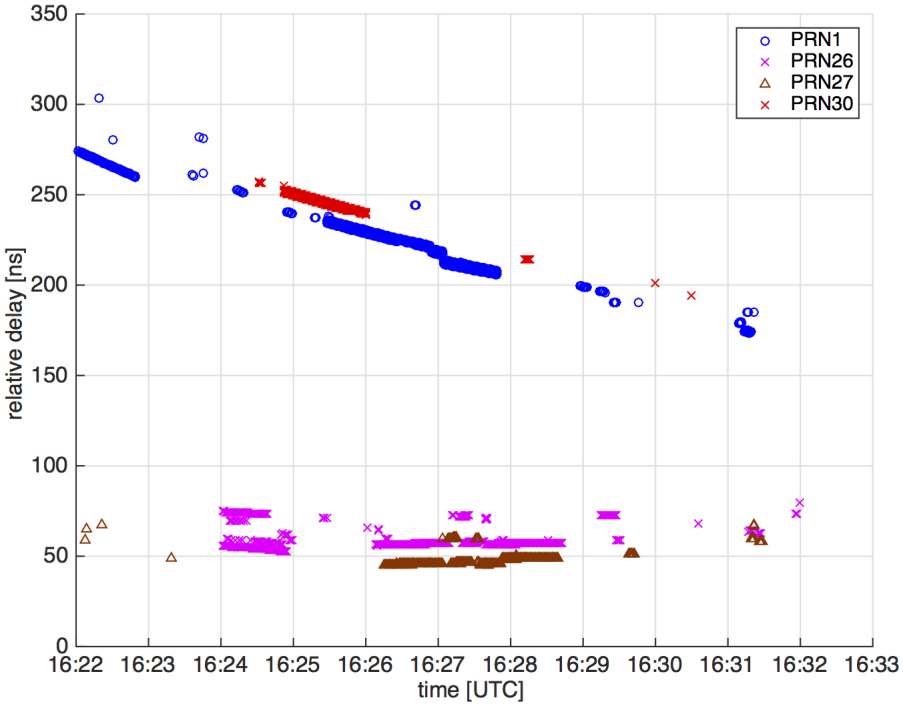

(b) Relative delay of strongest visible reflections for selected PRNs

Fig. 5.2. EM ray tracing results

known. Signal simulation code was initially created in MATLAB by GSFC engineers as a development tool, the GSFC Siggen ("Sig-gen"), then modified for this research to include multipath. The GPS constellation is simulated by propagating the satellite states described in a RINEX file for the appropriate epoch. The shuttle ephemeris from United Space Alliance's PATH product is used as the receiver trajectory. At each time step (a sampling interval), a clean, multipath-free signal is generated, where the i-th sample of the simulated signal for the n-th satellite is

$$s_0^n[i] = a_0^n[i] d_0^n[i] c_0^n[i] e^{\theta_0^n[i]}. \tag{5.1}$$

Here $d_0^n[i]$ is the navigation data bit and $c_0^n[i]$ the C/A code, each shifted according to the propagation delay due to the receiver-transmitter range, $r_0^n[i]$. A carrier-to-noise spectral density is calculated from a receiver-transmitter link budget and transformed into signal amplitude

$$a_0^n[i] = \sqrt{\frac{10^{C/N_0^n[i]/10}\sigma}{2f_s}}, \tag{5.2}$$

while carrier phase is determined from the geometric range, ionospheric delay and transmitter clock bias

$$\theta_0^n[i] = j(2\pi f_{IF} t[i] - 2\pi f_{L1}(r^n[i]/c - \tau_{iono}^n[i] + \tau_{b,s}^n[i])). \tag{5.3}$$

Multipath parameters $\alpha_m^n[i]$, $\delta_m^n[i]$ and $\psi_m^n[i]$ are obtained from the EM ray tracing simulation and used to calculate the m-th multipath signal

$$s_m^n[i] = a_m^n[i] d_m^n[i] c_m^n[i] e^{\theta_m^n[i]}, \tag{5.4}$$

where the navigation data bit and C/A code are shifted according to $r_m^n[i] = r_0^n[i] + \delta_m^n[i]$, and

$$a_m^n[i] = \alpha_m^n[i] * a_0^n[i], \tag{5.5}$$

$$\theta_m^n[i] = \theta_0^n[i] - \psi_m^n[i]. \tag{5.6}$$

The total simulated signal is formed by summing the direct signals for each of the N visible satellites, as well as any corresponding multipath signals,

$$s_{total}[i] = \sum_{n=1}^{N} \left(\sum_{m=0}^{M_n} s_m^n[i] \right) + \epsilon[i], \tag{5.7}$$

where $\epsilon[i]$ is a circular symmetric Gaussian random variable with variance σ^2.

5.3 Implementation

Four PRNs are used as examples in the following chapters, each selected for the presence of continuous reflections lasting several seconds: 1, 26, 27, and 30. Data simulation and tracking was performed from 16:25:27 to 16:28:12 UTC, a time span of 165 seconds (2.75 minutes). Some practical difficulties arise when using the ray tracing results to simulate signals, however. For example, the delay and power of reflections relative to the LOS signal for PRN 26 are shown in Figure 5.3. It is clear by inspection that a number of reflected rays are arriving simultaneously. This is a common feature of the ray tracing results. When generating simulated signals from these data, however, the individual rays are indistinguishable. It is not possible to associate one time-tagged delay value with a preceding delay value in order to reconstruct the time evolution of a single ray.

To resolve this, a curve fit is used to approximate the reflected ray represented by the data points. For instance, in Figure 5.3 a ray with a slope of 0.0145 ns/s starting at a delay of 56.48 ns would well approximate the reflected signal from 16:26:10 to 16:27:09 UTC. An average of the relative power is used. This approach is followed for each of the PRNs, producing the delay profiles described in Table 5.1. This approximation is justified by considering that the plurality of nearly identical, simultaneous reflections is likely due to the necessary discretization in the ray tracing simulation of shapes, such as the curved body of HST, into polygons. The effect can be seen in the ray tracing simulation itself, shown for a single time instant in Figure 5.4.

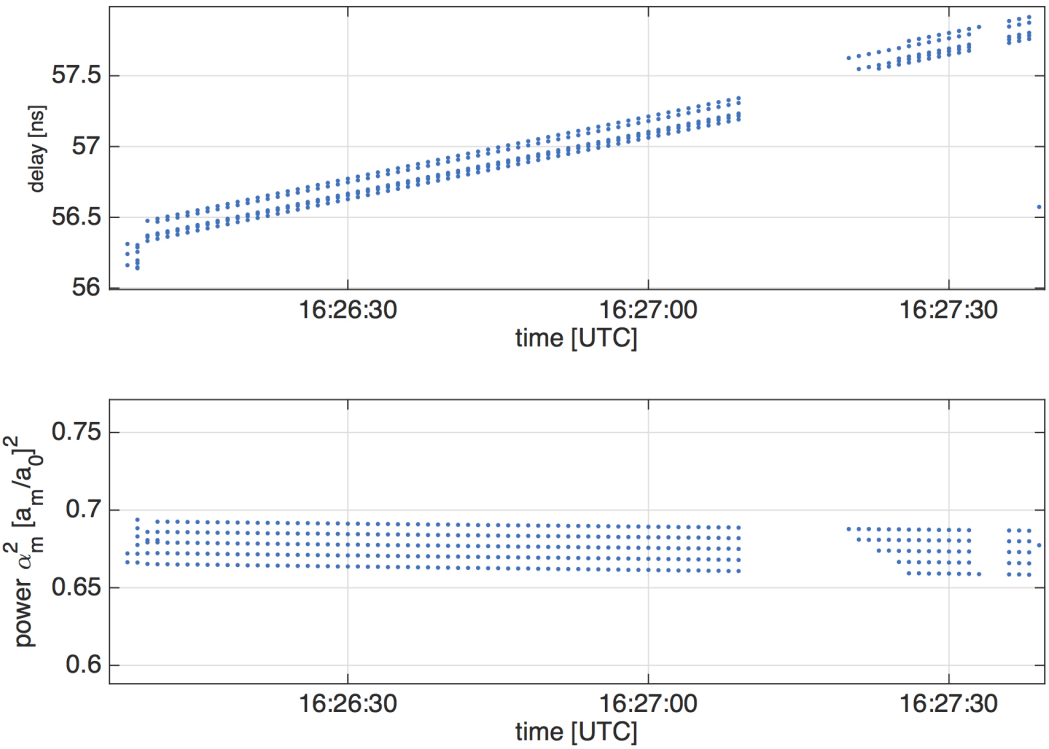

Fig. 5.3. Relative delay (top) and power (bottom) of reflected rays from PRN 26 ray tracing

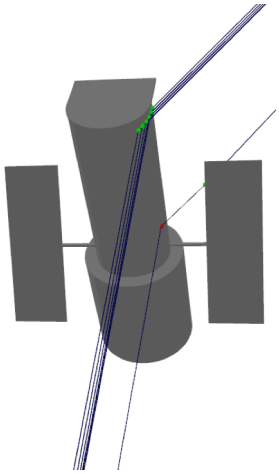

Fig. 5.4. PRN 26 ray tracing at 16:25 UTC (figure produced by J. Veldman)

Table 5.1.
Simulated multipath parameters from ray tracing starting at 16:25:27 UTC

PRN	δ_0 **[m]**	$\dot{\delta}$ **[cm/s]**	α_m^2/α_0^2
1	70.80	-4.94	0.45
26	16.75	0.44	0.66
27	16.32	0.47	0.67
30	73.84	-5.73	0.38

6. MODEL VALIDATION

The simulated and experimental data sets discussed in the preceding chapters are processed with the RNS SDR and other software receivers. Signal tracking measurements made by these receivers constitute the observables upon which this analysis is based. These measurements fall into two categories: those that provide range information, discussed in Chapter 8, and those that do not, discussed in this chapter. Although not useful for ranging, these measurements are nevertheless useful for model validation. In order to confirm that the EM ray tracing and simulated signals accurately model the relationship between geometry, reflected rays, and tracking observables, it is important to find measurements of multipath that can be made from both the simulated and experimental data. Oscillation of the prompt correlator power due to the presence of multipath, known as fading, was measured in both the simulated and experimental tracking outputs. Multipath-induced code tracking error was measured through simulated data tracking and used to verify model consistency - the presence of Hubble-reflected rays led to the expected signal tracking effects.

6.1 Multipath Fading

As the excess path length traveled by a reflected signal changes, the relative carrier phase will cycle through phases that add to the LOS signal constructively and destructively, an effect known as fading. This results in a characteristic oscillation of received power, the frequency of which is determined by the rate of change of the excess path length:

$$\dot{\psi} = (1/\lambda_{L1})\dot{\delta}. \tag{6.1}$$

The dot indicates a time derivative. In stationary terrestrial receivers, this oscillation frequency is known to be a function of satellite elevation. Ground reflections will cause

a higher frequency oscillation from low elevation satellites, as the excess path length of the reflections is changing more rapidly than for satellites at higher elevations [60]. In spacecraft docking, the oscillation frequency is driven by the relative geometry of the transmitting GNSS satellite, target, and receiver.

6.1.1 Simulation

Figures 6.1 and 6.2 show the prompt correlator power in the time and frequency domains (left and right plots, respectively). The expected oscillation from the simulated geometry (i.e., $\dot{\delta}$ in Table 5.1) and Equation (6.1) is 0.2595 Hz for PRN 1 and 0.3012 Hz for PRN 30. The peak measured oscillation, determined through the first peak in the frequency domain, is 0.2594 Hz for PRN 1 and 0.3052 Hz for PRN 1. Due to the simulated signal length (165 seconds), the resolution of the FFT is 0.0061 Hz; both measured fading frequencies are accurate to within the FFT resolution.

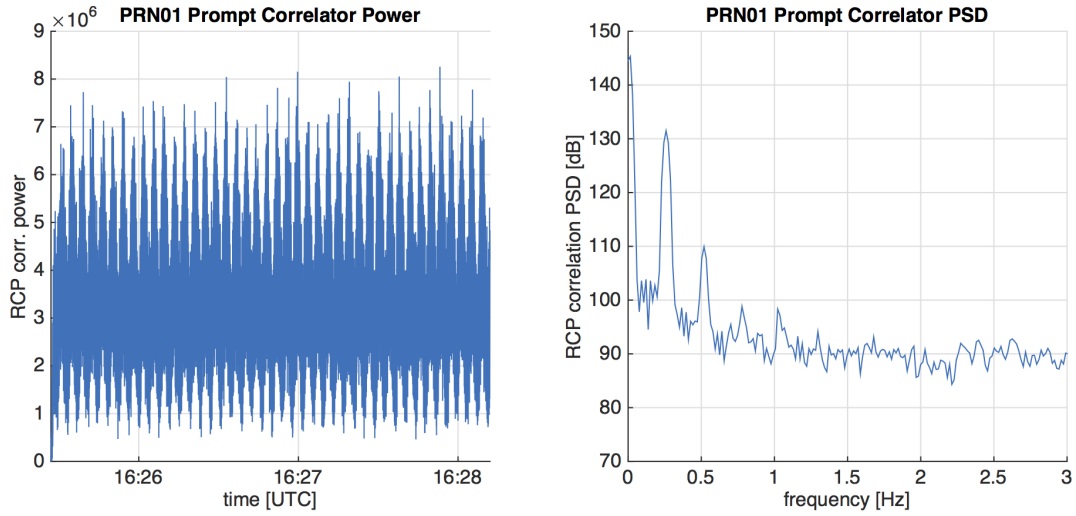

Fig. 6.1. Simulation: PRN 1 prompt power oscillation

PRNs 26 and 27 are an order of magnitude slower. The frequency of each is difficult to identify in the frequency domain but easily confirmed in the time domain. Figure 6.3 shows PRN 26, for example, where the calculated frequency is 0.0230 Hz.

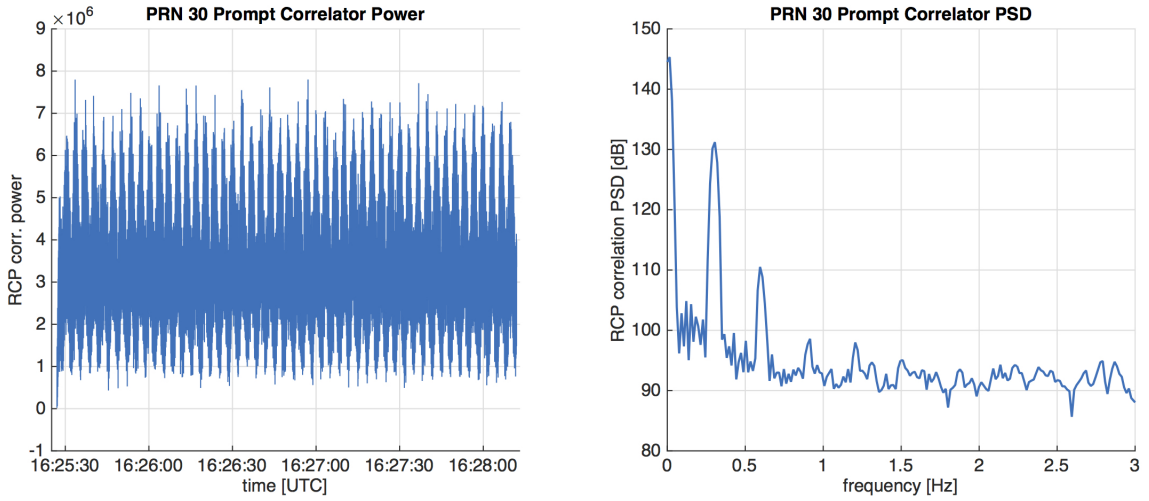

Fig. 6.2. Simulation: PRN 30 prompt power oscillation

This corresponds to a period of 43.55 seconds - approximately 3.8 periods over the simulation duration. The measured fading features in Figure 6.3 agree with these values. In the frequency domain on the right, a secondary peak may be present in the spectrum of the filtered power measurement at 0.0244 Hz, but the relatively coarse resolution of the FFT makes this difficult to discern.

6.1.2 Experiment

Multipath-induced oscillation of the prompt correlator power can also be measured in the experimental data. The measured frequency of oscillation is generally consistent with the rate of change of the reflected signal's relative delay in Table 5.1. This effect was first observed by University of Colorado collaborators [61].

The prompt correlator power for PRN 1 is shown in Figure 6.4. On the top left is the RCP time domain, where a coherent integration time of 1 ms is used. A 20 ms non-coherent average is overlaid in orange. The spectra of these unfiltered and filtered RCP power measurements are shown on the top right. The measured frequency of

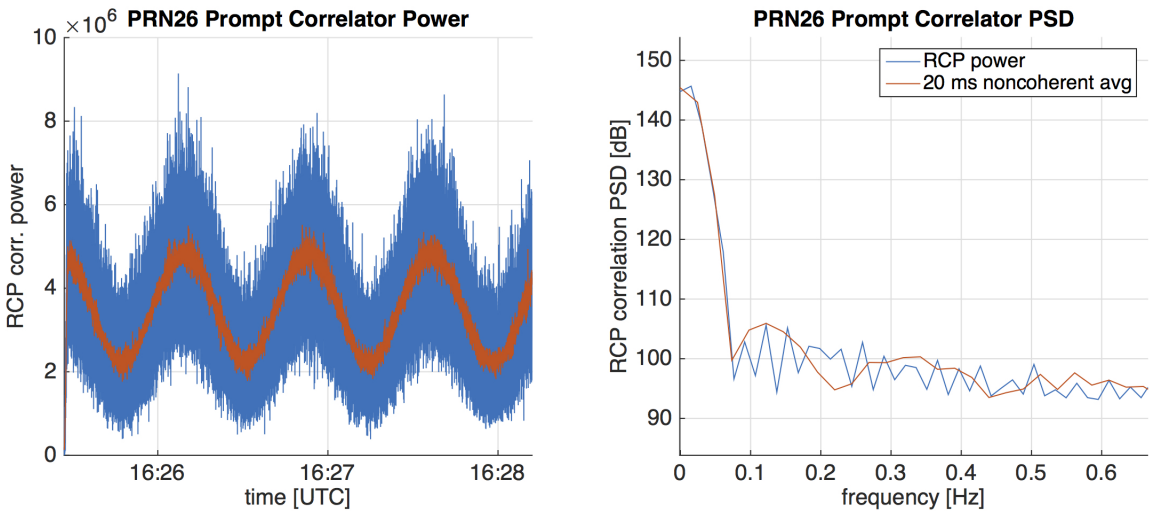

Fig. 6.3. Simulation: PRN 26 prompt power oscillation

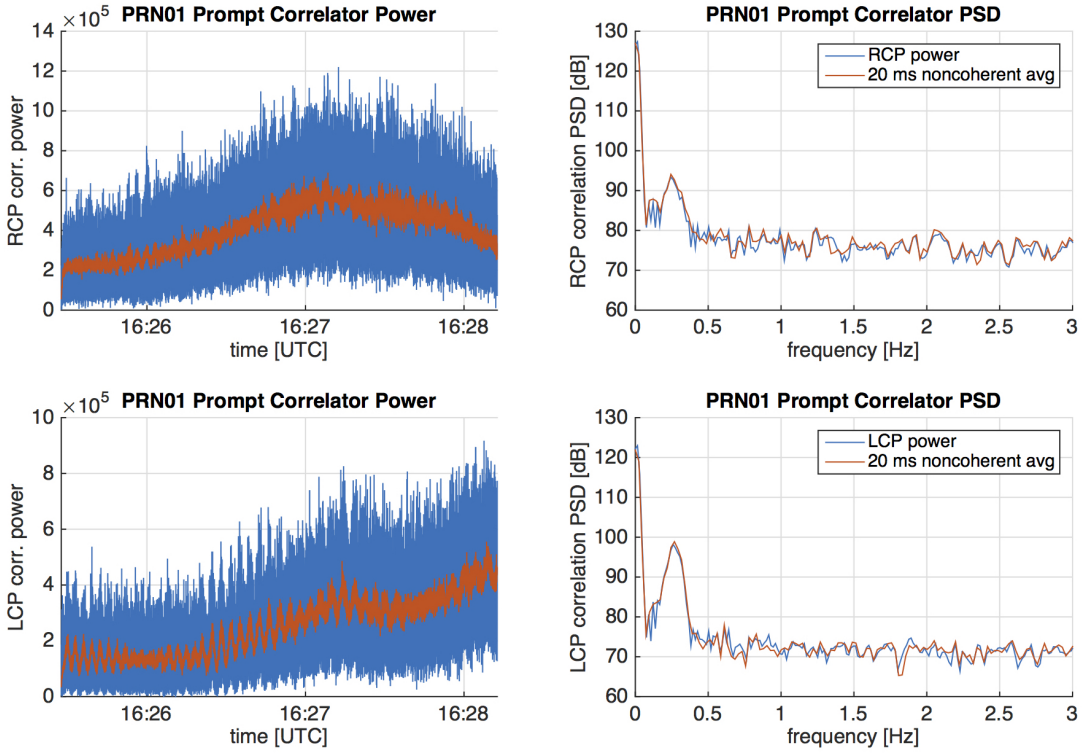

Fig. 6.4. Experiment: PRN 1 prompt power oscillation

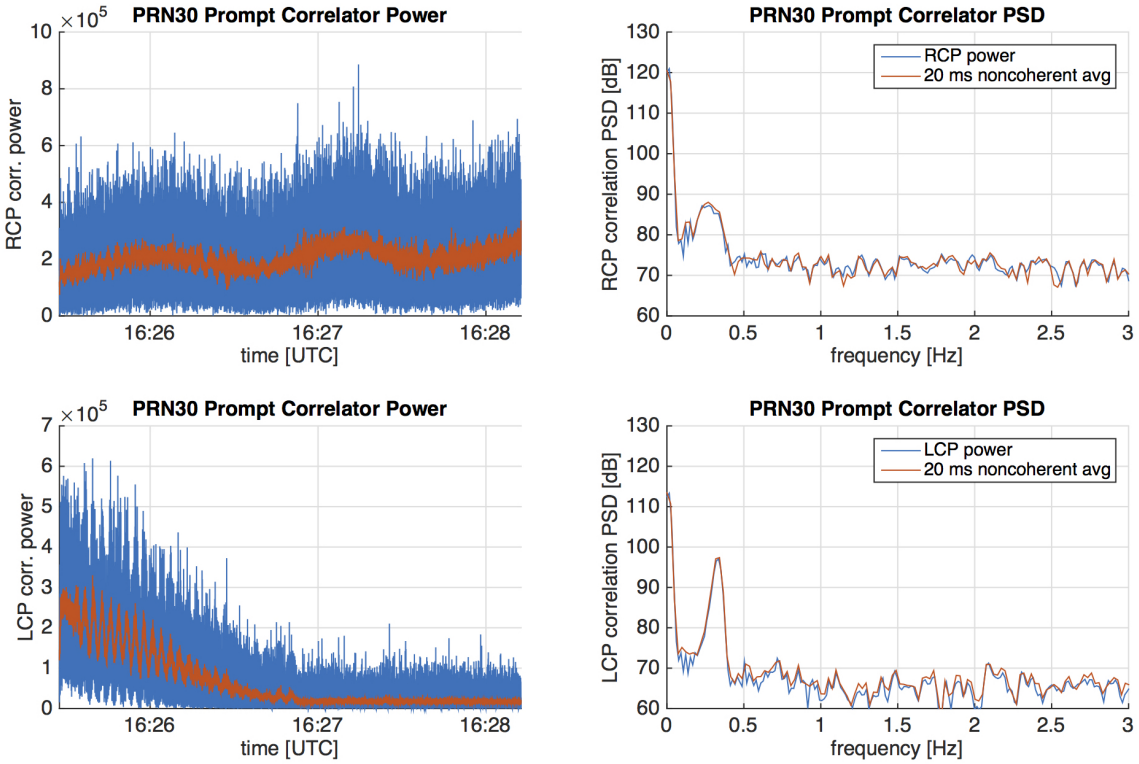

Fig. 6.5. Experiment: PRN 30 prompt power oscillation

the unfiltered LCP power is 0.2595 Hz - within the FFT resolution of the expected $\dot{\psi} = 0.2596$ Hz. Frequencies in the filtered RCP and LCP data do not agree quite as closely (0.2441 Hz and 0.2686 Hz respectively). However, the similarity between the results of tracking the simulated and experimental data suggest that the ray specified in Table 5.1 for PRN 1 is accurate. PRN 30 exhibits close agreement with ray tracing results as well, shown in Figure 6.5, with a measured $\dot{\psi} = 0.2686$ Hz (from the filtered RCP peak) and calculated $\dot{\psi} = 0.30118$ Hz.

The conclusion that this oscillation is due to multipath is further supported by the LCP tracking results, shown below the RCP results in both figures. The depth of the oscillation is greater, resulting in a larger frequency domain peak. While the frequency of multipath fading is determined by the rate of change of the multipath delay, the magnitude is a consequence of multipath strength. In the LCP data, reflected signals are expected to be stronger.

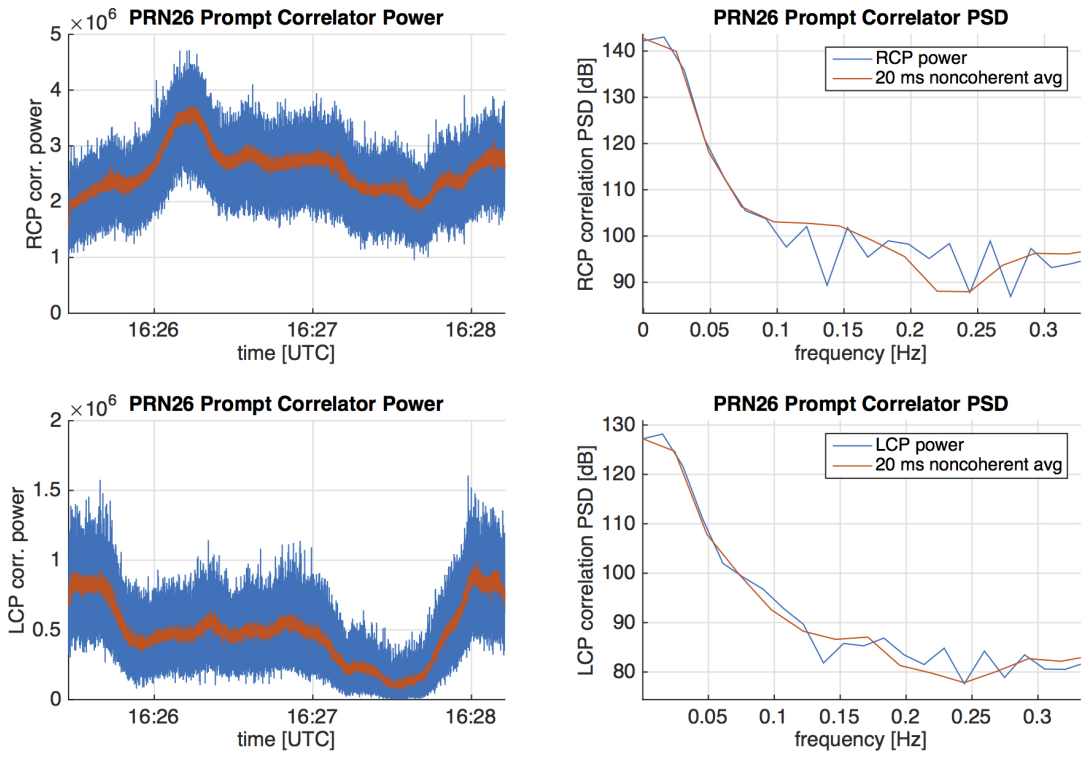

Fig. 6.6. Experiment: PRN 26 prompt power oscillation

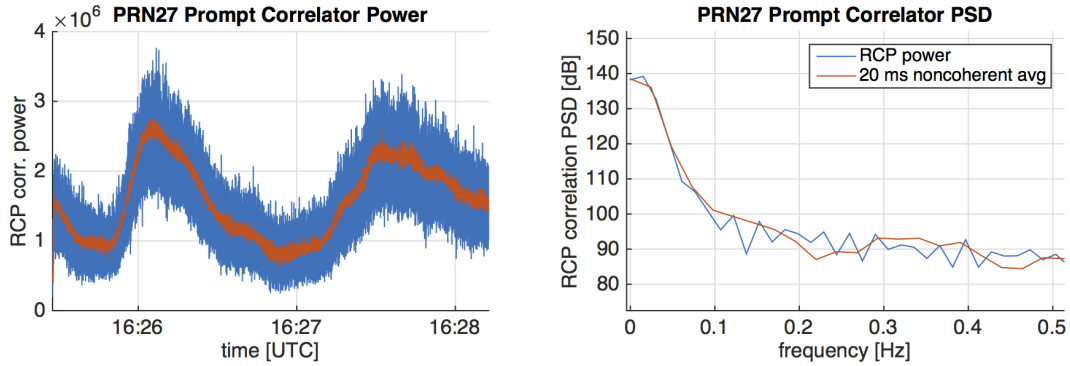

Fig. 6.7. Experiment: PRN 27 prompt power oscillation

The slower oscillations of PRNs 26 and 27 are more difficult to detect. A peak of 0.0244 Hz was measured in the filtered RCP spectra of both PRN 26 and 27, shown in Figures 6.6 and Figures 6.7 respectively. LCP tracking fails for PRN 27 and is not shown. While this $\dot{\psi}$ is within the FFT resolution of the calculated frequency for

both (0.0230 Hz for PRN 27 and 0.0244 Hz for PRN 26), the peak is not pronounced and the coarseness of the FFT leaves some doubt as to whether this measurement is physically meaningful. The time domain results are inconclusive.

Although the multipath offset rate of change is simulated as constant, this is not the case in reality. Unmodeled variation in the power oscillation frequency over time causes the wider frequency peak observed in PRNs 1 and 30, as compared to the simulated cases, and contributes to the difficulty in measuring $\dot{\psi}$ experimentally for PRNs 26 and 27.

6.2 Code Tracking Error

When the delay of a reflected signal is within one chip of the LOS (approximately 293 m), the reflected signal will distort the shape of the main lobe of the code correlation (see Figure 8.7). Furthermore, when the reflected signal is within the early/late correlator spacing, the multipath will affect the operation of code tracking, introducing errors.

A noncoherent DLL calculates the error in the current delay estimate $\hat{\tau}$ by forming the discriminator

$$S(\hat{\tau}) = \left|aR(\hat{\tau} - \tau + \frac{d}{2}T_C)e^{j\theta}\right|^2 - \left|aR(\hat{\tau} - \tau - \frac{d}{2}T_C)e^{j\theta}\right|^2, \tag{6.2}$$

where a is the signal amplitude, θ the carrier phase, d the offset of the two correlations (in chips) and T_C the chip period. When tracking is locked (i.e., error in the DLL code phase estimate is less than $dT_C/2$) the discriminator output is linearly proportional to the estimate error and is used to adjust the propagation delay estimate.

When multipath is present, however, correlations between the reflected signals and the early and late local codes distort the response of the DLL discriminator. Following the discussion in van Nee's dissertation on MEDLL [36], the discriminator curve in the presence of M multipath signals is,

$$S(\hat{\tau}_0) = \left|\sum_{m=0}^{M} a_m R(\hat{\tau}_0 - \tau_m + \frac{d}{2}T_C)e^{j\theta_m}\right|^2 - \left|\sum_{i=0}^{M} a_m R(\hat{\tau}_0 - \tau_m - \frac{d}{2}T_C)e^{j\theta_m}\right|^2 \tag{6.3}$$

where the zero subscript corresponds to the LOS signal. For DLL code phase error $\tau_e = \hat{\tau} - \tau$, the multipath-free case described by Equation (6.2) yields 0 when $\tau_e = 0$. However, Equation (6.3) yields 0 when $\tau_e = \tau_M$. Thus the discriminator drives the propagation delay estimate to $\tau_0 + \tau_M$ rather than τ_0.

In order to obtain a more convenient form for determining τ_M, let $\tau_d = dT_C/2$, $\alpha_m = a_m/a_0$, $\delta_m = \tau_m - \tau_0$, and $\psi_m = \theta_0 - \theta_m$, so that τ_d represents the correlator offset in seconds, and α_m, δ_m and ψ_m represent the relative amplitude, delay and phase of the i-th multipath signal respectively. Dividing Equation (6.3) by a_0^2 and writing as a function of error,

$$S_e(\tau_e) = \left| R(\tau_e + \tau_d) + \sum_{i=1}^{M} \alpha_m R(\tau_e + \tau_d - \delta_m) e^{-j\psi_m} \right|^2 - \left| R(\tau_e - \tau_d) + \sum_{i=1}^{M} \alpha_m R(\tau_e - \tau_d - \delta_m) e^{-j\psi_m} \right|^2. \quad (6.4)$$

The error in the propagation delay measurement caused by multipath rays with parameters α, δ and ψ can then be calculated by finding $\tau^\star$ such that $S_e(\tau^\star) = 0$.

To provide further insight, consider the case of a single multipath ray ($M = 1$):

$$S_e(\tau_e) = \left| R(\tau_e + \tau_d) + \alpha R(\tau_e + \tau_d - \delta) e^{-j\psi} \right|^2 - \left| R(\tau_e - \tau_d) + \alpha R(\tau_e - \tau_d - \delta) e^{-j\psi} \right|^2. \quad (6.5)$$

In this case the problem can be summarized as solving

$$0 = \left| R(\tau^\star + \tau_d) + \alpha R(\tau^\star + \tau_d - \delta) e^{-j\psi} \right|^2 - \left| R(\tau^\star - \tau_d) + \alpha R(\tau^\star - \tau_d - \delta) e^{-j\psi} \right|^2 \quad (6.6)$$

for $\tau^\star$. Without multipath, $\tau^\star = 0$, but with multipath this is some offset, $\tau^\star = \tau_M$.

Figure 6.8 shows the numerically computed multipath code tracking error, τ_M, as a function of δ, parameterized by ψ, where $\alpha = 1/2$. The solid lines show the maximum error cases, when $\psi = 0$ (top) or $\psi = \pi$ (bottom). The dashed lines show cases of ψ between these extremes. This fails to tell the whole story, however, as

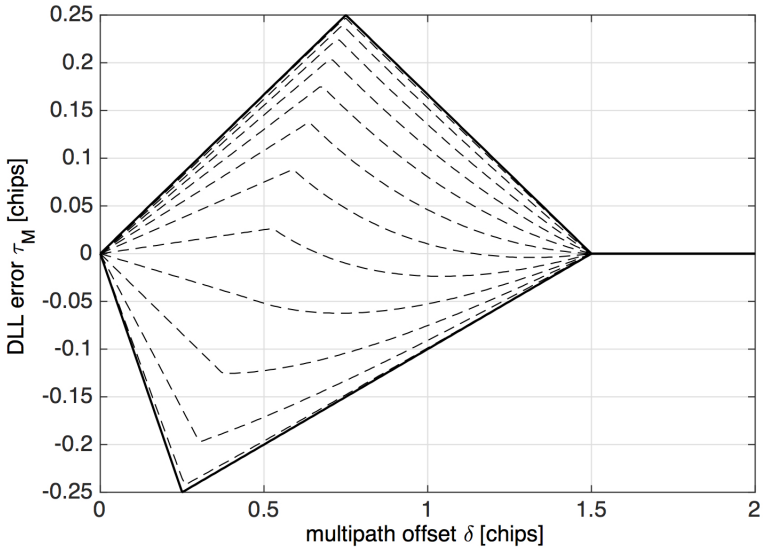

Fig. 6.8. Code tracking error in a noncoherent DLL due to one multipath signal (d = 1 chip, $\alpha = 1/2$)

ψ is functionally dependent on δ: $\psi_m = \text{mod}(\theta_0 - 2\pi\delta_m/\lambda_{L1}, 2\pi)$, where $\text{mod}(\cdot, 2\pi)$ indicates modulo 2π. Figure 6.9 shows a plot of τ_M for a single multipath signal over the space of relative amplitude and delay, demonstrating the importance of carrier offset in the code tracking error; τ_M varies significantly for even adjacent values of δ. This underscores an important point: the range of a reflecting target is not linearly related to the magnitude of the DLL tracking error, i.e., a larger code delay δ does not directly translate into a larger τ_M. Figures 6.8 and 6.9 show that τ_M does not map to unique δ values and therefore cannot be used as a measurement of the additional path length traveled by a reflected signal.

It is useful to have a closed form expression for the multipath-induced code error for code offsets of interest (i.e., small relative code delays that are measurable when tracking is locked). Consider again the case of one multipath ray, and set Equation

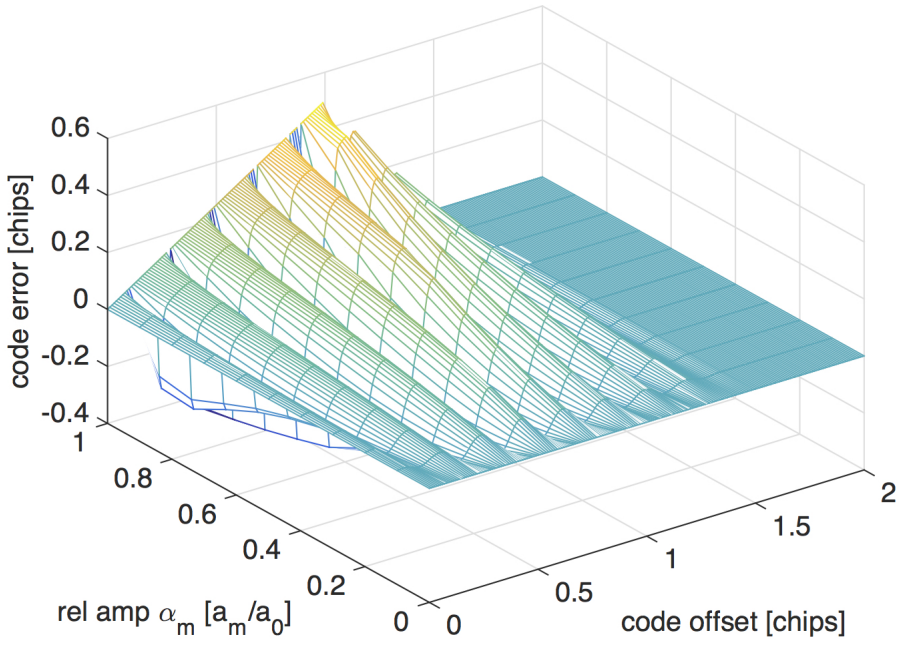

Fig. 6.9. Code tracking error over α and δ

(6.5) equal to zero and substitute the ideal code correlation function in Equation (2.4) for $R(\cdot)$. Assuming $\tau_e + \tau_d < T_C$ (i.e., the code correlation functions are nonzero),

$$0 = \left| \left(1 - \frac{|\tau_e + \tau_d|}{T_C}\right) + \alpha \left(1 - \frac{|\tau_e + \tau_d - \delta|}{T_C}\right) e^{-j\psi} \right|^2 - \left| \left(1 - \frac{|\tau_e - \tau_d|}{T_C}\right) + \alpha \left(1 - \frac{|\tau_e - \tau_d - \delta|}{T_C}\right) e^{-j\psi} \right|^2.$$

For cases when tracking is locked, $\tau_e < \tau_d$, so

$$0 = \left| 1 - \frac{\tau_e + \tau_d}{T_C} + \alpha \left(1 - \frac{|\tau_e + \tau_d - \delta|}{T_C}\right) e^{-j\psi} \right|^2 - \left| 1 - \frac{\tau_d - \tau_e}{T_C} + \alpha \left(1 - \frac{|\tau_e - \tau_d - \delta|}{T_C}\right) e^{-j\psi} \right|^2.$$

As demonstrated by the numerical solution in Figure 6.8, the code tracking error can be divided into δ regions. Consider the first region, where $\delta < \tau_e + \tau_d$:

$$0 = \left|1 - \frac{\tau_e + \tau_d}{T_C} + \alpha\left(1 - \frac{\tau_e + \tau_d - \delta}{T_C}\right)e^{-j\psi}\right|^2 - \left|1 - \frac{\tau_d - \tau_e}{T_C} + \alpha\left(1 - \frac{\tau_d + \delta - \tau_e}{T_C}\right)e^{-j\psi}\right|^2.$$

Expanding and multiplying both sides by T_C,

$$0 = \left(\frac{4\tau_d}{T_C} - 4 - 4\alpha^2 + \frac{4\alpha^2\tau_d}{T_C} - 8\alpha\cos\psi + \frac{8\alpha\tau_d\cos\psi}{T_C}\right)\tau_e + 4\alpha^2\delta - \frac{4\alpha^2\tau_d\delta}{T_C} + 4\alpha\delta\cos\psi - \frac{4\alpha\tau_d\delta\cos\psi}{T_C}.$$

After substituting $\tau_d = T_C d/2$ and some algebra, the solution for τ_e is

$$\tau_e = \frac{\alpha^2\delta(d-2) + \alpha\delta\cos\psi(d-2)}{(d-2)(1+\alpha^2) + 2\alpha\cos\psi(d-2)}.$$

This yields a closed-form expression for the DLL discriminator error in terms of multipath parameters,

$$\tau_M = \frac{\alpha^2\delta + \alpha\delta\cos\psi}{1 + \alpha^2 + 2\alpha\cos\psi}, \tag{6.7}$$

when the code delay offset is less than the sum of the resulting error and early-late spacing.

Note that the relative amplitude of the received signals is a factor of not only the relative power incident on the antenna, α, but also the relative gain of the antenna in response to the signal's polarization. In the case of an RCP antenna, which has been assumed so far in this section, the primary polarization (or "co-polarization") is optimally tuned to receive direct signals. LCP signals will be received through the antenna's cross-polarization gain. The relative amplitude of multipath is therefore scaled by the ratio of these two gains, $G_{R\times}/G_R$, where $G_{R\times}$ is the cross-polarization gain of the RCP antenna, and G_R the co-polarization gain. This results in a multipath-induced code tracking error of

$$\tau_{M,RCP} = \frac{\left(\alpha\frac{G_{R\times}}{G_R}\right)^2\delta + \alpha\frac{G_{R\times}}{G_R}\delta\cos\psi}{1 + \left(\alpha\frac{G_{R\times}}{G_R}\right)^2 + 2\alpha\frac{G_{R\times}}{G_R}\cos\psi}. \tag{6.8}$$

The tracking error due to multipath that arises when tracking LCP data is analogous, but depends on whether the reflected signal or LOS signal is treated as the interferer. When a LOS signal is tracked, the co-polarization of the LCP antenna is applied to the reflected signal causing the error:

$$\tau_{M,LCP} = \frac{\left(\alpha\frac{G_L}{G_{L\times}}\right)^2\delta + \alpha\frac{G_L}{G_{L\times}}\delta\cos\psi}{1+\left(\alpha\frac{G_L}{G_{L\times}}\right)^2 + 2\alpha\frac{G_L}{G_{L\times}}\cos\psi}. \tag{6.9}$$

This is the situation that appears to arise in Figures 6.4 and 6.5. If a reflected signal is being tracked, however, the LOS signal causes fading and

$$\tau_{M,LCP} = \frac{\left(\alpha\frac{G_{L\times}}{G_L}\right)^2\delta + \alpha\frac{G_{L\times}}{G_L}\delta\cos\psi}{1+\left(\alpha\frac{G_{L\times}}{G_L}\right)^2 + 2\alpha\frac{G_{L\times}}{G_L}\cos\psi}. \tag{6.10}$$

These two cases are discussed further in Chapter 8.

Although multipath-induced code tracking error does not translate into inter-vehicle range, it is useful as a means for detecting multipath. Features of the measured error can be used to assess the consistency of the EM ray tracing and signal simulation.

6.2.1 Simulation

If the true pseudorange is known, code tracking error can be measured through pseudorange error. The impact of M reflected signals on the pseudorange measurement can be summarized by adding an additional delay term to the multipath-free propagation delay in Equation (2.37),

$$c\tau^i = (r^i + I^i_{L1} + T^i) + c\tau^i_M, \tag{6.11}$$

so that the measured pseudorange from the i-th satellite is

$$\rho^i = r^i + ct_{b,R} - ct^i_{b,s} + I^i_{L1} + T^i + c\tau^i_M + v^i. \tag{6.12}$$

The multipath-induced tracking error can then be measured by subtracting the true pseudorange from this measured pseudorange,

$$\tau^i_M = \rho^i - \rho^i_{true}, \tag{6.13}$$

where the true pseudorange is constructed from known or estimated quantities according to Equation (2.38). This requires knowledge of the multipath-free pseudorange to an accuracy less than the magnitude of τ_M^i.

In the simulation case the geometric range, clock biases, and atmospheric delays are known, so a multipath-free pseudorange can be formed and multipath-induced tracking error can be calculated according to Equation (6.13). The measured, multipath-corrupted pseudorange is written ρ^i and is defined in Equation (6.12). A simple case is shown in Figure 6.10 in which PRN A and PRN C each contain one reflected signal with a constant $c\delta$ of 74.2 m and 55.6 m respectively [59]. Once tracking is locked, the excess pseudorange converges to the theoretical multipath-induced code tracking error given by Equation (6.7) and plotted by the corresponding dashed lines. PRN B has no multipath and predictably converges to zero.

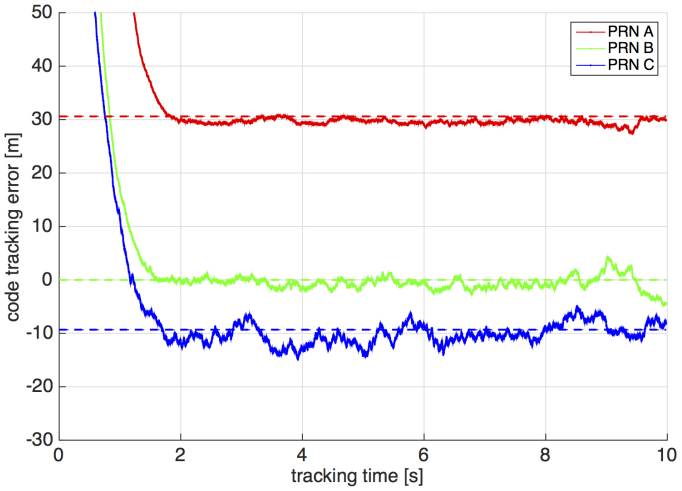

Fig. 6.10. Measurement of multipath-induced tracking error in the case of constant δ

In the case of multipath that changes relative to the LOS signal, τ_M is dominated by oscillations due to the relative carrier phase. The theoretical and measured tracking error is shown in Figures 6.11 and 6.12 for PRNs 1 and 26 respectively. There are several important differences between the realistic results and the constant mul-

tipath case. The dynamic code offset cases are characterized by carrier phase-driven oscillation and very little bias - all four simulated PRNs have a mean of nearly zero once tracking is locked. The apparent multipath-induced bias in Figure 6.10 is the result of a fixed relative carrier phase. The depth of the oscillation, i.e., the maximum and minimum code error values, is driven by the relative amplitude of the reflected signal. As seen in Figure 6.9, this can be as great as 0.5 chips (approximately 145 m). However, unlike the signals simulated in the constant multipath case, the realistic multipath has been attenuated according to the cross-polarization gain of the HSM4 RCP antenna. Code error in these cases does not exceed twenty meters.

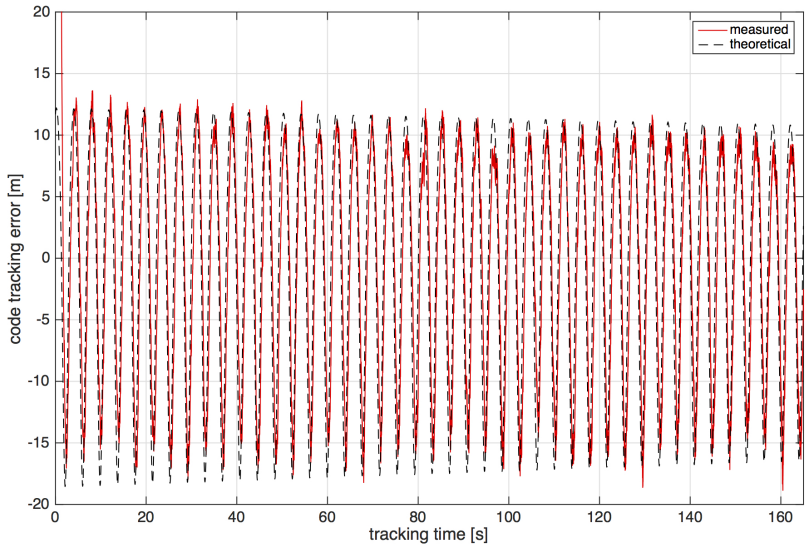

Fig. 6.11. Simulation: measurement of PRN 1 multipath-induced tracking error 16:25:27 to 16:28:12 UTC

For each of the example PRNs the pseudorange error measured by tracking simulated data agrees with the error calculated from the multipath parameters via Equation (6.7), plotted as black, dashed lines in Figures 6.11 and 6.12. This demonstrates the consistency of the multipath model: the simulated reflected rays are manifested in tracking observables as expected. Discrepancies between the theoretical and measured code error are due to unmodeled features of the tracking loop.

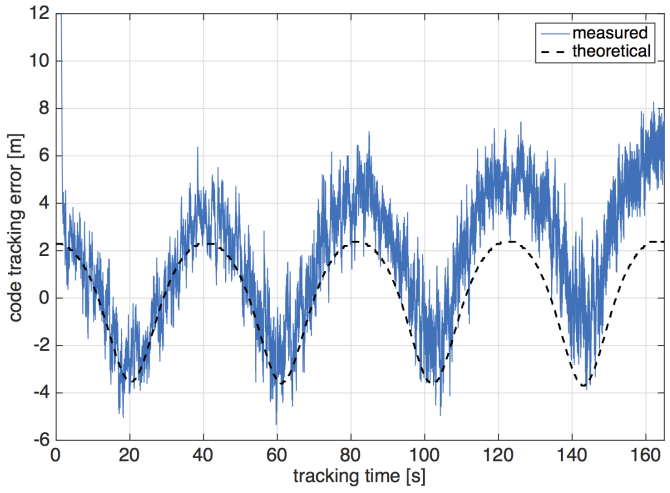

Fig. 6.12. Simulation: measurement of PRN 26 multipath-induced tracking error 16:25:27 to 16:28:12 UTC

6.2.2 Experiment

During HSM4 rendezvous, the direct/reflected signal path length difference ranged from approximately 235 meters down to 20 meters, or 0.8 to 0.07 chips. As in the simulation case, Hubble-reflected signals should result in perceptible code tracking errors. The difficulty in the experimental case is reconstructing a true pseudorange. Clock bias terms and atmospheric delays must be estimated with a combined error ϵ, where $\epsilon << c\tau_M^i < T_{C/A}$. A true pseudorange was constructed using the geometric range from the truth geometry and satellite clock biases from the IGS. The receiver clock bias was estimated by the NavSDR, and the ionospheric delay estimated using the International Reference Ionosphere 2012 (IRI-2012), developed by the Committee on Space Research and International Union of Radio Science. Unfortunately the results were inconclusive. The difference between the constructed "true" pseudorange and the measured pseudorange is shown in Figure 6.13 for PRNs 26 and 30. The erroneous bias and drift common to both measurements suggests the clock bias has not been correctly removed.

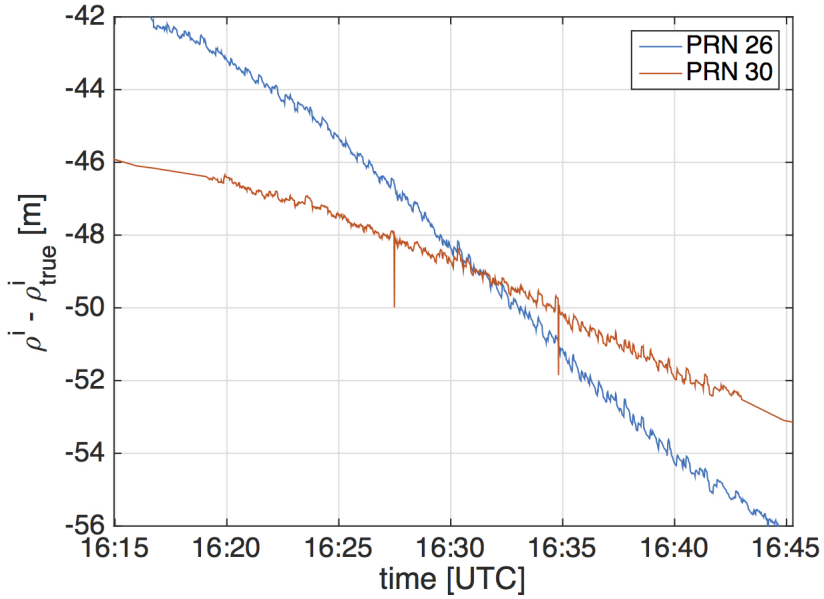

Fig. 6.13. Experiment: $\rho^i - \rho^i_{true}$

In order to eliminate clock bias, an attempt was also made to determine a relative multipath error by differencing pseudoranges from two satellites:

$$\rho^i - \rho^j = (r^i - r^j) - c(t^i_{b,s} - t^j_{b,s}) + c(\tau^i_{atm} - \tau^j_{atm}) + c(\tau^i_M - \tau^j_M). \tag{6.14}$$

Here τ^i_{atm} and τ^j_{atm} are the combined delay due to the ionosphere and troposphere for each satellite. Receiver clock biases, common to both measurements, cancel. For satellites at similar elevations, the difference between the atmospheric delays may be negligible and the relative multipath error experienced by each channel can be compared if the geometric ranges and satellite clock biases are known with sufficient accuracy. This too was inconclusive, however, as the difference between two satellite pseudorange measurements was on the order of hundreds of meters. Ultimately it is concluded that measurement of code tracking error in the simulation case is hindered by poor knowledge of the true geometry (see Table 4.2).

7. NAVIGATION WITH REFLECTED SIGNALS

The principle of navigation with reflected signals was introduced in Section 3.4. Pseudorange measurements from four or more GNSS satellites can be used to solve for the receiver position and velocity. If measurements of signals from four or more GNSS satellites reflecting off the same target can be related to the propagation path length of these signals, the target state can be solved for. In this chapter it will be assumed that the distance traveled by a reflected signal can be measured; the specifics of this measurement, and its feasibility, will be discussed in Chapter 8.

The relative navigation problem was examined in the context of spacecraft formation flying by [45], with a particular focus on high earth orbit (HEO). Crosslink signals between the members of the formation were incorporated. Thus, inter-vehicle range was estimated from reflected GNSS signals and reflected crosslink signals. All reflections were treated as specular reflections. Measurements were supplied to a Kalman filter in the form of singly differenced pseudoranges. Framing the state in Keplerian elements rather than Cartesian elements was shown to be more robust to measurement outages in the HEO case. The specific case of HSM4 was considered by [46] prior to the mission itself. The shuttle position was assumed known, and range measurements were supplied to an Extended Kalman Filter (EKF) in the form of differences between the direct and reflected pseudoranges. Range rate measurements were also used. The HST position was estimated using Hill's equations (also known as the Clohessy-Wiltshire equations) as a model for the relative dynamics.

The simplifications and assumptions used here are different than those discussed above. Although previous researchers have shown that relative navigation is feasible in principle, the objective of this chapter is to study target state estimation under conditions suitable for making reflected pseudorange measurements. Analysis of HSM4 data has suggested that separability of the direct and reflected signals is a significant

concern [59] [62]. Although the target spacecraft must be close enough to the receiver to produce sufficiently strong reflections, reflected signals with a longer additional path length are more easily distinguished from LOS signals.

Simplified target and chaser spacecraft trajectories have been generated based on HSM4 such that the two vehicles maintain a separation of approximately 80 meters. Spacecraft states are specified in Cartesian elements and restricted two body dynamics are used.

7.1 Problem Definition

In this simulation, the state of interest is

$$\mathbf{x} = \left[\mathbf{x}_{rcvr}^T \;\; \dot{\mathbf{x}}_{rcvr}^T \;\; \mathbf{x}_{targ}^T \;\; \dot{\mathbf{x}}_{targ}^T \;\; c\,b \;\; f\right]^T, \tag{7.1}$$

where $\mathbf{x}_{rcvr}$ and $\dot{\mathbf{x}}_{rcvr}$ are the receiver position and velocity respectively, $\mathbf{x}_{targ}$ and $\dot{\mathbf{x}}_{targ}$ the target position and velocity, $c\,b$ the receiver clock bias (in kilometers) and f the clock drift (in kilometers per second).

7.1.1 Measurement Model

It is assumed here that range measurements can be made from both the direct and reflected signals. As an example, these will be treated as direct and reflected pseudorange measurements. However, the measurement model used in the following estimation allows for any measurement technique that results in direct and reflected range information. This is further discussed in Chapter 8.

Pseudorange measurements are obtained from direct and reflected signals. The direct pseudorange from GNSS satellite i is

$$y_{direct,i} = |\mathbf{r}_i - \mathbf{x}_{rcvr}| + c\,b + v_{direct,i}. \tag{7.2}$$

The position of the i-th satellite is represented by $\mathbf{r}_i$. The reflected pseudorange measurement from GNSS satellite i is

$$y_{refl,i} = |\mathbf{r}_i - \mathbf{x}_{targ}| + |\mathbf{x}_{targ} - \mathbf{x}_{rcvr}| + c\,b + v_{refl,i}. \tag{7.3}$$

The measurement sensitivity matrix has the form

$$\mathbf{H} = \begin{bmatrix} \partial \mathbf{y}_{direct}/\partial \mathbf{x}_{rcvr} & \mathbf{0}_{M\text{x}3} & \mathbf{0}_{M\text{x}3} & \mathbf{0}_{M\text{x}3} & \mathbf{1}_{M\text{x}1} & \mathbf{0}_{M\text{x}1} \\ \partial \mathbf{y}_{refl}/\partial \mathbf{x}_{rcvr} & \mathbf{0}_{N\text{x}3} & \partial \mathbf{y}_{refl}/\partial \mathbf{x}_{targ} & \mathbf{0}_{N\text{x}3} & \mathbf{1}_{N\text{x}1} & \mathbf{0}_{N\text{x}1} \end{bmatrix} \tag{7.4}$$

for M direct measurements and N reflected measurements, where $\mathbf{1}_{j\text{x}k}$ and $\mathbf{0}_{j\text{x}k}$ indicate a j by k matrix of ones or zeros, respectively, and

$$\begin{aligned} \frac{\partial y_{i,direct}}{\partial \mathbf{x}_{rcvr}} &= \frac{-(\mathbf{r}_i - \mathbf{x}_{rcvr})}{|\mathbf{r}_i - \mathbf{x}_{rcvr}|} \\ \frac{\partial y_{i,refl}}{\partial \mathbf{x}_{rcvr}} &= \frac{-(\mathbf{x}_{targ} - \mathbf{x}_{rcvr})}{|\mathbf{x}_{targ} - \mathbf{x}_{rcvr}|} \\ \frac{\partial y_{i,refl}}{\partial \mathbf{x}_{targ}} &= \frac{-(\mathbf{r}_i - \mathbf{x}_{targ})}{|\mathbf{r}_i - \mathbf{x}_{targ}|} + \frac{(\mathbf{x}_{targ} - \mathbf{x}_{rcvr})}{|\mathbf{x}_{targ} - \mathbf{x}_{rcvr}|} \end{aligned}$$

for a particular satellite i. Note, however, that a reflected measurement from a satellite may not always exist when a direct measurement does and vice versa. In the sequential estimation case, the measurement noise for each measurement, $v_{direct,i}$ or $v_{refl,i}$, is calculated via a link budget. First a point solution is considered without measurement noise to demonstrate the solution convergence.

7.2 Point Solution

A receiver point solution is the location that best satisfies the overdetermined system of pseudorange measurements. This was introduced in Chapter 3 - the point solution is indicated by the $\mathbf{x}$ in Figure 3.3. The problem can be formulated as an optimization problem

$$\text{minimize} \qquad f(\hat{\mathbf{x}}) = \sum_{i=1}^{2N+2M} r_i(\hat{\mathbf{x}})^2, \tag{7.5}$$

for estimated state $\hat{\mathbf{x}}$, N LOS measurements and M reflected measurements, where r_i are the measurement residuals

$$r_i(\hat{\mathbf{x}}) = y_i - (\mathbf{H}\hat{\mathbf{x}} + v_i). \tag{7.6}$$

for measurement y_i - either a direct or reflected pseudorange. The sum of the squares of the measurement residual quantifies the error in the current estimated state. This

is an example of a nonlinear least squares problem, and the solution is the $\hat{\mathbf{x}}$ that minimizes the cost function $f(\hat{\mathbf{x}})$.

The Gauss-Newton method can be applied to the nonlinear least squares problem,

$$\hat{\mathbf{x}}^{(k+1)} = \hat{\mathbf{x}}^{(k)} - (\mathbf{H}^T\mathbf{H})^{-1}\mathbf{H}^T\mathbf{r}(\hat{\mathbf{x}}^{(k)}), \tag{7.7}$$

where $\mathbf{H}$ is the Jacobian of $\mathbf{r}$ given in Equation (7.4). Descent is guaranteed if the matrix $\mathbf{H}^T\mathbf{H}$, the Gramian, is positive definite; if it is not, the Levenberg-Marquardt modification can be used to ensure descent [63].

At a given time instant, measurements are computed according to the measurement model from the receiver, target, and GNSS satellite positions. Using the attitude-independent RCS of a conducting sphere [64] as the target's bistatic RCS, any satellite with an unobstructed line of sight to the target is treated as producing a reflected signal visible at the receiver. This is a first approximation; the actual visibility of a reflected signal will depend on the angle of incidence and target features at the point of incidence. There will likely be far fewer strong reflections visible at the receiver than the current approximation suggests.

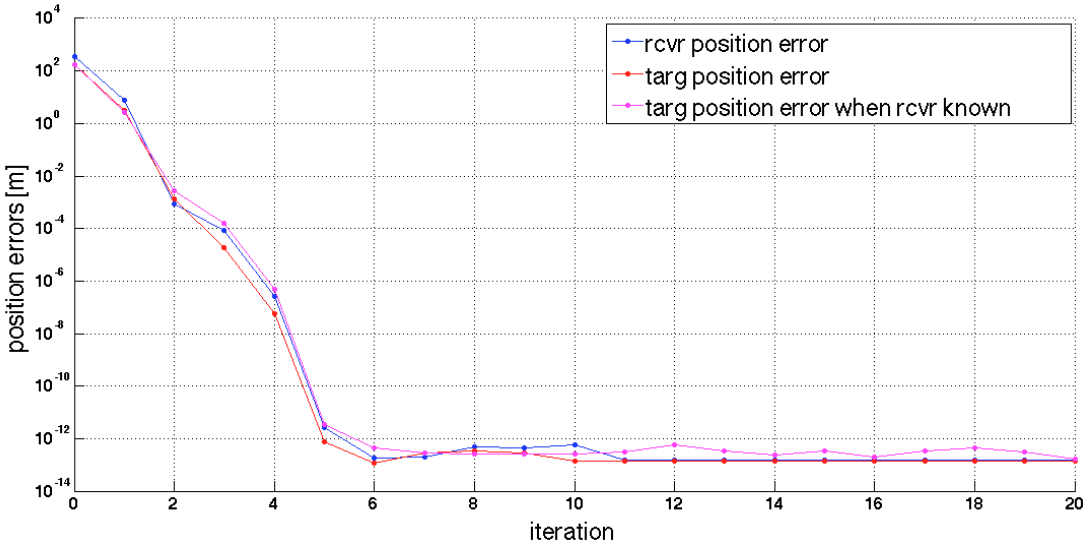

Fig. 7.1. Estimation of target and receiver positions via the Gauss-Newton algorithm

Figure 7.1 shows a typical run of the position and target estimation using simulated measurements. The results are consistent with the guarantee that the Gauss-Newton method converge with an order of at least two when the Gramian is positive definite [63]. In the case shown in Figure 7.1, only the position states are used. That is, pseudorange measurements are used to estimate the state

$$\mathbf{x} = \begin{bmatrix} \mathbf{x}_{rcvr} & \mathbf{x}_{targ} & c\,b \end{bmatrix}. \tag{7.8}$$

Note that in this section no measurement noise is applied - the point solution is used to demonstrate optimal solution convergence from an unknown initial state. As such, the errors in Figures 7.1 and 7.2 indicate only the convergence of the iteration, not the physical accuracy of the state estimate.

Two cases are considered: one in which the target and receiver states are estimated simultaneously, another in which the receiver state is assumed known (e.g., through a previously executed conventional GNSS point solution) and only the target position is estimated. Performance in either case appears comparable, and the errors essentially converge to zero, limited by machine precision ($2.2204\text{x}10^{-16}$).

The convergence is still superlinear when pseudorange rate measurements and velocity state components are included, but worse than the position-only case. The estimation of the full state in Equation (7.1) is shown in Figure 7.2. The errors in the target estimation case appear to be lower than those in the receiver estimation case. It is expected that target state estimation will be less robust than that of the receiver. However, due to the leniency in the reflected signal visibility criteria discussed above, more reflected signal measurements are available than direct ones here.

7.3 Sequential Estimation

Sequential estimation methods incorporate both prior state estimates and knowledge about the system dynamics to better estimate the instantaneous state of a time

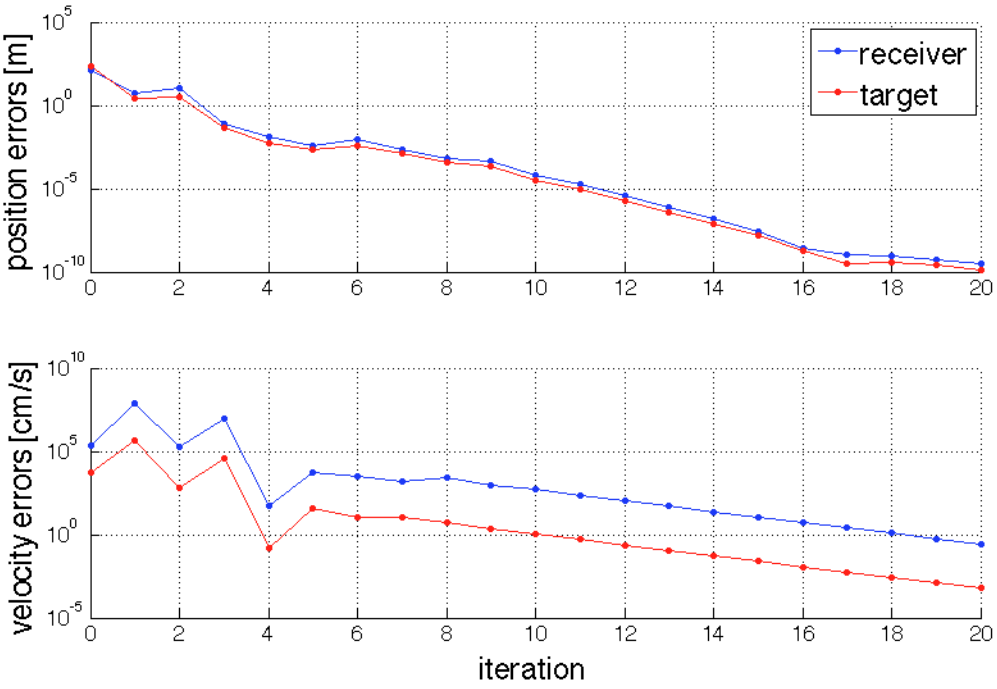

Fig. 7.2. Estimation of target and receiver positions and velocities via the Gauss-Newton algorithm

varying system. The discrete time Kalman filter is an estimation method of this class that can be used to estimate the state of a discrete time system of the form

$$\mathbf{x}_{k+1} = \mathbf{f}\left(\mathbf{x}_k, \mathbf{u}_k, \mathbf{w}_k, k\right) \tag{7.9}$$

$$\mathbf{y}_k = \mathbf{h}\left(\mathbf{x}_k, \mathbf{v}_k, k\right), \tag{7.10}$$

where $\mathbf{x}_k$ represents the state, $\mathbf{u}_k$ the input, and $\mathbf{w}_k$ the process noise at time k. Bold typeface is used to distinguish vector and matrix quantities from scalars. The subsequent state at $k+1$ is a linear function $\mathbf{f}(\cdot)$ of the current state, input, and measurement noise. The system state itself cannot be directly observed, however. Instead, an estimate of the state at time k is formed from measurements $\mathbf{y}_k$. The measurements are a linear function $\mathbf{h}(\cdot)$ of the state and measurement noise $\mathbf{v}_k$. The function $\mathbf{f}$ describes the system dynamics, and $\mathbf{h}$ the measurements.

In the case of spacecraft navigation, system dynamics and measurements are nonlinear, so the Kalman filter described above cannot be applied directly. Instead an EKF is used, which handles nonlinearities by linearizing the system about the current state estimate. This is an approximation, however; if the assumption of local linearity is invalid, the filter will diverge. Filter convergence is also highly dependent on the process noise and measurement noise covariance matrices, $\mathbf{Q}_k$ and $\mathbf{R}_k$ respectively. These are often treated as tuning matrices [21]. It is assumed that errors have zero mean and are uncorrelated.

A Kalman filter recursively propagates the first two moments of the distribution of the state, alternating between projections and measurement corrections [65]. Estimates of the state and state covariance prior to a measurement update are denoted with a superscript minus sign and referred to as *a priori* information. The state estimate is updated with a measurement according to

$$\hat{\mathbf{x}}_k^+ = \hat{\mathbf{x}}_k^- + \mathbf{K}_k(\hat{\mathbf{y}}_k - \mathbf{y}_k), \tag{7.11}$$

where the superscript plus sign indicates an *a posteriori* estimate. The new information contained in the measurement is incorporated in the state estimate via the measurement innovation $\hat{\mathbf{y}}_k - \mathbf{y}_k$, where the estimated measurement, denoted by $\hat{\mathbf{y}}$, is formed from the *a priori* state estimate by

$$\hat{\mathbf{y}}_k = \mathbf{h}(\hat{\mathbf{x}}_k^-). \tag{7.12}$$

The filter weighs the measurement update according to the gain matrix,

$$\mathbf{K}_k = \mathbf{P}_k^- \mathbf{H}_k^T (\mathbf{H}_k \mathbf{P}_k^- \mathbf{H}_k^T + \mathbf{R}_k)^{-1}, \tag{7.13}$$

where $\mathbf{H}_k$ is the Jacobian:

$$\mathbf{H}_k(\hat{\mathbf{x}}_k^-) = \frac{\partial \mathbf{h}(\hat{\mathbf{x}}_k^-)}{\partial \mathbf{x}}. \tag{7.14}$$

The state covariance is updated according to

$$\mathbf{P}_k^+ = (\mathbf{I} - \mathbf{K}_k \mathbf{H}_k)\mathbf{P}_k^- (\mathbf{I} - \mathbf{K}_k \mathbf{H}_k)^T + \mathbf{K}_k \mathbf{R}_k \mathbf{K}_k^T. \tag{7.15}$$

This form of the covariance update ensures that if $\mathbf{P}_k^-$ is symmetric, $\mathbf{P}_k^+$ will be as well [66].

After a measurement update, the state and state covariance estimates are projected by numerically integrating the dynamics model, forming *a priori* estimates for the subsequent time step. The conventional sequential estimation methods described above are implemented using the Orbit Determination Toolbox (ODTBX), a mission simulation and analysis tool developed in MATLAB by engineers at GSFC [67]. The measurement model is described above. Additional features and the dynamics models developed for this specific problem are described in the following sections.

7.3.1 Measurement Weighting

As described in Section 3.2, the power delivered to the receiver by a LOS signal is determined by the Friis transmission equation, and the power delivered to the receiver by a reflected signal is determined by the bistatic radar equation. Gain patterns of the flight antennas are used that were measured in the GEMAC, as described in Section 4.3, but the gain average over azimuth is used (shown in Figure 4.4). In this simulation, measurements are excluded that have a calculated C/N_0 below 25 dB-Hz.

Measurements can be weighted according to the measurement covariance matrix. The C/N_0 from the link budget calculation is used to approximate the covariance of each link. The ranging error resulting from a given signal power spectral density is dependent on a number of receiver properties. For a receiver with a conventional early/late type discriminator, the standard deviation of the code range measurement in chips is given by

$$\sigma_{DLL} = \sqrt{\frac{2d^2 B_n}{(C/N_0)}\left[2(1-d) + \frac{4d}{T(C/N_0)}\right]}, \tag{7.16}$$

where d is the correlation spacing between the early and late discriminators in chips, B_n the code loop noise bandwidth in Hz and T the pre-detection integration time in seconds [24]. These parameters are taken from the Navigator GPS receiver flown on HSM4 [4]. Although this weighting is not used in the Navigator receiver itself, filter

performance is shown to be improved here by calculating the diagonal elements of $\mathbf{R}_k$ according to the link budgets and Equation (7.16).

7.3.2 Dynamics Model

The dynamics model separates the state in Equation (7.1) into three independent components: receiver, target and clock.

Each spacecraft state is propagated using the dynamics of the restricted two-body problem, a simplified model of orbital mechanics in which only the Earth and the spacecraft are considered and the spacecraft mass is much less than the mass of the central body [68]. The state derivative is calculated,

$$\begin{bmatrix} \dot{x} \\ \dot{y} \\ \dot{z} \\ \ddot{x} \\ \ddot{y} \\ \ddot{z} \end{bmatrix} = \begin{bmatrix} \dot{\mathbf{r}}_{s/c} \\ \\ -\mu \frac{\mathbf{r}_{s/c}}{|\mathbf{r}_{s/c}|^3} \end{bmatrix} \tag{7.17}$$

and integrated over the propagation interval, where $\mathbf{r}_{s/c}$ and $\dot{\mathbf{r}}_{s/c}$ are the position and velocity components of the spacecraft state, respectively, and μ is the gravitational parameter for the Earth (3.986×10^5 km^2/s^2). The derivative of the process noise matrix for each spacecraft is diagonal (i.e., the derivatives of the process noise terms are assumed uncorrelated) and constant, with a standard deviation of 0 km^2/s and 1×10^{-9} km^2/s^2 for the velocity and acceleration dimensions, respectively.

A simple two-state clock dynamics model included in ODTBX is used, where the derivative,

$$\begin{bmatrix} f \\ \dot{f} \end{bmatrix} = \begin{bmatrix} 0 & 1 \\ 0 & 0 \end{bmatrix} \begin{bmatrix} c \cdot b \\ f \end{bmatrix}, \tag{7.18}$$

is integrated over the propagation interval [67]. The derivative of the process noise matrix is defined as

$$\dot{\mathbf{Q}}_{clk} = \begin{bmatrix} c^2 h_0/2 & 0 \\ 0 & c^2 2\pi^2 h_{m2} \end{bmatrix} \tag{7.19}$$

where h_0 and h_{m2} represent classical Allan variance parameters; here $h_0 = 2.4 \times 10^{-22}$ and $h_{m2} = 8.0 \times 10^{-28}$ [21].

Initial State and State Covariance

Errors in the components of the initial state estimate are assumed uncorrelated, so the initial state covariance $\mathbf{P}_0^-$ is a diagonal matrix. In a rendezvous and docking scenario like HSM4, the receiver position is likely available from conventional navigation systems, so knowledge of the initial receiver position is expected to be better than that of the target. The standard deviations of the receiver and target positions are chosen to be 10 m and 1 km respectively. Velocity and position are physically related quantities, so the covariance of the velocity terms should be consistent with the covariance of the position terms. For this simulation the velocity covariance was related to the position covariance by

$$\sigma^2_{velocity} = \left(\frac{\mu}{|\mathbf{r}_{s/c}|^2 |\dot{\mathbf{r}}_{s/c}|} \right) \sigma^2_{position}, \tag{7.20}$$

a relationship obtained by manipulating the relationship between an orbit's semi-major axis, orbital radius, orbital velocity, and orbital energy.

The initial state estimate is calculated as

$$\mathbf{x}_0^- = \mathbf{x}_{0,true} + \mathbf{x}_{err} \tag{7.21}$$

where $\mathbf{x}_{0,true}$ is read from a file of the generated true spacecraft trajectories. The initial clock bias is set to -2 km and the initial clock drift to 5 m/s, a typical drift for an oven-controlled crystal oscillator (OCXO) [12]. The perturbation of the initial state, $\mathbf{x}_{err}$, is sampled from $\mathcal{N}(0 \text{ m}, 100 \text{ m}^2)$ in the position dimensions.

7.3.3 Results

The number and strength of reflected signals depends on the EM scattering properties of the target. A previous simulation of HSM4 using EM ray tracing software suggests that numerous reflected signals exist during the period of approach when the inter-vehicle range is approximately 80 meters [59]. The rays scattered by HST vary with the spacecraft's attitude, but as a first approximation two scattering models will be considered that are attitude independent: a specular reflection and a perfectly conducting sphere.

Estimation was performed over a simulation duration of 1.5 hours with measurement updates every 90 seconds. The previous EM ray tracing simulation indicated that nearly all reflected signals at the receiver were produced by satellites above the receiver horizon (i.e., less than 90 degrees from the antenna boresight) [59], so in this simulation signals from satellites below this horizon were masked.

Specular Reflection Model

The study of relative navigation in [45] assumed each signal visible to the reflecting spacecraft would result in a specular reflection. This mirror-like reflection has the effect of simply extending the signal propagation path, avoiding the additional spreading loss in Equation (3.14) associated with a signal that is re-radiated at the point of reflection. In the specular case, the power delivered to the receiver by a reflected signal is determined by

$$P_{R,refl} = \frac{P_T G_T G_R \lambda_{L1}^2}{(4\pi)^2 (R_T + R_R)^2} \Gamma^2, \tag{7.22}$$

where the Fresnel reflection coefficient $\Gamma \approx 0.9$, as in [45].

This model affects all reflected signals equally, resulting in an attenuation of approximately 2 dB relative to the corresponding LOS signals. Every reflected signal is still above the 25 dB-Hz tracking threshold. A constant measurement covariance of 36 m^2 was used for all direct and reflected measurements. Figures 7.3 and 7.4 show

the spacecraft position RSS errors from 50 simulations. The RSS position errors are plotted as dots and the state covariance for each run is plotted as a black line. Both the receiver and target states are estimated to within less than a meter.

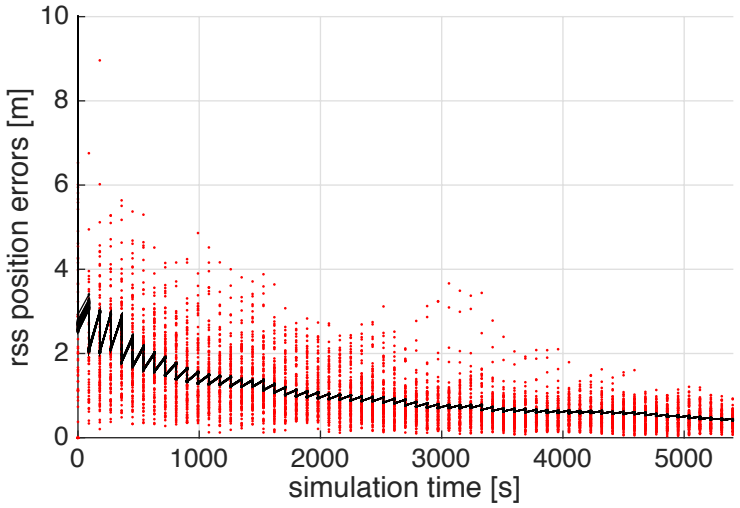

Fig. 7.3. Receiver position estimation in specular reflection case

Sphere Target Model

A perfectly conducting sphere has an RCS given by

$$\sigma_b = \pi a^2 \left(1 - \frac{\sin(2ka)}{ka} + \frac{1-\cos(2ka)}{(ka)^2}\right), \tag{7.23}$$

with k the wave number (for L1 in our case) and a the sphere radius [69]. As in the specular case, every LOS signal results in a reflected signal for every LOS signal. However, the radius of the sphere was adjusted to produce an attenuation of approximately 21 dB relative to the corresponding LOS signals, so only between four and six reflected signals exceeded the acquisition threshold at a given time. Again the constant measurement covariance of 36 m^2 was used for all direct and reflected measurements.

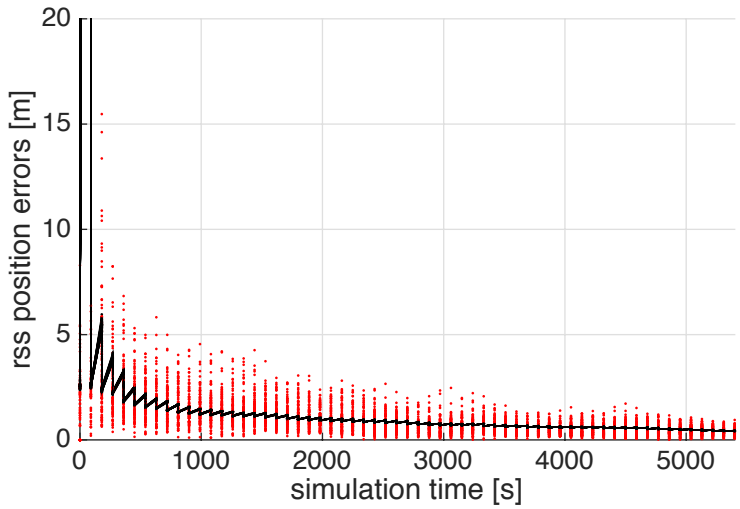

Fig. 7.4. Target position estimation in specular reflection case

Figures 7.5 and 7.6 show the spacecraft position estimate results for the receiver and target respectively from 50 runs. The performance is worse than in the specular case, particularly for target position estimation. This is not surprising, given the small number of reflected measurements being made, but both position estimates converge to within a few meters for most runs. Figure 7.7 shows improved filter performance when the measurement weighting via Equation (7.16) is used. In the target case, shown in Figure 7.8, the performance is comparable to the non-weighted case. The covariance bounds are more accurate, however, giving the impression of poorer performance.

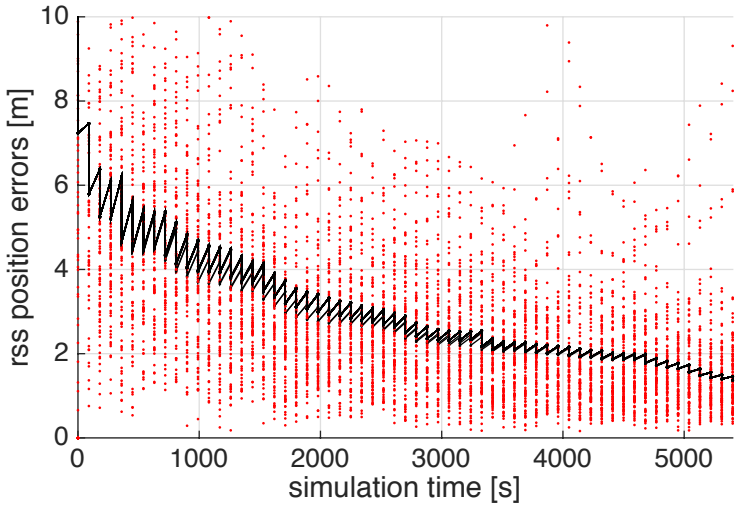

Fig. 7.5. Receiver position estimation in sphere case with fixed measurement covariance

7.4 Relative Navigation Dilution of Precision

In conventional satellite navigation, the relationship between the pseudorange error and the receiver position estimate is quantified by the geometric dilution of precision (GDOP),

$$\text{GDOP} = \frac{1}{\sigma} = \sqrt{\sigma_x^2 + \sigma_y^2 + \sigma_z^2 + \sigma_b^2} = \sqrt{\text{tr}((\mathbf{H}^T\mathbf{H})^{-1})} \tag{7.24}$$

for the three position dimensions and the clock bias dimension [70]. The trace is denoted tr and $\mathbf{H}$ is the measurement sensitivity matrix in Equation (7.4). GDOP provides a metric for position estimate quality based on the geometry of the GNSS satellites relative to the user for a given pseudorange error.

For GDOP in the case of relative navigation, consider the notation in Figure 7.9. The unit vector from the receiver to the i-th satellite is $\hat{d}$ (the direction of the direct signal), the unit vector from the receiver to the target is $\hat{r}$, and the unit vector from

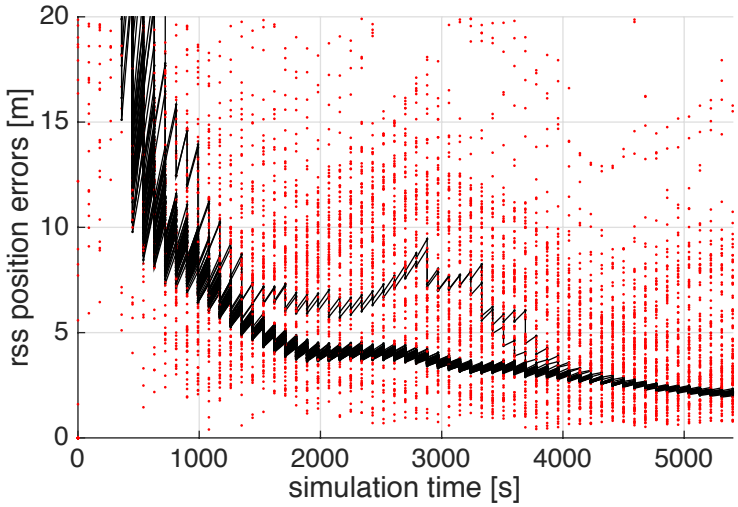

Fig. 7.6. Target position estimation in sphere case with fixed measurement covariance

the target to the i-th satellite is $\hat{t}_i$. In accordance with the partial derivatives defined for Equation (7.4) these unit vectors are 1x3. Then $\mathbf{H}$ is

$$\mathbf{H} = \begin{bmatrix} -\hat{d}_1 & \mathbf{0}_{1x3} & \mathbf{0}_{1x3} & \mathbf{0}_{1x3} & 1 & 0 \\ -\hat{r} & \mathbf{0}_{1x3} & -\hat{t}_1 + \hat{r} & \mathbf{0}_{1x3} & 1 & 0 \\ \vdots & \vdots & \vdots & \vdots & \vdots & \vdots \\ -\hat{d}_N & \mathbf{0}_{1x3} & \mathbf{0}_{1x3} & \mathbf{0}_{1x3} & 1 & 0 \\ -\hat{r} & \mathbf{0}_{1x3} & -\hat{t}_M + \hat{r} & \mathbf{0}_{1x3} & 1 & 0 \end{bmatrix} \tag{7.25}$$

The Gramian can be written in terms of blocks

$$\mathbf{H}^T\mathbf{H} = \begin{bmatrix} \mathbf{A} & \mathbf{0}_{3x3} & \mathbf{B} & \mathbf{0}_{3x3} & \mathbf{C} & \mathbf{0}_{3x1} \\ \mathbf{0}_{3x3} & \mathbf{0}_{3x3} & \mathbf{0}_{3x3} & \mathbf{0}_{3x3} & \mathbf{0}_{3x1} & \mathbf{0}_{3x1} \\ \mathbf{B} & \mathbf{0}_{3x3} & \mathbf{D} & \mathbf{0}_{3x3} & \mathbf{E} & \mathbf{0}_{3x1} \\ \mathbf{0}_{3x3} & \mathbf{0}_{3x3} & \mathbf{0}_{3x3} & \mathbf{0}_{3x3} & \mathbf{0}_{3x1} & \mathbf{0}_{3x1} \\ \mathbf{C}^T & \mathbf{0}_{1x3} & \mathbf{E}^T & \mathbf{0}_{1x3} & N+M & 0 \\ \mathbf{0}_{1x3} & \mathbf{0}_{1x3} & \mathbf{0}_{1x3} & \mathbf{0}_{1x3} & 0 & 0 \end{bmatrix} \tag{7.26}$$

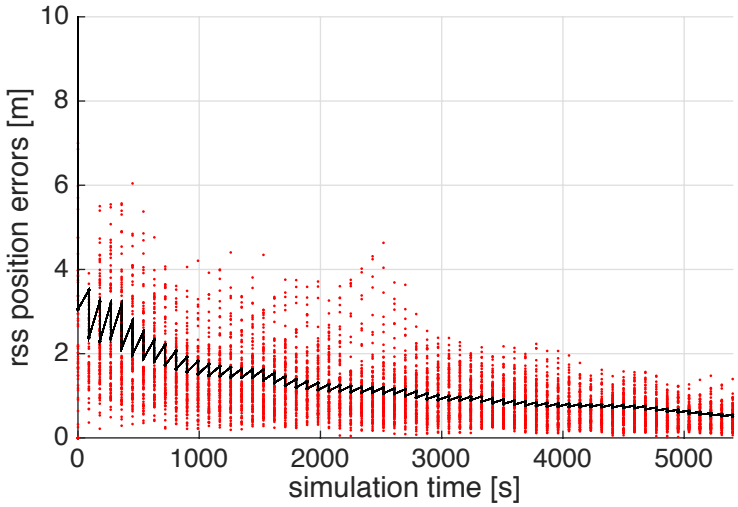

Fig. 7.7. Receiver position estimation in sphere case with variable measurement covariance

where

$$A = \sum_{i=1}^{N} \hat{d}_i^T \hat{d}_i + M\hat{r}^T\hat{r}, \tag{7.27}$$

$$B = \sum_{i=1}^{M} \hat{r}^T(\hat{t}_i - \hat{r}), \tag{7.28}$$

$$C = -\sum_{i=1}^{N} \hat{d}_i - M\hat{r}_i^T, \tag{7.29}$$

$$D = \sum_{i=1}^{M} \hat{r}^T(\hat{t}_i - \hat{r}) \tag{7.30}$$

$$E = -\sum_{i=1}^{M} \hat{t}_i^T + M\hat{r}^T. \tag{7.31}$$

GDOP can be formulated according to [70],

$$\text{tr}\left[(H^T H)^{-1}\right] = \left[\frac{1}{det(H)^2}\sum_{ij}(h'_{ij})^2\right] \tag{7.32}$$

where $h'_{ij}/det(H)$ are the elements of H^{-1} and h'_{ij} are the elements of adjoint matrix.

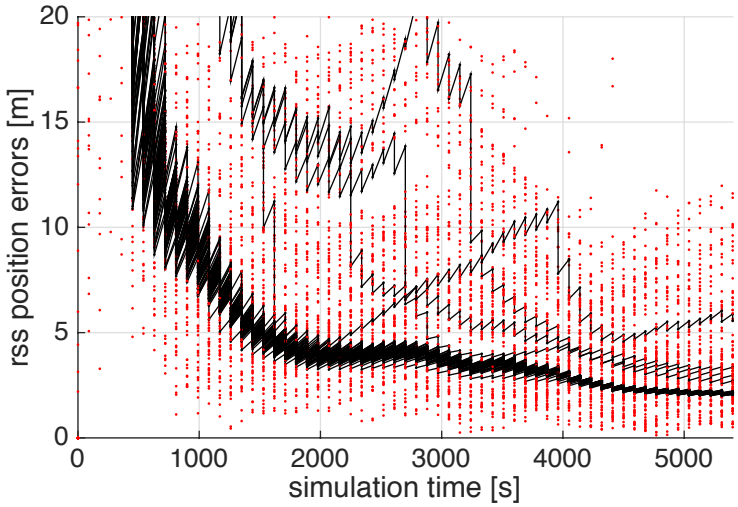

Fig. 7.8. Target position estimation in sphere case with variable measurement covariance

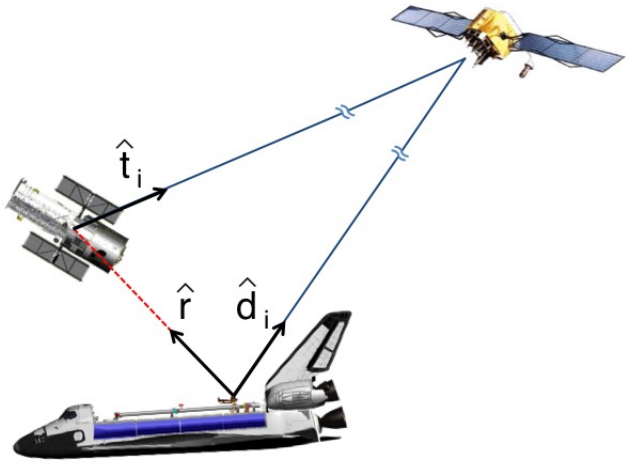

Fig. 7.9. Relative navigation geometry

7.4.1 Two Dimensions

For N GNSS satellites in two dimensions, GDOP is minimized by arranging satellites as the vertices of an N-sided polygon [70]. Limiting visibility to above the

receiver horizon, the optimal arrangement of satellites is from 0 to 180 degrees spaced by $\Delta\theta = 180/(N-1)$. If the receiver is placed at the origin and satellites are placed at their respective angles 24,000 km from the receiver, the relative GDOP can be compared for a variety of target spacecraft locations. Relative GDOP is shown in Figure 7.10 over target angle relative to the horizon. The optimal orientation of the target increases from 24° to 38° as the number of satellites grows. Distance between the target and receiver does not change relative GDOP - here 80 meters is used.

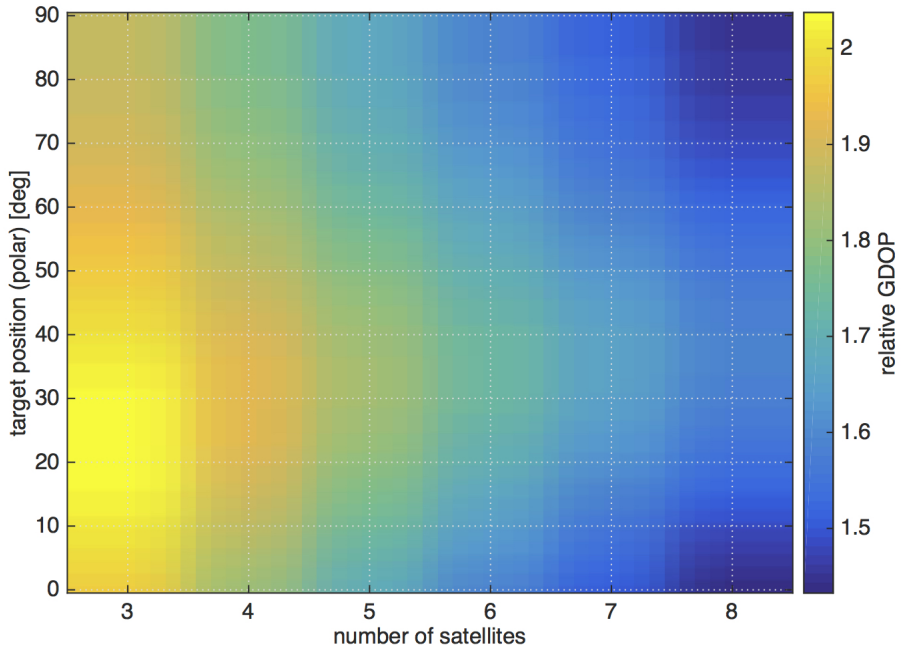

Fig. 7.10. 2D relative GDOP over HST position and number of GNSS satellites

8. RANGE MEASUREMENTS FROM MULTIPATH

8.1 Measurement Model Assumptions

The demonstration of relative navigation using reflected signals in Chapter 7 relied on several assumptions. The first is that reflected signals are available. The scattering cross sections used were greatly simplified, and these simplifications favored reflected signal availability. Every signal incident on the target was treated as a reflected signal source, and only power attenuation due to the link budget prevented these signals from being received. In actuality, target surface features will scatter the incident signals in a variety of directions, limiting the number of signals visible to the receiver. However, EM ray tracing has suggested that in the case of HSM4, numerous reflected signals of sufficient strength, duration, and variety for navigation are available. With a higher fidelity dynamics model, the shuttle and HST trajectories could be used for the navigation simulation, and EM ray tracing results could be used as inputs to the measurement model. This would improve the accuracy of the navigation simulation. Because of the large number of reflections predicted by ray tracing, however, the underlying assumptions of the measurement model itself are of more interest here.

The measurement model consisted of a measurement of the LOS range, and a measurement of the path length of the reflected signal. In Chapter 7, it was assumed that reflected signals could be isolated from the LOS signals and tracked independently to form reflected pseudoranges. This is the ideal case, in which signal polarization is fully reversed upon reflection, and the RCP and LCP antennas have excellent cross-polarization rejection, forming two separate data sets of direct and reflected signals respectively. The RNS experiment was designed with this methodology in mind [9].

Retaining the first assumption, that polarization is perfectly reversed upon reflection, the feasibility of this measurement model relies on the antennas to sufficiently

isolate incident RCP and LCP energy. Consider the multipath-induced code tracking error in Equation (6.7) for an antenna with RCP gain G_R and LCP gain G_L:

$$\tau_M = \frac{\left(\alpha\frac{G_L}{G_R}\right)^2 \delta + \alpha\frac{G_L}{G_R}\delta\cos\psi}{1 + \left(\alpha\frac{G_L}{G_R}\right)^2 + 2\alpha\frac{G_L}{G_R}\cos\psi}. \tag{8.1}$$

In the case of a very good RCP antenna, G_L is small and τ_M approaches zero. Thus the measured pseudorange is the multipath-free

$$\rho_{RCP} = r + ct_{b,R} - ct_{b,s} + I_{L1} + T + 0 + v_{RCP}. \tag{8.2}$$

For a very good LCP antenna, G_R is small, and in the limit τ_M approaches δ, the multipath relative delay in seconds. This is the case of reflected signal tracking, and the measured pseudorange is

$$\rho_{LCP} = r + ct_{b,R} - ct_{b,s} + I_{L1} + T + c\delta + v_{LCP}. \tag{8.3}$$

Reflected signal tracking can be confirmed by taking the difference between the pseudoranges measured through the two antennas to find the excess pseudorange

$$\rho_{LCP} - \rho_{RCP} \approx c\delta = R_\Delta, \tag{8.4}$$

where R_Δ is the geometric additional path length of the reflected signal relative to the direct: $R_\Delta = (R_T + R_R) - R_{LOS}$ (see Figure 3.1).

8.1.1 Simulation

Data from a good RCP antenna was simulated with Siggen by applying a 20 dB attenuation to the reflected signals, and from a good LCP antenna by applying a 20 dB attenuation to the direct signals. Under these conditions the reflected signals were well isolated in the LCP data set and tracking of the LCP data locks onto reflected signals. Excess pseudorange, shown in Figure 8.1, was computed by finding the difference between the RCP and LCP pseudoranges. Excess range calculated from the truth geometry is given by the corresponding dashed lines for each PRN. The excess

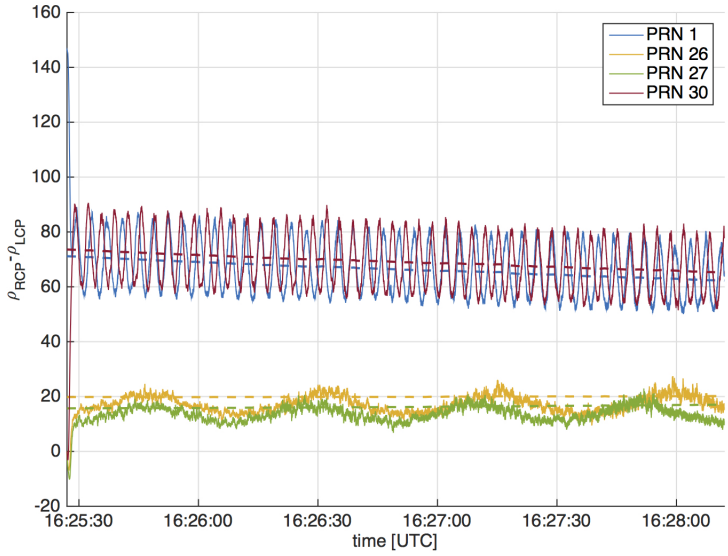

Fig. 8.1. Simulation: excess pseudorange with 20 dB cross-pole discrimination

pseudorange and truth geometry show strong agreement, indicating that reflected signal range measurements are feasible with sufficient cross-pole discrimination.

This measurement begins to break down, however, as antenna isolation decreases. For less than perfect antennas, both the RCP and LCP data sets contain a mix of direct and reflected signals. The pseudoranges suffer from error due to the presence of interfering signals:

$$\rho_{RCP} = r + ct_{b,R} - ct_{b,s} + I_{L1} + T + (0 + \tau_{M,RCP}) + v_{RCP}, \tag{8.5}$$

$$\rho_{LCP} = r + ct_{b,R} - ct_{b,s} + I_{L1} + T + (c\delta + \tau_{M,LCP}) + v_{LCP}. \tag{8.6}$$

Excess pseudorange departs from the excess geometric range of the reflected signals as this error increases. For large enough errors,

$$\rho_{LCP} - \rho_{RCP} \approx (\tau_{M,LCP} - \tau_{M,RCP} + c\delta) \neq R_{\Delta}. \tag{8.7}$$

This error is already apparent in the oscillation of the excess pseudorange measurement in the 20 dB case, but the measurement still sufficiently approximates R_{Δ}. This approximation breaks down as the antennas degrade. In Figure **??**, for example, at a

cross-pole discrimination of 10 dB the LOS-induced tracking errors experienced when tracking the reflected signal overwhelm the measurement of R_Δ. Eventually tracking of the reflected signal fails altogether. The cross-pole discrimination at which measurement of the reflected signal pseudorange fails depends on polarization reversal at reflection, reflected signal strength, and receiver features such as early-late correlator spacing. However, with the LCP antenna's cross-pole discrimination of 7 dB, the HSM4 GPS data was likely collected under conditions for which the approximation in Equation (8.4) is invalid.

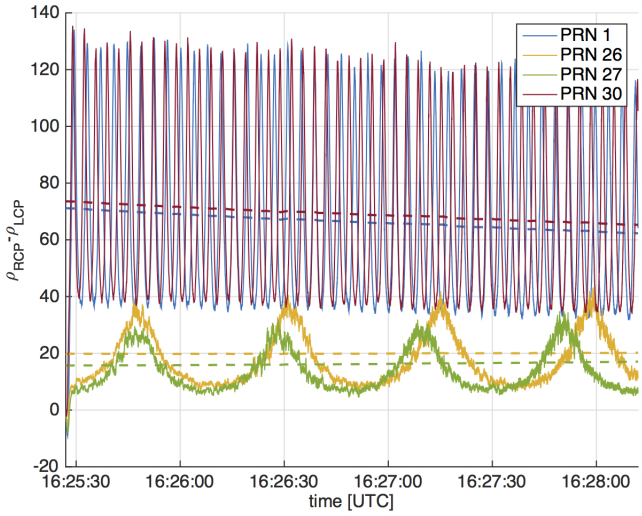

Fig. 8.2. Simulation: excess pseudorange with 10 dB cross-pole discrimination

8.1.2 Experiment

The initial concept of operations for relative navigation using reflected GNSS signals during HSM4 relied on tracking reflected signals in the LCP data. The excess path length of the reflections could then be computed through comparison to LOS signal tracking in the RCP data [9]. Initial results suggested this might be feasible. In 2010, Shah et al. performed repeated acquisition of PRN 19 to show that a correlation peak was visible in the LCP data that was not visible in the RCP data [71].

Furthermore, this peak exhibited a Doppler shift relative to the LOS rate of change consistent with the inter-vehicle motion. At the time studied, 16:17:45 UTC, PRN 19 was located below the horizon of the space shuttle, so that a LOS signal was not visible and the bistatic angle was nearly 90°. This geometry is particularly conducive to reception of strong Hubble reflections. In the absence of a corresponding LOS signal, however, ranging relies on a good estimate of the LOS range to the transmitting satellite. Focus was instead directed at those cases where direct and reflected signals are simultaneously visible.

Using the RNS SDR, a large number of signals were acquired in the LCP data, suggesting an abundance of strong reflections. C/N_0 estimates from acquisition are shown in Figure 8.3, where the LCP results are plotted on top of the RCP results. An LCP signal is acquired for every RCP case, and a few times in cases without an RCP peak (such as PRN 19 mentioned previously). The 25 dB-Hz acquisition threshold is shown by a dashed line. Even if every LCP signal acquired is a reflected signal, the small power difference relative to the corresponding RCP signals suggests a nearby reflection, possibly from within the shuttle cargo bay around the antenna. Nevertheless, a few signals seem promising.

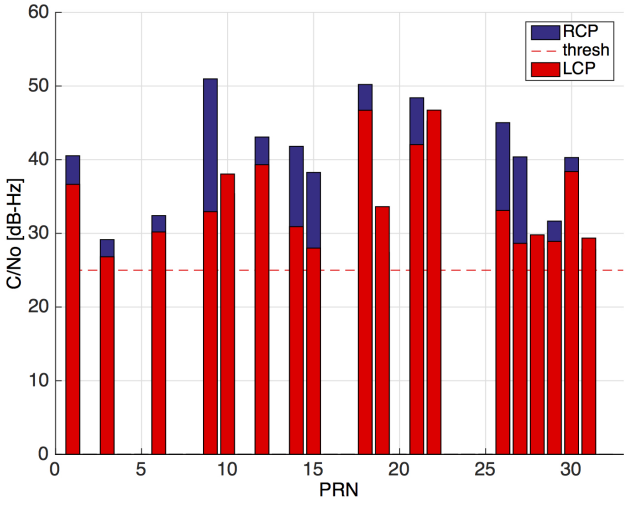

Fig. 8.3. C/N_0 estimated by acquisition (16:17:45 UTC)

NavSDR was used to perform conventional tracking on the RCP and LCP data sets for the entire duration of rendezvous (16:12:09-17:13:56 UTC). A summary of the number of signals tracked is shown in Figure 8.4. The number of LCP signals tracked and the lack of variation in this number as the inter-vehicle range decreases suggests that many of the signals being tracked in the LCP data are either reflections from within the shuttle bay or LOS signals strong enough to dominate despite the antenna polarization mismatch. This hypothesis is further borne out by the results of subtracting the measured RCP pseudorange from the measured LCP pseudorange for all PRNs tracked in both data sets, shown in Figure 8.5. The average pseudorange difference is approximately zero. There are no persistent pseudorange differences above forty meters, as would be expected if a reflected signal were being tracked prior to 16:50 UTC.

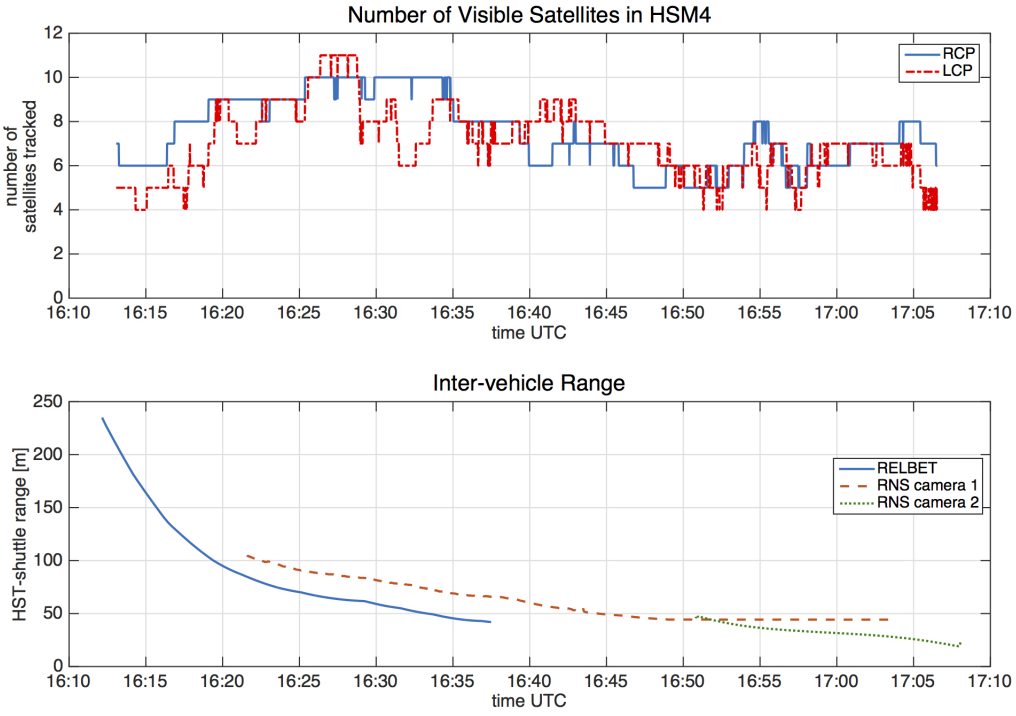

Fig. 8.4. Number of satellites tracking by NavSDR and inter-vehicle range

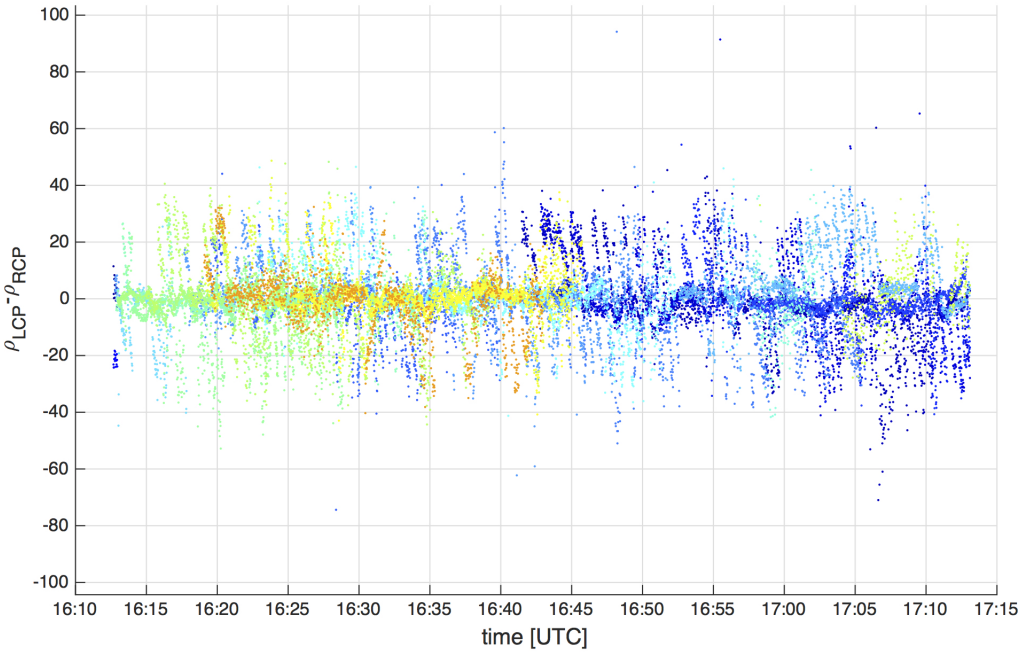

Fig. 8.5. LCP pseudorange minus RCP pseudorange from NavSDR

Tracking was then performed with RNS SDR to study the correlations in more detail. Excess pseudorange measurements analogous to those made in the simulation case are shown in Figure 8.6. As expected in the case of poor antenna isolation, the tracked PRNs 1, 26 and 30 exhibit a mean LCP/RCP pseudorange difference of zero. Tracking of PRN 30 fails in the LCP data halfway through, and tracking of PRN 27 fails in both cases.

8.2 Alternatives

In the absence of reflected signal isolation via polarization, propagation path length of reflected signals must be determined through other means if the same measurement model is to be retained. One approach is to estimate the reflected signal properties through the distortion of the code correlation shape, as in the MEDLL algorithm [36]. In the case of spacecraft docking, the relative velocity of the target spacecraft is slow, so the resulting Doppler shift of the reflected signals (on the order

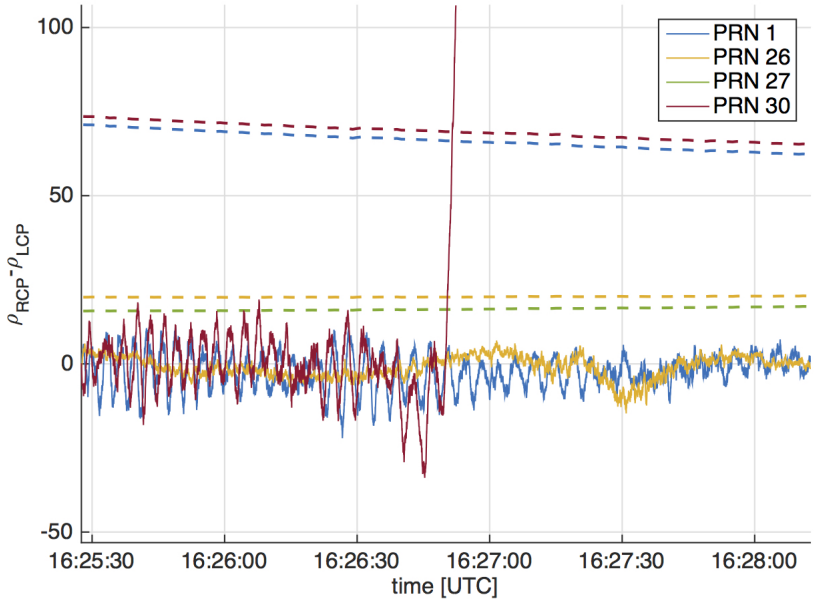

Fig. 8.6. Experiment: measured excess pseudorange

of Hz) can be ignored. Only the code dimension of the ambiguity function need be considered for multipath measurement. The code correlation is a sum of the correlation with the LOS signal and delayed, attenuated replicas created by reflections. The simple baseband case of two PRN codes is shown in Figure 8.7, where the measured "composite" correlation is a result of the two individual correlations. This is a simplification, but a good description of how multipath arises in code correlation power, i.e., the sum of the squared in-phase and quadrature correlations.

As described in Section 2.3.3, a conventional tracking loop performs correlations with three shifted C/A code replicas: a "prompt" code shifted to align with the instantaneous code phase estimate, and "late" and "early" codes shifted to lag and lead the prompt code respectively. Each correlation with an offset code is referred to as a correlator. Performing many correlations, closely spaced in delay, provides a more detailed view of the correlation shape. This bank of correlators concept has been employed by other researchers [36] [10], and even incorporated into tracking [72]. An example of the polycorrelator visualization is shown in Figure 8.8, in which

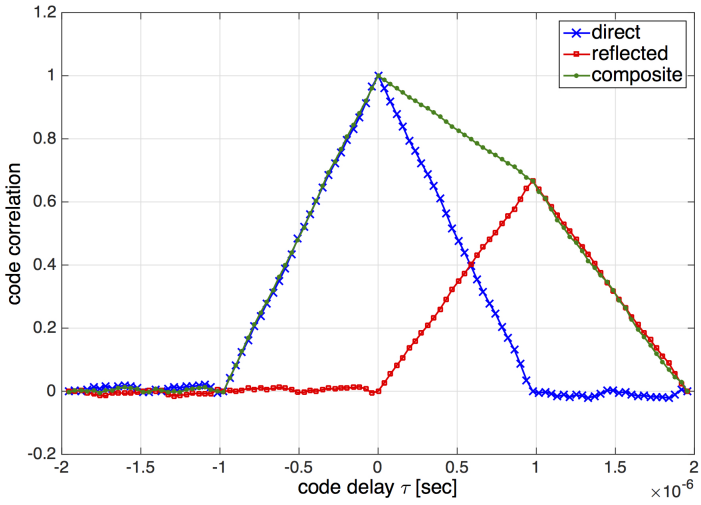

Fig. 8.7. Code correlation in the presence of a reflected signal

correlations are calculated over ±2 chips at each time and plotted sequentially (from bottom to top, in the 2D plot). A single reflected signal is immediately evident in this case when the multipath is offset by several hundred meters relative to the LOS signal tracked by the prompt correlator. A black line is overlaid on the two-dimensional plot at the true delay offset of the simulated multipath and clearly corresponds to the secondary correlation peak.

The example shown in Figure 8.8 is unrealistic for the cases of interest. It's unlikely that a signal with an excess path length of hundreds of meters would be so strong. A more realistic example, using parameters from EM ray tracing, correlation magnitude for PRN 30 is shown in Figure 8.9. A black line is overlaid on the two-dimensional plot at the true delay offset of the simulated multipath. Unlike the extreme case of Figure 8.8, the reflected signal is within the main lobe of the code correlation function and a secondary peak cannot be distinguished.

Similarly, the results of tracking PRN 30 in the HSM4 data in Figure 8.10 show no sign of a secondary correlation peak. In Figure 8.10(a) the correlation magnitude is shown for the same time frame as the simulation results in Figure 8.9. There does not appear to be any deformation of the correlation shape corresponding to a reflected

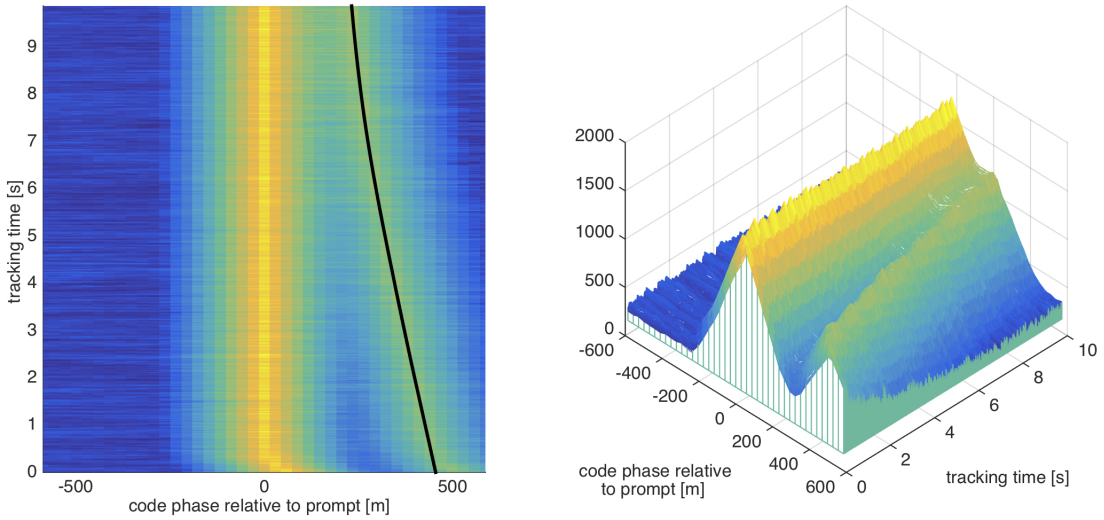

Fig. 8.8. Polycorrelator view: tracking a simulated signal in the presence of a single multipath signal

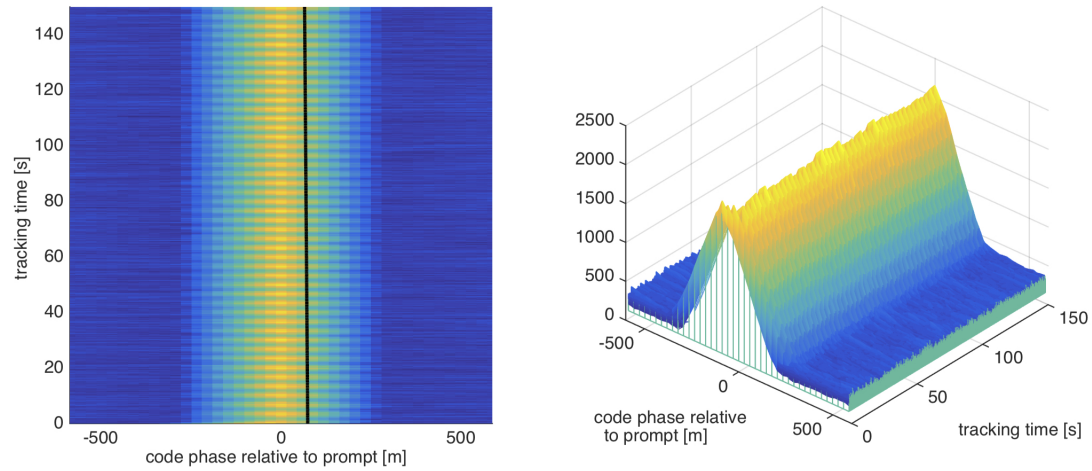

Fig. 8.9. Simulation: PRN 30 correlation magnitude 16:25:27 to 16:28:12 UTC

signal. This is made clearer by looking at the correlation symmetry, subtracting the left side of the correlation plot (corresponding to negative delay relative to the prompt correlator) from the right side of the correlation plot in Figure 8.10(b). If a reflected signal offset by less than one chip were present, a bulge in the positive half of the correlation function would result in a positive difference between the positive

and negative delay sides of the correlation function. No such asymmetry is evident. Results are similar for the other example PRNs identified to have reflections via EM ray tracing that were discussed in Chapter 5 (1, 26 and 27).

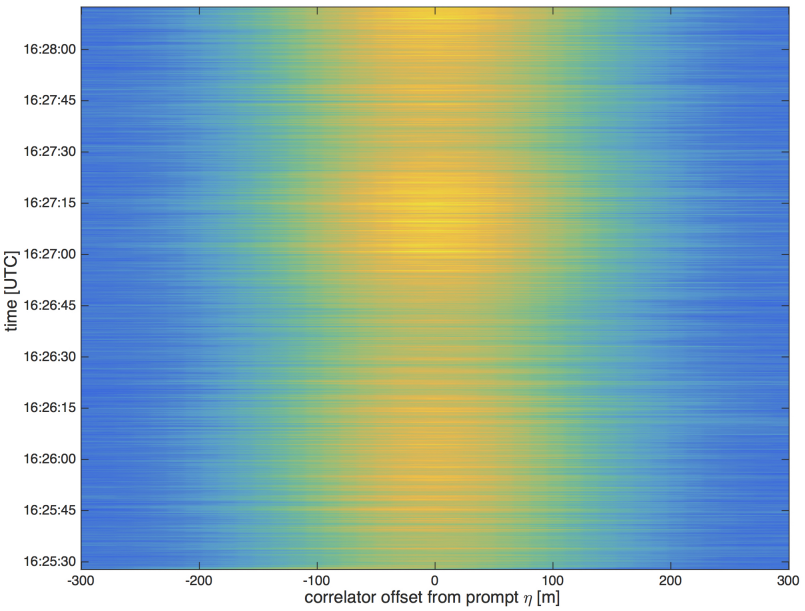

(a) correlation magnitude

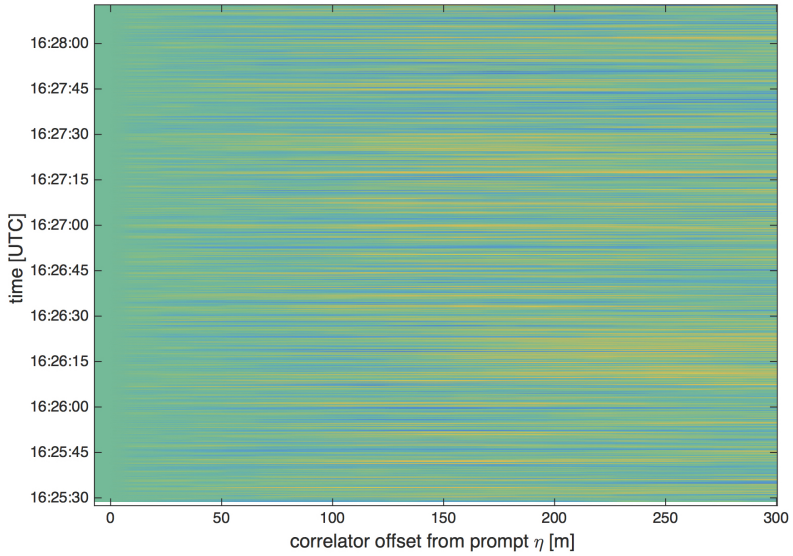

(b) RCP correlation symmetry

Fig. 8.10. Experiment: PRN 30 correlation measurements 16:25:27-16:28:12 UTC

Although the multipath signal can clearly be perceived through the composite correlation shape in Figure 8.7, this is complicated by the effect of front end filtering (see Figure 2.2). As a sequence of square pulses, a C/A code has an inherently infinite bandwidth. If the incoming signal is sampled at a 2.048 MHz (as in the case of HSM4), the signal must first be band-limited to less than half the sampling frequency in order to avoid aliasing. The reduction of signal bandwidth, indicated by the tilde in the signal models in Chapters 2 and 3, leads to a smoothing of the code correlation functions.

An example is shown in Figure 8.11 using the relative delay and amplitude of the multipath predicted by ray tracing for PRN 1 at 16:23 UTC. This is the same correlator number and spacing used in Figure 8.9. Here the green plot shows the correlation function of the composite signal without front-end filtering (as in the large multipath offset case in Figure 8.9). The black plot shows the code correlation function when the input signal is low-pass filtered with a cutoff frequency of 1.023 MHz (slightly wider than the two-sided 2 MHz bandwidth of the bandpass filter applied during HSM4). Under these conditions, a reflected signal so closely offset from the LOS signal (as expected in the case of Hubble reflections) does not manifest itself in deformation of the correlation function shape, but rather in a shift of the correlation peak.

Although the RCP and LCP antennas do not provide absolute isolation of direct and reflected signals, their effects can still be exploited. A direct signal may dominate when performing tracking on the LCP data, but the ratio of reflected signal power to the direct will be greater. This may not enable tracking of the reflected signal itself, but the LCP data can be leveraged to better detect and measure the multipath. A bank of correlators was applied to the LCP data, centered at the time in the data corresponding to the RCP prompt correlator. With sufficiently wide front-end bandwidth, the resulting LCP code correlation shape would better reveal secondary correlation peaks. For multipath arriving delayed by less than a chip, the LCP code correlation could be used to detect the peak shift due to multipath (as in Figure 8.11),

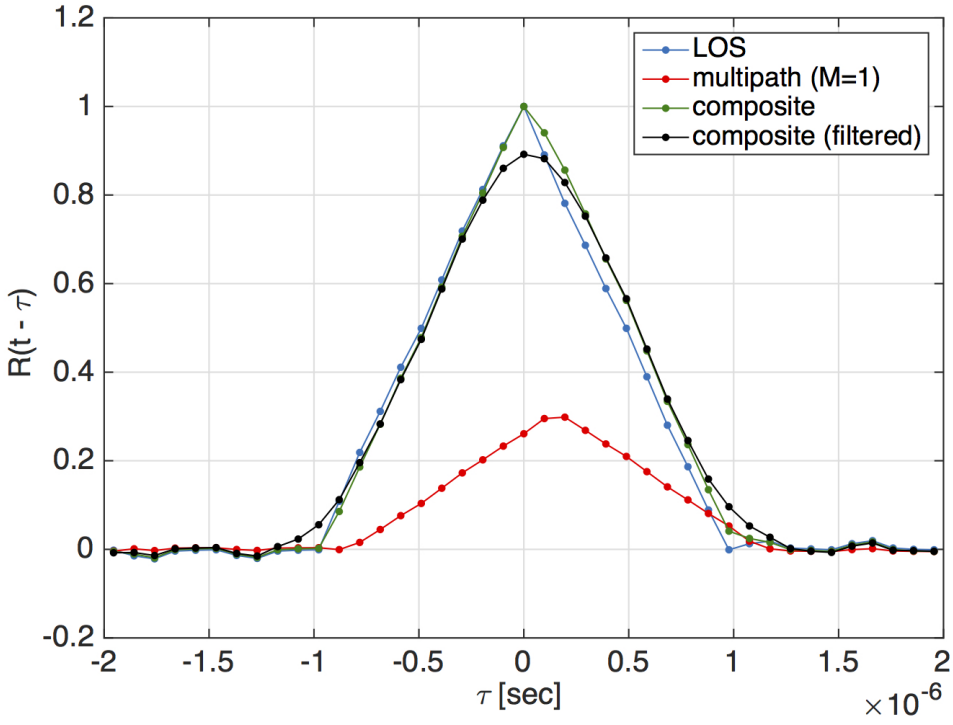

Fig. 8.11. Effect of filtering on code correlation in the presence of a reflected signal

as this shift would be greater in the LCP case than the RCP case. Unfortunately, in the narrowband case of the HSM4 data, this method of open-loop tracking of the LCP data failed to produce reflected signal measurements.

Without good isolation of direct and reflected signals via antenna polarization, or high resolution, wide-band code correlations, the simple direct and reflected range measurement model must be modified. Despite the antenna and bandwidth limitations, the effects of multipath can be observed in the HSM4 tracking results. With a sufficiently detailed model of how these observables arise from the multipath parameters, the observables themselves could be used as inputs to the EKF in order to estimate the target and receiver states from the mix of direct and reflected signals present in both data sets.

The combination of the multipath-corrupted pseudorange in Equation (6.12) and the closed form multipath-induced tracking error in Equation (8.1) is a start:

$$\rho^i = r^i + ct_{b,R} - ct^i_{b,s} + I^i_{L1} + T^i + c\frac{\left(\alpha\frac{G_L}{G_R}\right)^2\delta + \alpha\frac{G_L}{G_R}\delta\cos\psi}{1 + \left(\alpha\frac{G_L}{G_R}\right)^2 + 2\alpha\frac{G_L}{G_R}\cos\psi} + v^i. \tag{8.8}$$

Such an expression relates the measured pseudorange to the multipath relative amplitude, code phase, and carrier phase as well as the antenna cross-pole discrimination. This relies on good knowledge of the antennas and the arriving multipath azimuth and elevation. Furthermore, this is only valid for the case of a single multipath ray and when $\delta < \tau_e + \tau_d$. Despite the difficulties that arise in modeling the relationship between multipath and tracking observables in sufficient detail, this approach has some precedent, as in the batch least squares method pursued by Psiaki et al. in estimating multipath from known antenna motion and a detailed model of complex accumulations [17].

9. CONCLUSIONS

Previous work has focused on detailed measurement modeling not specifically intended for navigation or navigation with assumed measurements. The perspective presented in this dissertation seeks to advance the GNSS bistatic radar technique by considering the problem in its entirety: measurements with consideration of implementation in navigation, and relative navigation with consideration of measurement feasibility.

Forming range measurements from multipath relies first on signal availability, a function of the reflecting object's scattering properties. With solar panels and other highly reflective surfaces, spacecraft are particularly suited to produce strong signal reflections. In the case of HSM4, EM ray tracing confirmed what previous researchers expected: the bistatic RCS of HST scattered numerous strong, sustained reflections in the direction of the GPS receiver during rendezvous and docking.

In processing the RCP and LCP data sets, however, it was found that both contained a mixture of direct and reflected signals. Multipath fading confirmed the presence of reflected signals, and the agreement of these features with the effects of simulated Hubble-reflected signals suggested that the reflected signals were produced by HST.

The concept of relative navigation was demonstrated in simulation: An EKF was used to sequentially estimate the receiver and target states from simulated direct and reflected pseudorange measurements. The feasibility of making reflected pseudorange measurements was shown to be dependent on sufficient reflected signal isolation via antenna polarization. With simulated RCP and LCP antennas, it was shown that with a 20 dB cross-pole discrimination the direct and reflected signals could be separately tracked and the necessary measurements made for receiver and target state estimation.

With poorer cross-pole discrimination, closed-loop tracking of reflected signals fails. This was the case with the HSM4 data, where the LCP flight antenna was measured to have a cross-pole discrimination of less than 10 dB. Under such conditions, the LCP data set was dominated by LOS signals, and reflected signal range measurements could not be made.

In the absence of reflected signal isolation via antenna polarization, open-loop tracking was attempted in which a bank of LCP correlators was used to generate a detailed code correlation centered at the time of the RCP prompt correlator during tracking of the RCP data. Estimation of multipath parameters from deformation of the code correlation shape relies on wide bandwidth, however, and was not possible with the narrow, 2 MHz data collected during HSM4.

Relative navigation with reflected GNSS signals is a promising technique that has generated sustained research interest in applications such as urban navigation and spacecraft proximity operations. The vacuum of space, scattering properties of spacecraft, and well-understood dynamics make spacecraft rendezvous and docking an application with particular potential. The unique use of space data in this dissertation presented an opportunity, but also a challenge. This challenge led to insights regarding measurement feasibility. In order to make reflected pseudorange measurements, an LCP antenna with a cross-pole discrimination much greater than 10 dB must be used. Without two, oppositely polarized antennas with high cross-pole discrimination, measurement of reflected signals relies on the use of a wide front-end bandwidth (e.g., > 10 MHz).

9.1 Future Work

The relative navigation simulation should be improved by using EM ray tracing for the generation of reflected signals rather than an analytic bistatic RCS. This would require increasing the fidelity of the dynamics model to the point that the shuttle and HST trajectories from HSM4 can be used. This would be difficult, due to the shuttle

maneuvers during rendezvous, so it may be more feasible to redo EM ray tracing for the case of the simplified trajectories.

EM ray tracing should be improved by including the effects of the shuttle cargo bay. Although it seems likely that the signals tracked in the LCP data set were strong LOS signals, some of these could be reflections from near the receiver. Processing of the data collected after deploy of HST should be performed to see whether the number of signals tracked in the LCP data changes when Hubble is not present.

Simulated wide-band data should be generated and the MEDLL algorithm implemented. The estimated multipath properties could be checked against the simulated rays and used as inputs to the relative navigation EKF. It would be useful to determine what the minimum necessary band-width is.

Recommendations should be explored as to what can be done with the target spacecraft to support GNSS bistatic radar. Corner reflectors are sometimes used for LIDAR, and something similar may be beneficial when ranging with reflected GNSS signals. A spacecraft may be maneuvered into docking orientation, exposing a face with known or desirable scattering properties. EM ray tracing results from HSM4 suggest that solar panels are a significant source of reflections, so even in the case of a mostly passive target spacecraft it may be worthwhile to orient the solar panels in an optimal manner.

In the course of this dissertation research, preliminary work was done to measure multipath using carrier phase. The shorter wavelength of the L1 carrier provides much higher precision than the code phase measurements used here. Given the small ranges of interest in spacecraft docking, this is an important area for continued work. The technique of measuring multipath using carrier phase is outlined by [73] and was essential in the ranging experiments [11] and [43] mentioned previously, but a method must be employed to resolve carrier phase ambiguity.

Finally, an experiment should be conducted under controlled, static conditions using a large, simple reflecting object, as in the Stockmaster et al. experiment [11]. RCP and LCP antennas with good cross-pole discrimination should be used and,

more importantly, the gain patterns should be well known, including ground plane effects. A wide front-end bandwidth should be used and the resulting data used to validate the conclusions presented in this dissertation.

REFERENCES

REFERENCES

[1] Sung Byun and George Hajj and Lawrence Young, "Development and Application of GPS Signal Multipath Simulator," *Radio Science*, vol. 37, no. 6, pp. 10.1–10.23, November 2002.

[2] Susan Gomez and Shian Hwu, "Comparison of Space Shuttle GPS Flight Data to Geometric Theory of Diffraction Predictions," in *Proceedings of the 10th International Technical Meeting of the Satellite Division of The Institute of Navigation (ION GPS 1997)*, Kansas City, MO, September 1997.

[3] Susan Gomez, "Three Years of Global Positioning Systems Experience on International Space Station," NASA Johnson Space Center, NASA Technical Publication NASA/TP-2006-213168, 2006.

[4] Luke Winternitz and William Bamford, and Gregory Heckler, "A GPS Receiver for High-Altitude Satellite Navigation," *IEEE Journal of Selected Topics in Signal Processing*, vol. 3, no. 4, pp. 541–556, 2009.

[5] Joel Parker and Jennifer Valdez and Frank Bauer and Michael Moreau, "Use and Protection of GPS Sidelobe Signals for Enhanced Navigation and Performance in High Earth Orbit," in *Proceedings of the 39th Annual AAS Guidance and Control Conference.* American Astronautical Society, Feb 2016, pp. 1–13.

[6] Carmelo Carrascosa-Sanz and Pablo Colmenarejo and Emilio Mora-Castro and Guillermo Ortego, "Multipath Effects in GPS Navigation for Rendez-Vous Operations," in *Proceedings of the 4th ESA International Conference on Spacecraft Guidance*, Noordwijk, The Netherlands, October 1999.

[7] D. E. Gaylor and E. G. Lightsey and K. W. Key, "Effects of Multipath and Signal Blockage on GPS Navigation in the Vicinity of the International Space Station (ISS)," *Navigation*, vol. 52, pp. 61–70, 2005.

[8] M. Powe and F. Zanier and M. Porretta and A. Garcia-Rodriguez and O. Mongrard, "Analysis of the International Space Station Multipath and Masking Environment for Automated Transfer Vehicle Relative GPS Rendezvous Manoeuvres," in *2012 6th ESA Workshop on Satellite Navigation Technologies and European Workshop on GNSS Signals and Signal Processing, (NAVITEC).* Institute of Electrical and Electronic Engineers, Dec 2012, pp. 1–7.

[9] Ian Cohen, "Relative Navigation for Hubble Servicing Mission Using Reflected GPS Signals," Master's thesis, University of Maryland, 2007.

[10] Eric Vinande and Dennis Akos and Dallas Masters and Penina Axelrad and Stephan Esterhuizen, "GPS Bistatic Radar Measurements of Aircraft Altitude and Ground Objects with a Software Receiver," in *Proceedings of the 61st Annual Meeting of the Institute of Navigation*, Cambridge, MA, June 2005, pp. 528–534.

[11] Michael Stockmaster and James Tsui and Dennis Akos, "Passive Ranging Using the GPS," in *Proceedings of the 11th International Technical Meeting of the Satellite Division of the Institute of Navigation*, Nashville,TN, September 1998, pp. 915–921.

[12] Pratap Misra and Per Enge, *Global Positioning System*, 2nd ed. Lincoln, MA: Ganga-Jamuna Press, 2005.

[13] Science Applications International Corporation, "IS-GPS-200H," Global Positioning Systems Wing, El Segundo, CA, Tech. Rep., September 2014.

[14] Dilip Sarwate and Michael Pursley, "Crosscorrelation Properties of Pseudorandom and Related Sequences," in *Proceedings of the IEEE*. Institute of Electrical and Electronic Engineers, May 1980, pp. 593–619.

[15] R. Gold, "Optimal binary sequences for spread spectrum multiplexing (corresp.)," *Information Theory, IEEE Transactions on*, vol. 13, no. 4, pp. 619 –621, October 1967.

[16] Nadav Levanon, *Radar Principles*. New York: Wiley, 1988.

[17] Mark Psiaki and Tunc Ertan and Brady O'Hanlon and Steven Powell, "GNSS Multipath Mitigation using Antenna Motion," *Journal of the Institute of Navigation*, vol. 62, no. 1, pp. 1 –22, Spring 2015.

[18] Mark Psiaki and Brady O'Hanlon, "System Identification of a GNSS Receiver's RF Filter Impulse Response Function," *Proceedings of the 24th International Technical Meeting of the Satellite Division of the Institute of Navigation*, pp. 3690–3708, September 2011.

[19] A. J. Van Dierendonck, "GPS Receivers," in *The Global Positioning System: Theory and Applications*, James Spilker and Bradford Parkinson, Ed. Washington, DC: American Institute of Aeronautics and Astronautics, 1996, vol. 1, ch. 8.

[20] James Spilker, "Fundamentals of Signal Tracking Theory," in *The Global Positioning System: Theory and Applications*, James Spilker and Bradford Parkinson, Ed. Washington, DC: American Institute of Aeronautics and Astronautics, 1996, vol. 1, ch. 7.

[21] P. Axelrad and R. G. Brown, "GPS Navigation Algorithms," in *The Global Positioning System: Theory and Applications*, James Spilker and Bradford Parkinson, Ed. Washington, DC: American Institute of Aeronautics and Astronautics, 1996, vol. 1, ch. 9.

[22] Dennis Akos and Per-Ludvig Normark and Jeong-Taek Lee and Konstantin Gromov and James Tsui and John Schmaus, "Low Power Global Navigation Satellite System (GNSS) Signal Detection and Processing," in *Proceedings of the 13th International Technical Meeting of the Satellite Division of the Institute of Navigation*. Salt Lake City, UT: Institute of Navigation, September 2000, pp. 784–791.

[23] Mark Psiaki, "Block Acquisition of Weak GPS Signals in a Software Receiver," *Proceedings of the 14th International Technical Meeting of the Satellite Division of the Institute of Navigation*, pp. 2838–2850, September 2001.

[24] Phillip Ward, "Satellite Signal Acquisition and Tracking," in *Understanding GPS: Principles and Applications*, 1 ed., Elliott Kaplan, Ed. London: Artech House, 1996, ch. 5, pp. 167–172.

[25] Luke Winternitz, "MMS-Navigator Global Positioning System Receiver Algorithm Description Document," National Aeronautics and Space Administration, Tech. Rep. 461-NAV-SPEC-0061 Revision A, September 2012.

[26] K. Borre, D. Akos, and N. Bertelsen, *A Software-Defined GPS and Galileo Receiver: A Single-Frequency Approach*, ser. Applied and Numerical Harmonic Analysis. Birkhauser, 2007.

[27] Mark Bell, "Chapter 2: Electromagnetic Wave Propagation and Antennas," October 2012, Textbook Draft.

[28] Joseph Goodman, *Introduction to Fourier Optics*. Englewood, CO: Roberts & Co., 2005.

[29] S. Cloude, *An Introduction to Electromagnetic Wave Propagation and Antennas*. Springer, 1995.

[30] Joseph Keller, "Geometrical Theory of Diffraction," *Journal of the Optical Society of America*, vol. 52, no. 2, pp. 116–130, 1961.

[31] V. A. Borovikov and B. Ye. Kinber, *Geometrical Theory of Diffraction*. London: The Institute of Electrical Engineers, 1994.

[32] Friis, H.T., "A Note on a Simple Transmission Formula," *Proceedings of the IRE*, vol. 34, no. 5, pp. 254 – 256, May 1946.

[33] Skolnik, Merill I., "An Analysis of Bistatic Radar," *Aerospace and Navigational Electronics, IRE Transactions on*, vol. ANE-8, no. 1, pp. 19 –27, March 1961.

[34] J. Willis, "Bistatic Radar," in *Radar Handbook*, 2nd ed., Merrill Skolnik, Ed. New York, NY: McGraw Hill, 2001, ch. 25.

[35] Sunil Bisnath and Richard Langley, "Pseudorange Multipath Mitigation By Means of Multipath Monitoring and De-Weighting," in *Proceedings of the International Symposium on Kinematic Systems in Geodesy, Geomatics and Navigation*, Banff, Alberta, June 2001, pp. 392–400.

[36] R. D. J. van Nee, "Multipath and multi-transmitter interference in spread-spectrum communication and navigation systems," Ph.D. dissertation, Delft University of Technology, 1995.

[37] Marshall E. Haker and John F. Raquet, "Tracking Multipath in Received GNSS Signals through use of a Signal Decomposition and Parameterization Algorithm," in *Proceedings of the 25th International Technical Meeting of The Satellite Division of the Institute of Navigation (ION GNSS 2012)*, Nashville, TN, September 2012, pp. 151–156.

[38] J. Auber and A. Bibaut and J. Rigal, "Characterization of Multipath on Land and Sea at GPS Frequencies," in *Proceedings of the 7th International Technical Meeting of the Satellite Division of the Institute of Navigation*. Salt Lake City, UT: Institute of Navigation, September 1994.

[39] Stephen Katzberg and James Garrison and Charles Howell, "Simple Over-Water Altimeter Using GPS Reflections," in *Proceedings of the 12th International Technical Meeting of the Satellite Division of the Institute of Navigation*. Nashville, TN: Institute of Navigation, September 1999, pp. 1819–1828.

[40] S. Lowe and C. Zuffada and J. LaBrecque and M. Lough and J. Lerma and L. Young, "An Ocean-Altimetry Measurement Using Reflected GPS Signals Observed From a Low-Altitude Aircraft," in *Proceedings of the IEEE IGARS 2000*. Honolulu, HI: Institute of Electrical and Electronic Engineers, July 2000.

[41] M. Martin-Neira and M. Caparrini and J. Font-Rossello and S. Lannelongue and C. Vallmitjana, "The PARIS Concept: An Experimental Demonstration of Sea Surface Altimetry using GPS Reflected Signals," *IEEE Transactions on Geoscience and Remote Sensing*, vol. 39, no. 1, pp. 142–150, 2001.

[42] D. Masters and P. Axelrad and V. Zavorotny and S. Katzberg and F. Lalezari, "A Passive GPS Bistatic Radar Altimeter for Aircraft Navigation," in *Proceedings of the 14th International Technical Meeting of the Institute of Navigation*. Cambridge, MA: Institute of Navigation, June 2001, pp. 2435–2445.

[43] R. Treuhaft and S. Lowe and C. Zuffada and Y. Chao, "2-cm GPS Altimetry Over Crater Lake," *Geophysical Research Letters*, vol. 22, no. 23, pp. 4343–3446, December 2001.

[44] J. R. Dowdle and D. E. Gustafson and J. John M. Elwell, "Geographical Navigation Using Multipath Wireless Navigation Signals," US Patent 6,693,592, February 2004.

[45] C. M. Lane, "Formation design and relative navigation in high earth orbits," Ph.D. dissertation, University of Colorado, 2007.

[46] Ian Cohen, "Relative Navigation Using Reflected GPS Signals," in *Proceedings of the 2008 National Technical Meeting of The Institute of Navigation*, San Diego, CA, January 2008, pp. 224–230.

[47] Ian Cohen and Gregory Boegner Jr., "Method and Apparatus for Relative Navigation Using Reflected GPS Signals," US Patent 7,817,087, October 2010.

[48] Bo Naasz and John Van Eepoel and Steve Queen and Michael Southward and Joel Hannah, "Flight Results of the HST SM4 Relative Navigation Sensor System," *33rd Annual AAS Guidance and Control Conference*, p. 14, February 2010.

[49] Bo Naasz and Richard Burns and Steve Queen and John Vaneepoel and Joel Hannah and Eugene Skelton, "The HST SM4 Relative Navigation Sensor System Overview and Preliminary Testing Results from the Flight Robotics Lab," *The Journal of the Astronautical Sciences*, vol. 57, no. 1-2, pp. 457–483, 2009.

[50] "High Speed Serial (Pseudo-Space Wire RS644-like)," Goddard Space Flight Center, June 2006, Revision 0.2.

[51] "GPS S67-1575-39/139 Specifications," Sensor Systems Inc.

[52] Navigation Group of the Flight Design and Dynamics Department, "Internal ICD: PATH Product," United Space Alliance Company, ICD-I-TOP-002, April 2007.

[53] ——, "Internal ICD: RELBET Product," United Space Alliance Company, ICD-I-TOP-001, December 2006.

[54] Mission Planning and Analysis Division, "Onboard Navigation Systems Characteristics," Johnson Space Center, JSC-14675, March 1979.

[55] Mission Operations Directorate Flight Design and Dynamics Division, "Rendezvous STS-125/STS-400," Johnson Space Center, JSC-48072-125, September 2008.

[56] Jan Weiss and Penina Axelrad and Steve Anderson, "A GNSS Code Multipath Model for Semi-Urban, Aircraft, and Ship Environments," *NAVIGATION*, vol. 54, no. 4, pp. 294–307, 2007.

[57] AWE Communications, "WinProp Version 12.30," 2012.

[58] J. P. Weiss, "Modeling and characterization of multipath in global navigation satellite system ranging signals," Ph.D. dissertation, University of Colorado, 2007.

[59] Benjamin Ashman and Jeanette Veldman and James Garrison and Penina Axelrad, "Evaluation of the GNSS Multipath Environment in Space Proximity Operations: Experimental and Simulation Studies of Code Correlations in Hubble Servicing Mission 4," in *Proceedings of the ION 2015 Pacific PNT Meeting*. Honolulu,HI: Institute of Navigation, April 2015, pp. 863–871.

[60] Christine Larson and Andria Bilich and Penina Axelrad, "Improving the Precision of High-rate GPS," *Journal of Geophysical Research*, vol. 112, no. B05422, pp. 1–11, 2007.

[61] Jeanette Veldman, "GPS Multipath Study for HSM4," December 2015, ASEN 6091 Final Project.

[62] Benjamin Ashman and James Garrison, "Tracking of Direct and Reflected Global Navigation Satellite System (GNSS) Signals in Hubble Servicing Mission 4," in *Proceedings of the ION 2013 Pacific PNT Meeting*. Honolulu,HI: Institute of Navigation, April 2013, pp. 1117–1124.

[63] Edwin Chong and Stanislaw Żak, *An Introduction to Optimization*. Hoboken, NJ: Wiley-Interscience, 2008.

[64] J. W. Crispin Jr. and R. F. Goodrich and K. M. Siegel, "A Theoretical Method for the Calculation of the Radar Cross Sections of Aircraft and Missiles," The University of Michigan, Tech. Rep. 2591-1-H, July 1959.

[65] S. J. Julier and J. K. Uhlmann, "A New Extension of the Kalman Filter to Nonlinear Systems," in *Proceedings of the SPIE*, vol. 3068, July 1997, pp. 182–193.

[66] M. S. Grewal and A. P. Andrews, *Kalman Filtering: Theory and Practice Using MATLAB*. New York: John Wiley and Sons, 2001.

[67] "Orbit Determination Toolbox (ODTBX) 6.5," http://opensource.gsfc.nasa.gov/projects/ODTBX/, November 2014.

[68] H. D. Curtis, *Orbital Mechanics for Engineering Students*, 3rd ed. Oxford: Butterworth-Heinemann, 2010.

[69] J. Crispin, K. Siegel, and J. Bowman, *Methods of Radar Cross-Section Analysis*. New York: Academic Press, 1968.

[70] James Spilker, "Satellite Constellation and Geometric Dilution of Precision," in *The Global Positioning System: Theory and Applications*, James Spilker and Bradford Parkinson, Ed. Washington, DC: American Institute of Aeronautics and Astronautics, 1996, vol. 1, ch. 5.

[71] Rashmi Shah and Michael Walker and Justin Voo and James Garrison and Phillip Stout and Katie Pekkarinen and Daniel LeJeune, "Study of GPS Reflections and Multipath During Hubble Servicing Mission 4 (STS-125)," in *ION GNSS*, May 2010, pp. 2743 – 2749.

[72] Karen Chiang and Mark Psiaki, "GNSS Signal Tracking Using a Bank of Correlators," in *Proceedings of the 23rd International Technical Meeting of the Satellite Division of the Institute of Navigation*. Portland, OR: Institute of Navigation, September 2010, pp. 3258–3267.

[73] Michael Braasch, "Isolation of GPS Multipath and Receiver Tracking Errors," *NAVIGATION*, vol. 41, no. 4, pp. 415–434, Winter 1994-1995.

[74] Jeffrey Marquart, "Relative Navigation Sensors Technical Memorandum: Post-SM4 Truth Estimation for Pose Performance Evaluation," Goddard Space Flight Center, Tech. Rep. 2007-0012, December 2007.

[75] Buddy Nelson, "Hubble Space Telescope Servicing Mission 4 Media Reference Guide," Lockheed Martin, Tech. Rep., 2002.

[76] Jeffrey Marquart, "Relative Navigation Sensors Technical Memorandum: RNS Camera Alignment," Goddard Space Flight Center, Tech. Rep. 2007-0001_camera_alignment, March 2007.

[77] C. A. Murray, "The transformation of coordinates between the systems of B1950.0 and J2000.0, and the principal galactic axes referred to J2000.0," *Astronomy and Astrophysics*, no. 218, pp. 325–329, 1989.

[78] Mark Bell, "Chapter 3: Radar Cross Section (RCS) and Radar Return," October 2012, Textbook Draft.

[79] Eugene F. Knott and John Shaeffer and Michael Tuley, *Radar Cross Section*. Raleigh: SciTech Publishing, 2004.

[80] "Tangent Lines and Normal Vectors to an Ellipse," http://www.algebra.com/algebra/homework/Quadratic-relations-and-conic-sections/Tangent-lines-to-an-ellipse.lesson, December 2013.

[81] "IEEE Standard Test Procedures for Antennas," Institute of Electrical and Electronic Engineers, 2002, Std 149-1979.

[82] Constantine A. Balanis, *Antenna Theory: Analysis and Design*. Chichester: Wiley, 1997.

APPENDICES

A. CONSTRUCTION OF HST RELATIVE TRAJECTORY TRUTH

A.1 RELBET and GNFIR

United Space Alliance provided an estimate of HST's position and attitude relative to the space shuttle during HSM4, but this relied on the shuttle's on-board rendezvous radar for relative range information [53]. When this system was switched over to wideband communications during docking at 16:37:30 UTC, error increased in the RELBET estimate of HST position, rendering the solution invalid. The error is readily apparent when images from cameras in the shuttle bay are compared to the STK simulation produced with RELBET HST data, as shown in Figure A.1.

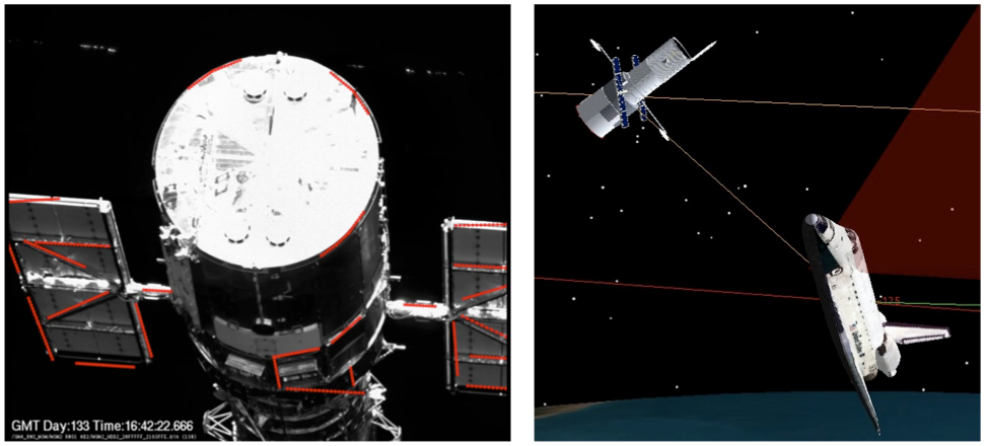

Fig. A.1. Comparison of HST position in RNS camera image (left) and RELBET (right) at 16:42:22 UTC

Three cameras with varying optical ranges were mounted on the Multi-use Logistic Equipment Carrier (MULE), looking up out of the shuttle cargo bay. Using images from these cameras, GNFIR and ULTOR sought to track physical features of HST

and calculate the space telescope's state relative to the shuttle. This relative state, a quantity incorporating position and attitude, is referred to by RNS researchers as "pose."

Noting the "discrepancies between the pose generated from Shuttle and HST position/attitude information, and the pose solutions from the RNS algorithms," researchers used RNS flight imagery to "justify the pose solution from the RNS algorithms as the correct solution" [48]. As a result, the GNFIR post-processed solution is used as a truth for the HST position after the rendezvous radar is turned off at 16:37:30 UTC. However, the RELBET attitude for HST is regarded as a valid truth throughout rendezvous [48].

A.2 Transformation from RNS Camera Frame to J2000.0

The shuttle and HST rendezvous poses from RELBET are available from 10:00:00-20:00:00 UTC on May 13, 2009 in the B1950.0 inertial reference frame. Each of the three RNS cameras recorded imagery during the time frames shown in Table A.1. The GNFIR algorithm only tracked and produced pose estimates for the time frames given in the table's "pose soln." fields. Interpolation must be used to produce a continuous trajectory for HST over the duration of rendezvous and docking. Researchers determined that Hubble was grappled with the Shuttle Remote Manipulator System (SRMS) at 17:13:56 UTC. Note that no pose solutions were produced from RNS camera 3 data prior to grapple, so only the first two RNS cameras will be considered in the following discussion.

The objective here is to construct improved HST position data through a combination of RELBET and GNFIR, so the relative HST position from GNFIR must be transformed from the corresponding RNS camera frame into the J2000.0 inertial frame and added to the RELBET shuttle position. The notation introduced by [74] is used, in which subscripts identify coordinate frames and are in the form 'location-

Table A.1.
Time spans of RNS camera data; pose solutions only available during successful GNFIR tracking (May 13, 2009 UTC)

		start	**end**
RNS 1	data	16:17:57.309	17:07:31.355
	pose soln.	16:21:34.646	16:49:03.673
		17:03:30.686	17:03:31.352
RNS 2	data	16:50:36.683	17:09:22.702
	pose soln.	16:50:48.684	16:51:00.017
		17:06:35.700	17:08:07.035
RNS 3	data	17:49:05.902	17:55:46.572
	pose soln.	- -	- -

origin.' For instance, q_{ba} is the quaternion describing the rotation from frame a to frame b. The coordinate frame abbreviations are shown in Table A.2.

Table A.2.
Coordinate frame subscripts

Abbreviation	**Reference Frame**
b50	B1950.0 inertial frame
2k	J2000.0
sts	shuttle-fixed structure frame
orb	orbiter-fixed body frame
hst	HST-fixed structure frame
cm	HST-fixed body frame
rns	RNS camera frame
stk	HST-fixed body frame in STK

The HST relative position data available from GNFIR is the vector from the corresponding RNS camera frame origin to the HST-fixed structure frame, $\vec{r}_{hstrns}$. The starting frame is *rns*, and the transformations necessary to obtain the desired vector (the HST center of mass expressed in the *2k* frame) are listed below and described in detail in the following sections:

1. Rotation into the shuttle structure frame ($\vec{r}_{hstrns} \rightarrow \vec{r}'_{hstrns}$)
2. Translation of reference origin from RNS camera frame origin to orbiter body frame origin, i.e., the shuttle center of mass ($\vec{r}'_{hstrns} \rightarrow \vec{r}'_{hstorb}$)
3. Rotation into J2000.0 inertial frame ($\vec{r}'_{hstorb} \rightarrow \vec{r}''_{hstorb}$)
4. Translation of reference origin from orbiter body frame origin to J2000.0 inertial frame origin ($\vec{r}''_{hstorb} \rightarrow \vec{r}_{hst2k}$)
5. Translation of reference point on HST from the HST structure frame origin to the HST body frame origin, i.e., the HST center of mass ($\vec{r}_{hst2k} \rightarrow \vec{r}_{cm2k}$)

A.2.1 Rotation Into Shuttle Structure Frame

The HST relative position data available from GNFIR is the vector from the RNS camera frame origin to the HST-fixed structure frame, $\vec{r}_{hstrns}$. The HST-fixed structure frame origin is just below the space telescope's aft-bulkhead and is defined with axes V1, V2 and V3 as shown in Figure A.2. First the HST relative position is rotated so that it is expressed in the shuttle-fixed structure frame,

$$\vec{r}'_{hstrns} = q_{stsrns} \odot \vec{r}_{hstrns}. \tag{A.1}$$

Again following the notation of [74], the prime on the rotated vector is used to indicate it is expressed in an intermediate frame other than the one indicated by the second subscript (e.g., here $\vec{r}'_{hstrns}$ is expressed in the *sts* frame rather than the *rns* frame).

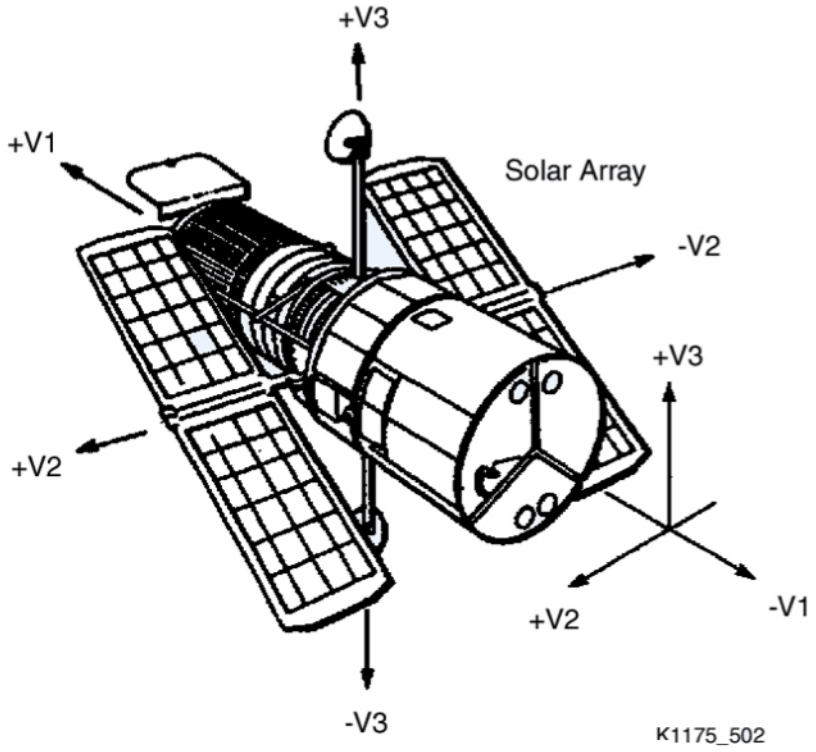

Fig. A.2. Definition of HST-fixed structure frame [75]

A quaternion describes an arbitrary rotation as a rotation by ϕ degrees about a unit vector axis $\vec{e} = \begin{bmatrix} e_1 & e_2 & e_3 \end{bmatrix}^T$. Here the convention is followed where the fourth component is a scalar, so

$$\vec{q} = \begin{bmatrix} q_1 \\ q_2 \\ q_3 \\ q_4 \end{bmatrix} = \begin{bmatrix} e_1 * \sin\frac{\phi}{2} \\ e_2 * \sin\frac{\phi}{2} \\ e_3 * \sin\frac{\phi}{2} \\ \cos\frac{\phi}{2} \end{bmatrix}. \tag{A.2}$$

The $\odot$ operator indicates a rotation by the preceding quaternion from the frame of the quaternion's right subscript into the frame of the quaternion's left subscript. For

a quaternion $\vec{q} = \begin{bmatrix} q_1 & q_2 & q_3 & q_4 \end{bmatrix}^T$, this is implemented via a 3x3 rotation matrix, R(q),

$$R(q) = \left(q_4^2 - \begin{bmatrix} q_1 & q_2 & q_3 \end{bmatrix} \begin{bmatrix} q_1 \\ q_2 \\ q_3 \end{bmatrix} \right) \mathbf{I}_{3x3} + 2 \begin{bmatrix} q_1 \\ q_2 \\ q_3 \end{bmatrix} \begin{bmatrix} q_1 & q_2 & q_3 \end{bmatrix} \tag{A.3}$$

$$- 2q_4 \begin{bmatrix} 0 & -q_3 & q_2 \\ q_3 & 0 & -q_1 \\ -q_2 & q_1 & 0 \end{bmatrix}, \tag{A.4}$$

so that

$$\vec{r}'_{hstrns} = R(q_{stsrns})\vec{r}_{hstrns} \tag{A.5}$$

is equivalent to Equation (A.1).

The rotation matrices from the shuttle structure frame into the RNS camera frames are given in [76]. The resulting quaternion for RNS camera 1 is

$$q_{stsrns1} = \begin{bmatrix} 0.666584362385609 \\ 0.740316935054896 \\ 0.0647693392335613 \\ 0.0583185749923974 \end{bmatrix}, \tag{A.6}$$

and the quaternion for RNS camera 2 is

$$q_{stsrns2} = \begin{bmatrix} 0.648140114229582 \\ 0.732589182849416 \\ 0.155716773064050 \\ 0.137766469069945 \end{bmatrix}. \tag{A.7}$$

A.2.2 Translation to Shuttle Center of Mass

The camera frame origin is

$$\vec{r}_{rns1sts} = \begin{bmatrix} 31.115 & 0.9525 & 11.4935 \end{bmatrix}^T \tag{A.8}$$

for RNS camera 1 and

$$\vec{r}_{rns2sts} = \begin{bmatrix} 31.115 & 1.143 & 11.4935 \end{bmatrix}^T \tag{A.9}$$

for RNS camera 2 in meters with respect to the shuttle-fixed structure frame.

RELBET position data is referenced to the spacecraft center of mass for both HST and the shuttle. The shuttle-fixed structure frame origin is 10.16 meters below the center line of the payload bay and 5.99 meters in front of the nose [74]. The x-axis points from the front of the shuttle toward the back, and the y-axis points out the starboard side. The orbiter-fixed body frame is at the shuttle's center of mass, and is rotated 180° about the y-axis relative to the shuttle-fixed structure frame. Both coordinate frames are shown in Figure A.3. Although the center of mass changed slightly throughout HSM4 as fuel was consumed, the origin of the orbiter-fixed body frame in the shuttle-fixed structure frame was initially

$$\vec{r}_{orbsts} = \begin{bmatrix} 28.263 & 0.0058 & 9.472 \end{bmatrix}^T_{sts} \tag{A.10}$$

in meters [74].

Therefore, the position of the HST-fixed structure frame relative to the shuttle center of mass is

$$\vec{r}'_{hstorb} = \vec{r}'_{hstrns} + \vec{r}_{rnssts} - \vec{r}_{orbsts}, \tag{A.11}$$

where all of the vectors are expressed in the *sts* coordinate frame and $\vec{r}'_{hstrns}$ is from Equation (A.1).

A.2.3 Transformation From Shuttle Structure Frame to J2000.0

The RELBET shuttle attitude is given in the form of quaternions describing the orientation of the orbiter-fixed body frame relative to the B1950.0 inertial reference frame. Although RELBET documentation states that the shuttle attitude is given as a "transformation, Aries mean-of-1950 to body, matrix" (i.e., B1950.0 to orbiter-fixed body frame) [53], comments in RNS researcher's MATLAB scripts indicate the

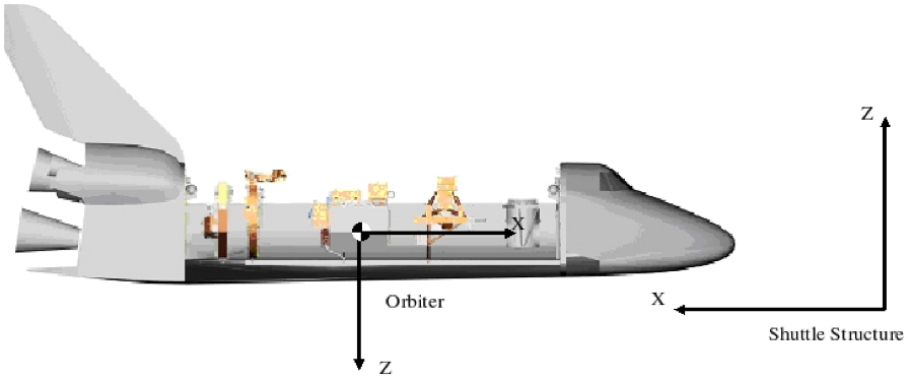

Fig. A.3. Definition of orbiter-fixed body frame and shuttle-fixed structure frame (from slides by C. Eugene Skelton II, published in [74])

RELBET quaternions actually describe the opposite - the orbiter-fixed body frame to B1950.0 transformation. After reversing the transformation order (i.e., negating the non-scalar terms) and transforming this to the J2000.0 frame according to [77], the shuttle attitude from RELBET is $\vec{q}_{sts2k}$. Thus the position of the HST-fixed body frame relative to the shuttle center of mass, expressed in J2000.0 inertial coordinates, is

$$\vec{r}''_{hstorb} = \vec{q}_{2ksts} \odot \vec{r}'_{hstorb}, \tag{A.12}$$

where the double prime is used to indicate the second intermediate frame, J2000.0, $\vec{q}_{2ksts}$ is the reversal of the transformed RELBET shuttle attitude, and $\vec{r}'_{hstorb}$ is from Equation (A.11).

Next, the location of the shuttle center of mass in the J2000.0 frame (obtained by rotating the RELBET position data from B1950.0 to J2000.0) is added to the HST relative position to obtain absolute position of the HST-fixed structure frame in J2000.0:

$$\vec{r}_{hst2k} = \vec{r}''_{hstorb} + \vec{r}_{orb2k}. \tag{A.13}$$

A.2.4 Translation of HST Reference to HST Center of Mass

Finally, in order to be consistent with the RELBET data, the HST position in the J2000.0 coordinate frame must be referenced to the spacecraft's center of mass. The HST center of mass in the HST-fixed structure frame is

$$\vec{r}_{cmhst} = \begin{bmatrix} 6.50 & 0.033 & -0.175 \end{bmatrix}^T_{hst} \tag{A.14}$$

in meters. Therefore the absolute position of HST in the J2000.0 inertial coordinate frame from GNFIR is

$$\vec{r}_{cm2k} = \vec{r}_{hst2k} + \vec{r}_{cmhst}. \tag{A.15}$$

A.3 Spacecraft Attitude

Several adjustments are necessary in order to correctly simulate the attitude of each spacecraft in STK. Although the PATH/RELBET shuttle attitude is valid throughout the servicing mission [48], the provided quaternions actually specify the rotation from the orbiter-fixed body frame to the B1950.0 inertial frame. Therefore, this quaternion must be reversed.

HST is inertially-fixed, so its attitude remains constant throughout the shuttle approach. The initial attitude for HST is

$$\vec{q}_{cm2k} = \begin{bmatrix} -0.0200219210460135 \\ 0.610672122288234 \\ 0.780859403727529 \\ 0.130143280072002 \end{bmatrix}. \tag{A.16}$$

However, the HST body frame in STK is different than the one specified in Figure A.2. The STK frame is obtained through a 180° rotation about the y-axis. For the

axis of rotation $e = \begin{bmatrix} 0 & 1 & 0 \end{bmatrix}^T$ and the angle of rotation $\phi = \pi/2$, the quaternion specifying the rotation from the *cm* frame to the *stk* frame is

$$\vec{q}_{stkcm} = \begin{bmatrix} 0 & \sin(\pi/4) & 0 & \cos(\pi/4) \end{bmatrix}^T \tag{A.17}$$

$$= \begin{bmatrix} 0 & \sqrt{2}/2 & 0 & \sqrt{2}/2 \end{bmatrix}^T. \tag{A.18}$$

Using the resulting rotation matrix, the correct HST attitude to enter into STK can be calculated

$$\vec{q}_{stk2k} = \frac{\sqrt{2}}{2} \begin{bmatrix} 1 & 0 & -1 & 0 \\ 0 & 1 & 0 & 1 \\ 1 & 0 & 1 & 0 \\ 0 & -1 & 0 & 1 \end{bmatrix} \vec{q}_{cm2k} = \begin{bmatrix} -0.566308615673038 \\ 0.523835594616364 \\ 0.537993343385002 \\ -0.339785202886818 \end{bmatrix}. \tag{A.19}$$

A.4 Additional Notes on Accuracy

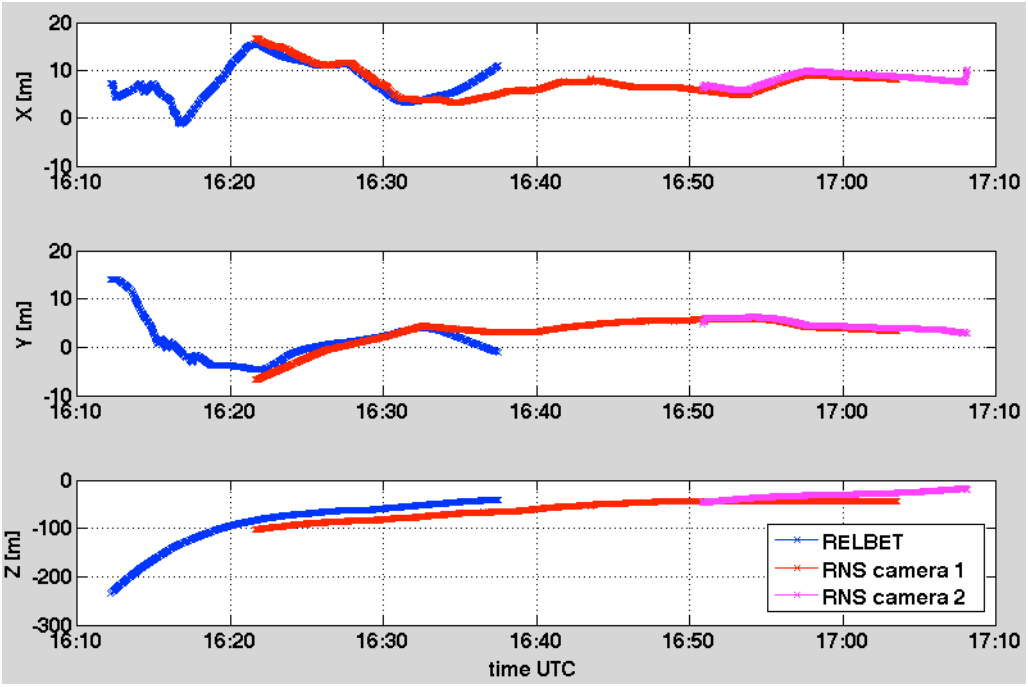

Fig. A.4. HST position in shuttle structure frame according to RELBET and GNFIR from RNS cameras 1 and 2

It is clear from Figure A.4 that the position estimates from each data source do not perfectly align during times of overlap. The differences between each of the HST trajectory estimates are shown in Figure A.5 for these times. In the first case, the deviation of RELBET from GNFIR in the x and y dimensions is within the 3-σ bound of RELBET, with an RMS error of less than 1.5 meters in both cases. Error in the z (or range) dimension is significant, however. This 20 meter RELBET bias was observed in [48] as well, and camera imagery and ULTOR results were used to identify this as an error in RELBET. No further explanation is given, except to note that the rendezvous radar was set to low power at 16:11:25 UTC, which "resulted in increased noise in the radar angles" [48]. In producing a continuous trajectory, then, the GNFIR solution from RNS camera 1 imagery will be used instead of RELBET when it is available. The RELBET bias is particularly evident in the plot of inter-vehicle range in Figure A.6.

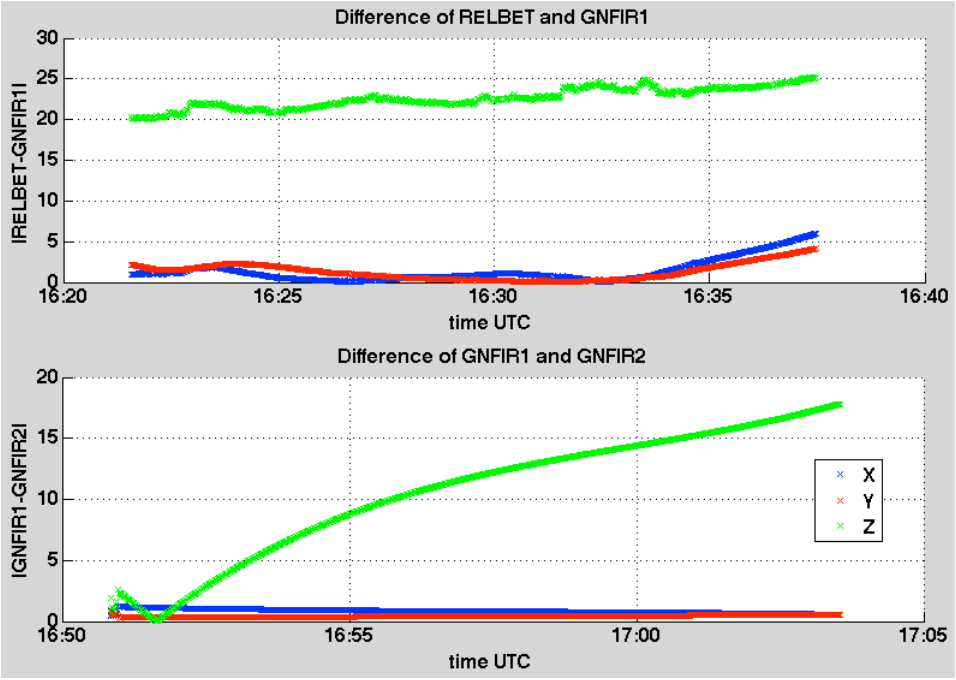

Fig. A.5. Difference between RELBET and GNFIR solutions in regions of overlap

In the second region of overlap, both position estimates are within a meter of one another for the first couple minutes. Even at this point, however, they do not meet the RNS 3-σ accuracy goals. Notice in Table A.1 that neither camera produced trackable images from 16:51:00 to 17:03:30 UTC. In producing a continuous trajectory, however, the results from RNS camera 2 will be used after 16:50:00 UTC, as the camera has a working range of 6 to 40 meters [49]. RNS camera 1 is intended for distances greater than 28 meters, and shuttle-HST range approaches this threshold during the overlap region.

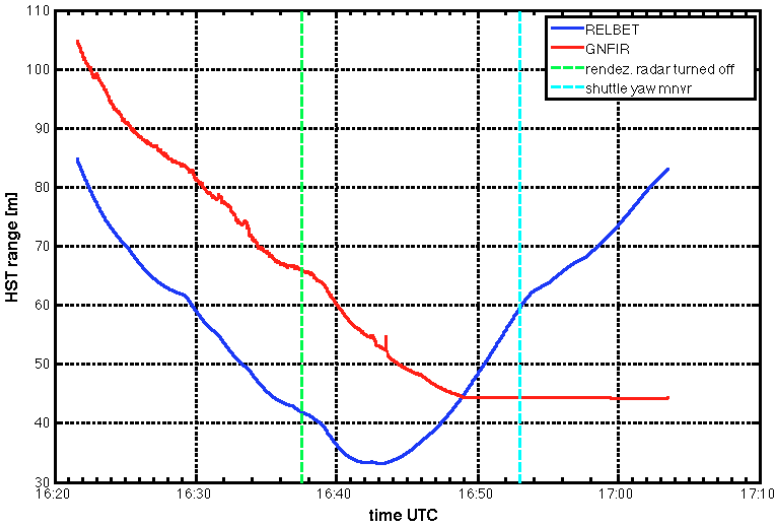

Fig. A.6. Range between shuttle and HST according to RELBET and GNFIR

B. ANALYTIC APPROACH TO CALCULATING THE HUBBLE BISTATIC RCS

B.1 Radar Cross Section

The RCS, σ, is a term independent of the receiver and transmitter systems that describes the target's ability to re-radiate an incident power density. It is dependent on target material, target absolute size, target size relative to λ, incident and reflected angles and the transmitter and receiver polarizations with respect to the target. The quantity itself is theoretically the cross-sectional area of a perfectly reflecting sphere that would produce the same strength reflection as the target object [78].

An accurate radar cross section of HST at L band frequencies is complicated. In addition to the complicated electrical properties of the space telescope and its moving solar panels, the spacecraft involved are rapidly changing position and orientation with respect to one another. A full solution is only possible using numerical electromagnetic simulation software.

A simplified analytic solution may be possible, however, using combinations of simple shapes. First the RCS of a perfectly conducting sphere is examined. Due to the symmetric nature of the sphere, this RCS can be generalized across all satellites and geometries, so that the received power varies only with range terms. A perfectly conducting cylinder is considered next. This is more accurate, in that it is highly dependent on the orientation of the target relative to the transmitter and receiver. Therefore, the cylinder RCS is considered here for the particular case of the satellite transmitting pseudo-random noise code 9 (PRN 9).

From [79], RCS is defined in general to be

$$\sqrt{\sigma} = \lim_{R\to\infty} 2\sqrt{\pi}R\frac{\vec{E}_s \cdot \hat{e}_r}{E_i}e^{ikR}, \tag{B.1}$$

where the scattered electric field can be written

$$\vec{E}_s = -jk\eta \int_s \left(\vec{J}\psi - \frac{1}{k^2}\Delta \cdot \vec{J}\Delta\psi \right) ds \tag{B.2}$$

for a perfect conductor, where ψ is the free-space Green's function $\psi = e^{-i\vec{k}\cdot\vec{R}_{fs}}/(4\pi\vec{R}_{fs})$. This is the sum of the surface integral over the scattering object surface for fields caused by external sources and the volume integral over the scattering object for fields caused by internal sources.

When the target dimensions are much larger than the incident field wavelength, the the- ory of physical optics can be applied. Assuming the receiver is in the far field with respect to the scatterer, the gradient of the Green's function can be approximated $\Delta\psi \approx ik\hat{s}\psi$ and there will be no surface field distribution component along the scattering direction. Finally, by making the tangent plane approximation (i.e. assigning surface fields values they would have if the body were smooth and flat at ds) we arrive at the physical optics integral:

$$\vec{E}_s = -i2kZ_0H_0\psi_0 \int_S \hat{s} \times [\hat{s} \times (\hat{n} \times h_i)]\, e^{ik\vec{r}\cdot(\hat{i}-\hat{s})}\, ds, \tag{B.3}$$

where S is the illuminated portion of the body [79].

Substituting this scattered electric field expression into the general radar cross section in (B.1) to obtain the physical optics approximation for the square root of the RCS that we must solve:

$$\sqrt{\sigma} = -i\frac{k}{\sqrt{\pi}} \int_S \hat{n} \cdot \hat{e}_r \times \hat{h}_i e^{ik\vec{r}\cdot(\hat{i}-\hat{s})}\, ds. \tag{B.4}$$

B.1.1 Sphere Model

In a report on experiments at the University of Michigan Radiation Laboratory, Crispin *et al.* present a Physical Optics approximation of the radar cross section of a sphere

$$\frac{\sigma(\beta)}{\pi a^2} = (2ka)^2 \left| \int_0^{2\pi} sin(\alpha)cos(\alpha)J_0(kasin(\beta)sin(\alpha))e^{ika(1+cos(\beta)cose(\alpha)}d\alpha \right|^2, \tag{B.5}$$

where a is the sphere radius, β is the angular separation of the incident and reflected directions, k is the wave number and J_0 is the Bessel function of the first kind, 0th order [64]. In the monostatic case $\beta = 0$, so this simplifies to

$$\frac{\sigma(0)}{\pi a^2} = 1 - \frac{sin(2ka)}{ka} + \frac{1 - cos(2ka)}{(ka)^2}. \tag{B.6}$$

The full-wave solution presented by Crispin *et al.* is proportional to the scattering object volume, so a is chosen to generate a sphere of the same volume as HST. On average, the bistatic radar cross section and monostatic radar cross section will vary over comparable values [33], so the result from equation (B.6) can be used for the bistatic RCS in determining an approximate loss in reflected signal power with respect to the direct signal, if not for determining the actual loss at a particular configuration.

The wave number, k, is equal to $\frac{\omega}{c}\mu_r\epsilon_r$, where μ_r and ϵ_r are the magnetic permeability and electric permittivity of the transmission medium, respectively. Both are equal to 1.0 in this case, because transmission is through the vacuum of space. The angular frequency, ω, is $2\pi \times 1.57542$ MHz for GPS and c is the speed of light ($299,792,458$ m/s). Substituting the above values into equation (B.6), with $a = 7.6$ meters, produces a radar cross section of 181.97 m^2.

B.1.2 Cylinder Model

For a cylinder, the general RCS in Equation (B.1) can be written

$$\sqrt{\sigma_{cyl}} = -i\frac{ka}{\sqrt{\pi}} I_z I_\phi e^{ik\vec{r}_0 \cdot (\hat{i} - \hat{s})} \tag{B.7}$$

in cylindrical coordinates (i.e., $ds = ad\phi dz$, and $\vec{r} = \vec{r}_0 + z\hat{z} + a\hat{n}$). The axial integral for a cylinder with length l is

$$I_z = \int_{-l/2}^{l/2} e^{ikz\hat{z}\cdot(\hat{i}-\hat{s})}\, dz = l\frac{\sin\left[(1/2)kl\hat{z}\cdot(\hat{i}-\hat{s})\right]}{(1/2)kl\hat{z}\cdot(\hat{i}-\hat{s})}, \tag{B.8}$$

while the circumferential integral is

$$I_\phi = \int_{-\pi/2}^{\pi/2} \hat{n}\cdot\hat{e}_r \times \hat{h}_i e^{ika\hat{n}\cdot(\hat{i}-\hat{s})}\, d\phi. \tag{B.9}$$

The second integral is not easily solved, however, because the limits of integration are not symmetrically disposed with respect to the specular line along the side of the cylinder [79]. The specular line is located such that a surface normal erected on it bisects the projections of the incident and scattering angles on a plane perpendicular to the cylinder axis. This means ϕ is only from $-\pi/2$ to $\pi/2$ in the case where the $\hat{i}$, $\hat{s}$ plane is the same as the $\hat{i}$, $\hat{z}$ plane.

Note that the phase of the integrand varies sinusoidally, the real and imaginary parts essentially canceling over time. The dominant contribution to this integral will be when this variation stops. Using the method of secondary phase, this is found to be at the specular line [79], so

$$I_\phi \approx \hat{n}_0 \cdot \hat{e}_r \times \hat{h}_i e^{ika\hat{n}_0\cdot(\hat{i}-\hat{s})} \left[\frac{a}{\lambda}\hat{n}_0 \cdot (\hat{i}-\hat{s})\right]^{1/2}. \tag{B.10}$$

Substituting I_z and I_ϕ into the expression for $\sqrt{\sigma_{cal}}$ leads to

$$\sqrt{\sigma_{cyl}} = -il\left[\frac{2ka}{\hat{n}_0\cdot(\hat{i}-\hat{s})}\right]^{1/2} \frac{\sin[(1/2)kl\hat{z}\cdot(\hat{i}-\hat{s})]}{(1/2)kl\hat{z}\cdot(\hat{i}-\hat{s})}(\hat{n}_0\cdot\hat{e}_r\times\hat{h}_i)e^{ik\vec{r}_0\cdot(\hat{i}-\hat{s})}e^{ika\hat{n}\cdot(\hat{i}-\hat{s})}e^{-i\pi/4}. \tag{B.11}$$

Taking the magnitude-squared, phase terms are eliminated to arrive at our working formula for the bistatic RCS for a perfectly conducting cylinder,

$$\sigma_{cyl} = \frac{l^2 2ka}{\hat{n}_0\cdot(\hat{i}-\hat{s})}\left|\frac{\sin((1/2)kl\hat{z}\cdot(\hat{i}-\hat{s}))}{(1/2)kl\hat{z}\cdot(\hat{i}-\hat{s})}\right|^2 (\hat{n}_0\cdot\hat{e}_r\times\hat{h}_i)^2. \tag{B.12}$$

The cylinder dimensions of length and radius are given by l and a respectively (HST has a length of 13.2 meters and a radius of 2.1 meters), and $\hat{z}$ is the unit vector in the direction of the cylinder's axis of symmetry. The unit vectors $\hat{n}_0$, $\hat{i}$, and $\hat{s}$ indicate the direction of the cylinder surface normal at the point of reflection, the incident ray and the scattered ray, while $\hat{e}_r$ and $\hat{h}_i$ are the reflected electric field and incident magnetic field unit vectors.

Hypothesis

The transmitting GPS satellite, at approximately 20,000 km, is in the far field with respect to HST. As a result, the infinite number of rays that make up the incident

field are regarded as parallel. The receiver in the shuttle payload bay, however, is at most two hundred meters from HST during the mission times of interest. Rays that make up the scattered field are not treated as parallel, but rather as emanating from a specular point on the hull of the space telescope.

The specular point is defined in a manner similar to the specular line described in Section B.1.2, but for a receiver in the near field the specular reflection is limited to a single point. This is the point on the ellipse formed by the intersection of the scatter plane and HST (see Figure B.1) where the incident and scattered angles are equal. The scatter plane is the plane formed by the line-of-sight (LOS) vectors from HST to the transmitter and receiver. The following sections describe the computation of $\hat{n}_0$, $\hat{i}$, $\hat{s}$, $\hat{e}_r$ and $\hat{h}_i$ from the HST-to-shuttle and HST-to-GPS satellite LOS vectors and any assumptions made in the process. The LOS vectors are obtained through a Satellite Tool Kit (STK) simulation of HSM4 using mission ephemeris and attitude data [53] [52].

The left-hand circularly polarized (LHCP) antenna in the shuttle payload bay will experience an electric field due to many reflections from all parts of HST and the antenna's immediate environment in the shuttle. However, it is assumed that the specular reflection from HST will be the dominant HST-reflected contributor to the received electric field, and the most useful component for processing and determining relative range information.

Ellipse

The strategy for finding the specular point is to compute the ellipse dimensions that arise from the LOS vectors, then search along the ellipse for the point where the incident and scattering angles are equal. The scatter plane is defined as perpendicular to $\hat{n}_p = \hat{i}_{LOS} \times \hat{s}_{LOS}$, where $\hat{i}_{LOS}$ and $\hat{s}_{LOS}$ are the unit line-of-sight vectors from HST to the transmitter and receiver respectively. If $\hat{z}$ is the cylinder axis, and $\hat{n}_p$ is the scatter plane normal, then the ellipse's semi-minor axis is perpendicular to both:

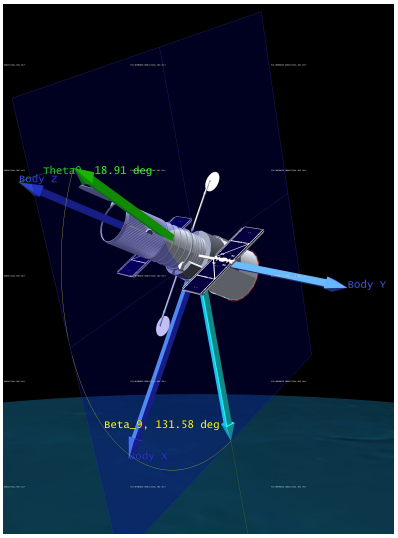

Fig. B.1. Intersection of scatter plane and HST (green arrow points to PRN 9, light blue to the shuttle)

$\hat{b} = \hat{z} \times \hat{n}_p$. The semi-major axis, in turn, is perpendicular to the scatter plane normal and the semi-minor axis, $\hat{a} = \hat{n}_p \times \hat{b}$.

The magnitudes of the ellipse axes can be determined by considering that their projections onto the x-y plane (of the HST body frame) must equal the cylinder radius. The inclination of $\hat{a}$ above the x-y plane is $\alpha = \cos^{-1}(\sqrt{\hat{a}_1^2 + \hat{a}_2^2}^2)$, where $\hat{a}_1$ and $\hat{a}_2$ are the x and y components of the semi-major axis unit vector respectively. Denoting the cylinder radius as r_1, the magnitude of the semi-major axis is $||\vec{a}|| = r_1/\cos\alpha$. The semi-major axis, in the HST body frame, is

$$\vec{a} = \frac{r_1}{\cos\alpha}(\hat{n}_p \times \hat{b}). \tag{B.13}$$

The semi-minor axis is found in a similar manner, for inclination β above the x-y plane, to be

$$\vec{b} = \frac{r_1}{\cos\beta}(\hat{z} \times \hat{n}_p). \tag{B.14}$$

The search for a specular point proceeds in the ellipse reference frame, where the x axis is the semi-major axis, the y axis the semi-minor axis, and the z axis n_p. Denoting the x, y, and z unit vectors as $\hat{a}_1$, $\hat{a}_2$ and $\hat{a}_3$ for the HST body frame, and

$\hat{b}_1$, $\hat{b}_2$, and $\hat{b}_3$ for the ellipse frame, the transformation from a vector $[x, y, z]$ in the ellipse frame to a vector $[x', y', z']$ in the HST body frame is given by the direction cosine matrix $\mathbf{R}$ so that

$$\begin{bmatrix} x' \\ y' \\ z' \end{bmatrix} = \begin{bmatrix} \hat{a}_1 \cdot \hat{b}_1 & \hat{a}_1 \cdot \hat{b}_2 & \hat{a}_1 \cdot \hat{b}_3 \\ \hat{a}_2 \cdot \hat{b}_1 & \hat{a}_2 \cdot \hat{b}_2 & \hat{a}_2 \cdot \hat{b}_3 \\ \hat{a}_3 \cdot \hat{b}_1 & \hat{a}_3 \cdot \hat{b}_2 & \hat{a}_3 \cdot \hat{b}_3 \end{bmatrix} \begin{bmatrix} x \\ y \\ z \end{bmatrix} = \mathbf{R} \begin{bmatrix} x \\ y \\ z \end{bmatrix}. \tag{B.15}$$

The coordinate frame is indicated by a preceding superscript, so for example, a vector $\vec{v}$ defined in the ellipse frame and transformed into the HST body frame is written ${}^a\vec{v} = \mathbf{R}{}^b\vec{v}$.

Having defined the ellipse axes, the LOS vectors can be described in the ellipse frame. It is convenient to define θ_1 as the angle between ${}^b\vec{i}_{LOS}$ and the semi-major axis, and θ_2 as the angle between ${}^b\vec{s}_{LOS}$ and the semi-major axis. A search is then performed along the angle between ${}^b\vec{i}_{LOS}$ and ${}^b\vec{s}_{LOS}$ (the bistatic angle β in radar literature [34]), parameterized by the angle θ_p between the search point p and the semi-major axis. An example is shown in Figure B.2.

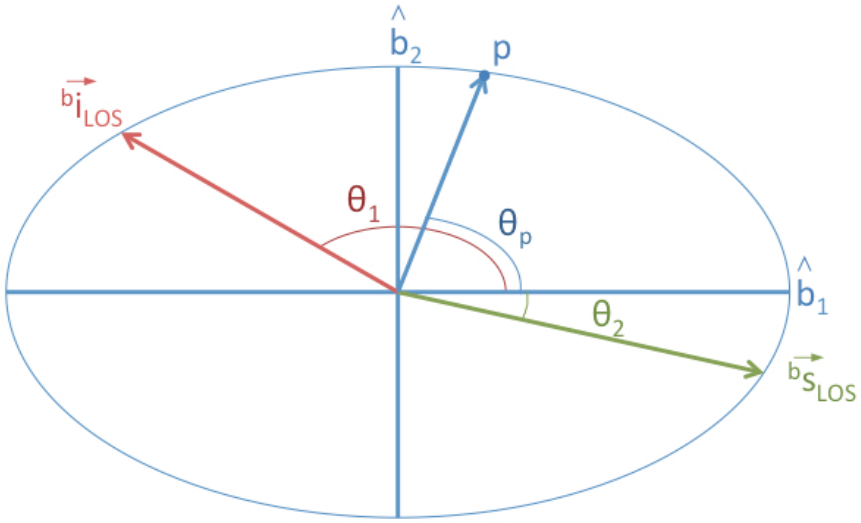

Fig. B.2. Vectors in the ellipse frame involved in the specular point search

Incident and Scatter Unit Vectors

The incident and scatter unit vectors, ${}^{b}\hat{i}$ and ${}^{b}\hat{s}$, are found at each search point. Because the transmitter is in the far field, incident rays are all parallel. Thus, at each point,

$$ {}^{b}\hat{i} = {}^{b}\,\hat{i}_{LOS}. \tag{B.16}$$

The receiver is not in the far field, however, so ${}^{b}\hat{s}$ changes slightly at each p to point at the receive antenna's geometric center.

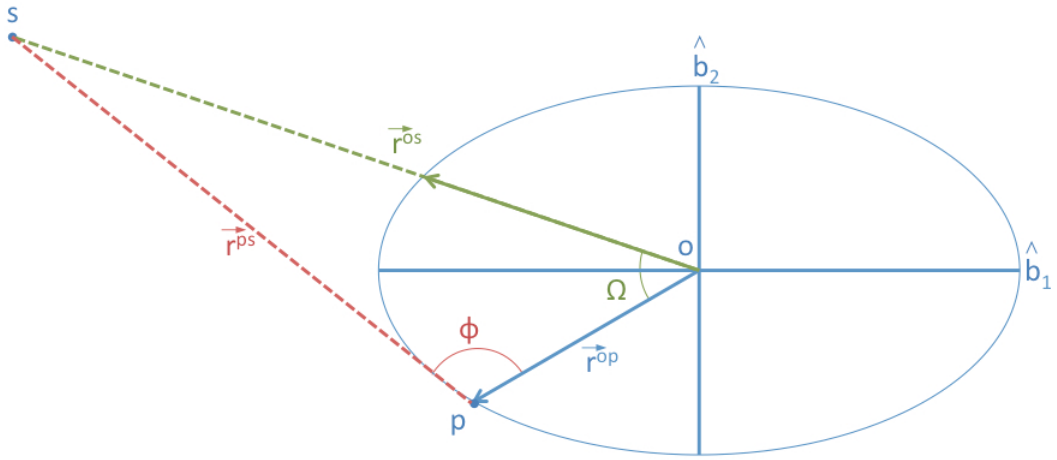

Fig. B.3. Calculation of scatter ray unit vector $\hat{s}$ at candidate specular point p

The orientation of ${}^{b}\hat{s}$ is determined using the law of cosines and the geometry shown in Figure B.3. Here, point s is the receiver on the space shuttle, point p is the candidate specular point, and point o is the origin of the ellipse frame (the cylinder z axis). The objective is to find ${}^{b}\hat{s} = \vec{r}^{ps}/||\vec{r}^{ps}|| = \hat{r}^{ps}$ in the ellipse frame. The convention of indicating normalized vectors with a hat is used throughout this

report. The vector $\hat{r}^{ps}$ can be calculated by first defining a coordinate frame at point p oriented so that $\hat{c}_1 = \hat{r}^{op}$:

$$\begin{aligned}\hat{c}_1 &= \cos(\theta_p)\hat{b}_1 + \sin(\theta_p)\hat{b}_2 \\ \hat{c}_2 &= -\sin(\theta_p)\hat{b}_1 + \cos(\theta_p)\hat{b}_2 \\ \hat{c}_3 &= \hat{b}_3.\end{aligned}$$

After finding $\hat{r}^{ps}$ in this frame it can be transformed into the ellipse frame.

Using the notation in Figure B.3, it is first determined that $\Omega = \cos^{-1}(\hat{r}^{op} \cdot \hat{r}^{os})$. From the law of cosines,

$$||\vec{r}^{ps}|| = \sqrt{||\vec{r}^{op}||^2 + ||\vec{r}^{os}||^2 - 2||\vec{r}^{op}||||\vec{r}^{os}|| \cos(\Omega)}. \tag{B.17}$$

Here, $||\vec{r}^{os}||$ is simply the HST-shuttle range from the STK simulation. To find $||\vec{r}^{op}||$, consider the equation of an ellipse with semi-major and semi-minor axes a and b centered at the origin of an x-y cartesian coordinate system,

$$\frac{x^2}{a^2} + \frac{y^2}{b^2} = 1. \tag{B.18}$$

A line extending radially from the ellipse center, parameterized by its angle, θ, with the x axis, will have the equation

$$y = \tan(\theta)x. \tag{B.19}$$

Substituting this into Equation (B.18), the intersection of the line and ellipse is

$$[x^*, y^*]^T = \left[\frac{ab}{\sqrt{b^2 + a^2 + \tan^2(\theta)}}, \frac{ab\tan(\theta)}{\sqrt{b^2 + a^2\tan^2(\theta)}}\right]^T. \tag{B.20}$$

Thus, the magnitude of $\vec{r}^{op}$ is the magnitude of the vector from the origin to this point of intersection, with the previously defined angle θ_p substituted for θ:

$$||\vec{r}^{op}|| = \frac{ab}{\cos(\theta)\sqrt{b^2 + a^2\tan^2(\theta)}}. \tag{B.21}$$

The axes a and b are the magnitudes of $\vec{a}$ and $\vec{b}$ in Equations (B.13) and (B.14).

From the law of cosines,

$$\phi = \cos^{-1}\left(\frac{||\vec{r}^{ps}||^2 + ||\vec{r}^{op}||^2 - ||\vec{r}^{os}||^2}{2||\vec{r}^{ps}||||\vec{r}^{op}||}\right). \tag{B.22}$$

Finally, using the relationship between the coordinate frame rotating with θ_p and the ellipse frame,

$${}^b\hat{s} = \hat{r}^{ps} = \begin{bmatrix} -\cos(\phi)\cos(\theta_p) - \sin(\phi)\sin(\theta_p) \\ -\cos(\phi)\sin(\theta_p) + \sin(\phi)\cos(\theta_p) \\ 0 \end{bmatrix}. \tag{B.23}$$

Incident and Scatter Angles

The specular point is that point on the ellipse where the incident and scatter angles are equal. These are the angles the incident and scatter unit vectors make with a line tangent to the ellipse at the reflecting point. To find the tangent line at a point, consider again the equation for the ellipse centered at zero with semi-major axis a and semi-minor axis b,

$$\frac{x^2}{a^2} + \frac{y^2}{b^2} = 1. \tag{B.24}$$

From [80], the line

$$\frac{xx_0}{a^2} + \frac{yy_0}{b^2} = 1 \tag{B.25}$$

is tangent to the ellipse at $[x_0, y_0]^T$. It is evident that the line intersects the ellipse at this point, as substituting $[x_0, y_0]^T$ into Equation (B.25) satisfies Equation (B.24). Furthermore, it can be shown that this is the only point of intersection. Rearranging Equation (B.25) for y,

$$y = \frac{(1 - xx_0/a^2)b^2}{y_0}.$$

Substituting this into the formula for the ellipse,

$$\frac{x^2}{a^2} + \frac{(1 - xx_0/a^2)b^4}{b^2y_0^2} = 1 \rightarrow x^2a^2 + \frac{b^2}{y_0^2}(a^4 - 2xx_0a^2 + x^2x_0^2) = a^4$$
$$\rightarrow (a^2y_0^2 + b^2x_0^2)x^2 + (-2b^2x_0a^2)x + (b^2a^4 - y_0^2a^4) = 0.$$

In finding the roots to this equation, the discriminant is

$$d = 4b^4x_0^2a^4 - 4(a^2y_0^2 + b^2x_0^2)(b^2a^4 - y_0^2a^4),$$

but from Equation (B.24) $a^2y_0^2 + b^2x_0^2 = a^2b^2$ and $b^2a^4 - y_0^2a^4 = a^2b^2x_0^2$, leading to

$$d = 4b^4x_0^2a^4 - 4b^4x_0^2a^4 = 0.$$

Thus, only one root exists, so only one point is common to the ellipse and line.

In order to determine the vector expression for the tangent line, consider that the line

$$\frac{xx_0}{a^2} + \frac{yy_0}{b^2} = 0$$

is parallel to that in Equation (B.25). By inspection, the vector $[x_0/a^2, y_0/b^2]^T$ is perpendicular to this line (its inner product with $[x, y]^T$ is zero). Note that this vector is the cylinder unit normal, $\hat{n}_0$, used in Equation (B.12). The vector normal to $\hat{n}_0$, and thus the vector expression of the tangent line itself, is

$$\vec{T} = \left[\frac{-y_0}{b^2}, \frac{x_0}{a^2}\right]^T. \tag{B.26}$$

The incident and scatter angles, θ_i and θ_s, are therefore the angles between $\hat{i}$ and $\hat{s}$ and the tangent line $\vec{T}$. Some care must be taken to ensure that the angle measured is the smallest angle referenced from the outer side of the tangent line (the side opposite the ellipse center).

Ideally, the specular point search is stopped when $\theta_i = \theta_s$. The search algorithm is similar to a golden section search, except that step sizes are not chosen according to golden sections: The search begins at a point halfway between ${}^b\vec{i}_{LOS}$ and ${}^b\vec{s}_{LOS}$, where $\theta_i[0]$ and $\theta_s[0]$ are calculated. The next test point is halfway between the initial point and the search limit in the direction of the smaller angle. For instance, if at $p[0]$, $\theta_i < \theta_s$, then $p[1]$ will be at the point on the ellipse halfway between $\vec{r}^{op}[0]$ and the vector ${}^b\vec{i}_{LOS}$. The new search limits will be ${}^b\vec{i}_{LOS}$ and $\vec{r}^{op}[0]$. The following test point will be halfway between $\vec{r}^{op}[1]$ and the new search limit in the direction of the smallest angle. This continues until $\theta_s[k+1] - \theta_s[k] < \delta$ for some threshold δ, and the

point p at this iteration is the specular point used in calculating σ_{cyl}. This algorithm is not optimal, but greatly reduces the number of steps necessary to achieve a precise solution over an exhaustive search. For $\delta = 0.001$, about ten steps are required.

Electric and Magnetic Field Unit Vectors

The last components needed for calculating σ_{cal} via Equation (B.12) are the reflected electric field and incident magnetic field unit vectors, $\hat{e}_r$ and $\hat{h}_i$. The plane wave solution at point $\vec{r}$ and time t for an electromagnetic wave traveling in the z direction is

$$\vec{E}(\vec{r},t) = \begin{bmatrix} E_x^0 \cos(kz - \omega t + \alpha_x) \\ E_y^0 \cos(kz - \omega t + \alpha_y) \\ 0 \end{bmatrix} \tag{B.27}$$

where E_x^0 and E_y^0 are the magnitudes of the x and y electric field components, respectively, and α_x and α_y indicate the phases of these field components at the initial time reference $t = 0$. The variable z is the spatial position of the plane wave along the direction of propagation. The electric field can equivalently be written

$$\vec{E}(\vec{r},t) = |\vec{E}|\mathrm{Re}\{\mathbf{Q}\,|\psi\rangle\, e^{i(kz-\omega t)}\}. \tag{B.28}$$

The magnitude of the field is given by $|\vec{E}|$ and is related to E_x^0 and E_y^0 according to $|\vec{E}|^2 \equiv (E_x^0)^2 + (E_y^0)^2$. The columns of matrix $\mathbf{Q}$ are the orthogonal vectors spanning the x-y plane and $|\psi\rangle$ is the Jones vector describing the field polarization.

The reference time $t = 0$ is arbitrary, so this can be selected so that the spatial displacement relative to the coordinate system origin is zero, i.e., $z = 0$. Considering the field in a coordinate frame such that the x-y plane is perpendicular to the direction of propagation,

$$\mathbf{Q} = \begin{bmatrix} 1 & 0 \\ 0 & 1 \\ 0 & 0 \end{bmatrix} \tag{B.29}$$

and so

$$\vec{E}(t) = |\vec{E}|\mathrm{Re}\{|\phi\rangle\, e^{-i\omega t}\}. \tag{B.30}$$

The direct signal from a GPS signal is right-hand circularly polarized (RHCP). Following the convention adopted by the Institute of Electrical and Electronic Engineers (IEEE) [81], the Jones vector for RHCP is

$$|\phi\rangle_{RHCP} = \frac{1}{\sqrt{2}} \begin{bmatrix} 1 \\ i \end{bmatrix}. \tag{B.31}$$

A Jones vector represents the relative amplitude and phase of $\vec{E}$ in the x and y directions. It is important to note that conventions differ, however, and the convention used here is the opposite of that often used in optics. When the GPS signal reflects off the conducting surface of HST, the polarity is reversed. The LHCP Jones vector is

$$|\phi\rangle_{LHCP} = \frac{1}{\sqrt{2}} \begin{bmatrix} 1 \\ -i \end{bmatrix}. \tag{B.32}$$

Thus, for a signal traveling in the z direction, the RHCP and LHCP unit vectors can be written

$$\vec{E}_{RHCP}(t) = \begin{bmatrix} \cos(\omega t) \\ \sin(\omega t) \end{bmatrix} \tag{B.33}$$

$$\vec{E}_{LHCP}(t) = \begin{bmatrix} \cos(\omega t) \\ -\sin(\omega t) \end{bmatrix}, \tag{B.34}$$

as in [82].

Both the electric field and magnetic field are oriented perpendicular to the direction of propagation and are orthogonal to one another. Lacking any further constraints beyond these and Equation (B.33), it is assumed that the $\vec{E}$ and $\vec{H}$ field vectors are oriented as shown in Figure B.4.

The incident and scatter directions of propagation have been determined in the ellipse frame according to Equations (B.16) and (B.23). Consider an incident signal coordinate frame, d, at the point of specular reflection such that the z axis points

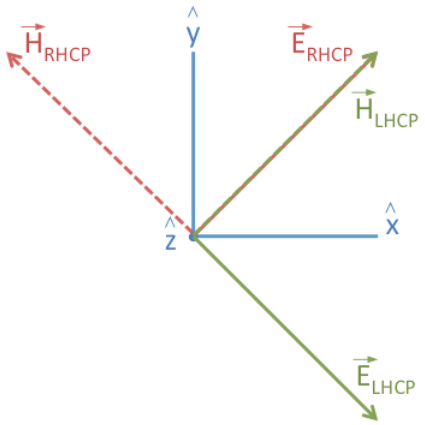

Fig. B.4. Orientation of electric and magnetic field vectors for a signal propagating out of the page

along the direction of incident signal propagation, i.e., $\hat{d}_3 = -\hat{i}$. In terms of the ellipse frame, this incident signal coordinate frame is:

$$\begin{aligned}\hat{d}_1 &= \sin(\theta_1)\hat{b}_1 - \cos(\theta_1)\hat{b}_2 \\ \hat{d}_2 &= \hat{b}_3 \\ \hat{d}_3 &= -\cos(\theta_1)\hat{b}_1 - \sin(\theta_1)\hat{b}_2,\end{aligned}$$

where θ_1, as previously defined, is the angle between ${}^b\vec{i}_{LOS}$ and the ellipse's semi-major axis. In this frame, the RHCP electric field follows simply from Equation (B.33):

$${}^d\vec{E}_i(t) = |\vec{E}|\left(\cos(\omega t)\hat{d}_1 + \sin(\omega t)\hat{d}_2\right).$$

From the $\vec{E}$ and $\vec{H}$ field relationship in Figure B.4,

$${}^d\vec{H}_i(t) = |\vec{H}|\left(-\sin(\omega t)\hat{d}_1 + \cos(\omega t)\hat{d}_2\right).$$

This leads to the incident RHCP magnetic field vector in the ellipse frame,

$${}^b\vec{H}_i(t) = |\vec{H}|\left(-\sin(\omega t)\sin(\theta_1)\hat{b}_1 + \sin(\omega t)\cos(\theta_1)\hat{b}_2 + \cos(\omega t)\hat{b}_3\right), \tag{B.35}$$

and the desired $\hat{h}_i$ can be calculated

$$\hat{h}_i = \mathbf{R}\frac{{}^b\vec{H}(t)}{|{}^b\vec{H}(t)|}. \tag{B.36}$$

In a similar manner, a scatter signal coordinate frame, f, can be defined such that the z axis is in the direction of the scatter unit vector $\hat{s}$:

$$\begin{aligned}\hat{f}_1 &= -\sin(\theta_2)\hat{b}_1 + \cos(\theta_2)\hat{b}_2 \\ \hat{f}_2 &= \hat{b}_3 \\ \hat{f}_3 &= \cos(\theta_2)\hat{b}_1 + \sin(\theta_2)\hat{b}_2.\end{aligned}$$

Here θ_2, as previously defined, is the angle between ${}^b\vec{s}_{LOS}$ and the ellipse's semi-major axis. In this frame, the LHCP electric field follows simply from Equation (B.33),

$${}^f\vec{E}_s(t) = |\vec{E}|\left(\cos(\omega t)\hat{f}_1 - \sin(\omega t)\hat{f}_2\right),$$

and in the ellipse frame

$${}^b\vec{E}_s(t) = |\vec{E}|\left(-\cos(\omega t)\sin(\theta_2)\hat{b}_1 + \cos(\omega t)\cos(\theta_2)\hat{b}_2 - \sin(\omega t)\hat{b}_3\right). \tag{B.37}$$

The desired $\hat{e}_r$ can be calculated

$$\hat{e}_r = \mathbf{R}\frac{{}^b\vec{E}_s(t)}{|{}^b\vec{E}_s(t)|}. \tag{B.38}$$

Cylinder Approximation Results

The time-varying terms described above, $\hat{n}_0$, $\hat{i}$, $\hat{s}$, $\hat{e}_r$ and $\hat{h}_i$, all follow from the transmitter and receiver LOS vectors in the HST body frame and the HST-shuttle and HST-GPS satellite ranges from the STK simulation of HSM4. These input data are generated at one second intervals from 16:12:09 to 16:54:14 UTC on the day of rendezvous and docking, May 13, 2009. At each second, a specular point search is performed to supply the time-varying terms for the bistatic RCS calculation via Equation (B.12). The RCS computed for PRN 9 geometry, in decibel square meters versus GPS time since the start of the day, is shown in Figure B.5.

The RCS calculated from the STK simulation and cylinder approximation follows an increasing trend from 16:12:09 up to a peak at 16:46:54. This peak occurs at the near-singularity caused by the minimum of the numerator $1/(2kl\hat{z}\cdot(\hat{i}-\hat{s}))$. The

overall increase is reasonable, as HST is rotating into a position where it is viewed end-on from the shuttle payload bay. The flat surface of the space telescope's aft bulkhead should have a strong specular reflection. The STK simulation must be studied closer, however, to determine whether the sharp roll-off has a reasonable physical explanation. Note that the visibility of the specular point from the payload bay is not considered here - masking due to the bay doors and floor must be applied when calculating the expected received power.

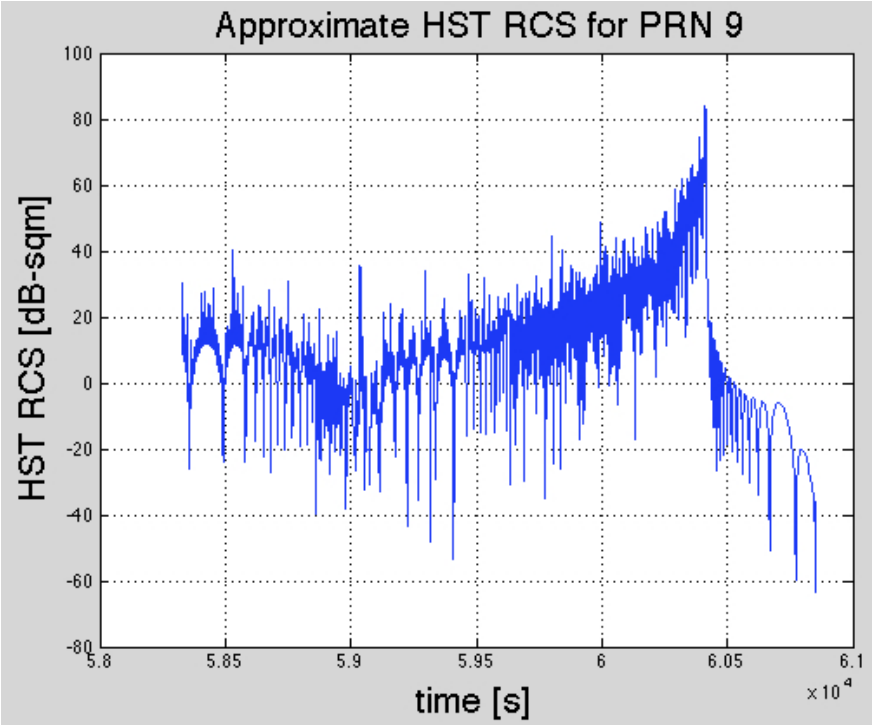

Fig. B.5. Bistatic radar cross section of HST approximated as a cylinder for PRN 9 geometry

B.2 Relative Signal to Noise Ratio

The ratio of direct signal power to reflected signal power is a measure of how much stronger the direct signal is than the reflected signal. This is essentially the power loss of the reflected signal relative to the direct signal, and is referred to here as the LHCP's

relative signal-to-noise ratio (SNR). Relative SNR eliminates receiver parameters that are common to both the direct and reflected signal power calculations:

$$\frac{P_{R,\text{direct}}}{P_{R,\text{reflected}}} = \frac{4\pi R_T^2 R_R^2}{R_D^2 \sigma}. \tag{B.39}$$

The relative SNR predicted with the STK simulation and RCS models for HST provides an indication of the feasibility of tracking Hubble-reflected signals for relative navigation. The power loss experienced by a reflected signal must be small enough that when it is subtracted from a strong direct signal power (e.g. 50 dB-Hz) the received signal power still exceeds a receiver's tracking threshold. If the receiver threshold is taken to be 25 dB-Hz, as suggested in [9], the relative SNR should be approximately 25 dB-Hz, though some post-processing techniques can be used to track weaker signals [4]. Relative SNR is also used to distinguish Hubble-reflected signals from those reflected by the environment near the receiver [62].

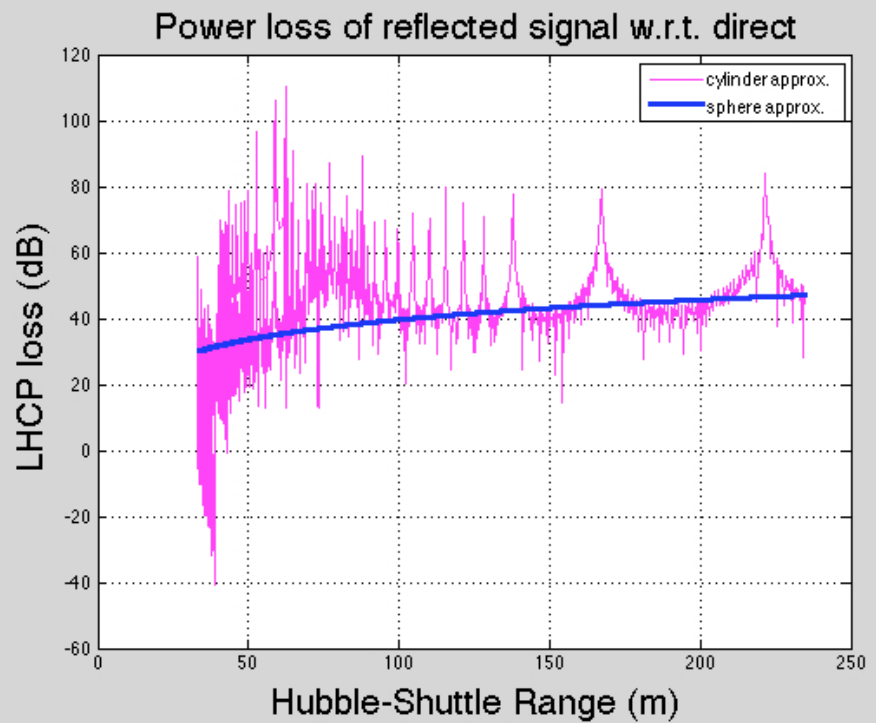

Fig. B.6. Relative SNR versus HST-shuttle range for sphere and cylinder RCS models

Figure B.6 shows the relative SNR for the cylinder and sphere RCS models as a function of HST-shuttle range. This is computed using the PRN 9 geometry. Interestingly, the two models result in similar trends over the changing HST-shuttle range. The deviation of the cylinder approximation from the smooth sphere approximation is the result of including the effects of HST attitude. This is presumed to be more accurate (not an erroneous deviation from a theoretical curve, as it may appear at first glance).

VITA

VITA

Ben Ashman was born on 28 October 1987 in Dayton, Ohio, to Lewis and Diane Ashman, a philosopher-turned-poet and writer-turned-computer programmer, respectively. He grew up in Kettering, a suburb of the "Gem City," and graduated high school in 2006. He started a bachelors degree that fall at Ohio University, a historic university in the Appalachian foothills of southeast Ohio. An advanced high school physics course and a passion for Hammond organs led him to major in Electrical Engineering. During his four years in Athens, he was active in the local music scene and worked two internships for electrical contractor M.C. Dean, first at the Pentagon in Arlington, Virginia, then at United States military bases Stuttgart, Germany.

In 2009 he spent a summer in Orono, Maine, studying sensors and laser ranging under a National Science Foundation Research Experience for Undergraduates (NSF REU) fellowship. This experience left him with an interest in research, and after graduating from Ohio University in 2010 he began a Ph.D. at Purdue University in West Lafayette, Indiana. He spent his scarce free time at Purdue visiting with his Uncle Doug and Grandpa Ashman in town, usually over pizza, and made bi-monthly trips to see Leah Bevis in Ithaca, New York. In 2011 he began working with Dr. Garrison, and that year was awarded a NASA Space Technology Research Fellowship (NSTRF). He spent the following five summers living in Washington, District of Columbia, and working at Goddard Space Flight Center in Greenbelt, Maryland. He began work as a civil servant at Goddard in the summer of 2015, and will continue work there in satellite navigation after graduating from Purdue in 2016. He remains close to his brother Sam, a saxophonist-turned-technical writer, who lives in Portland, Oregon.

Purdue University